A Model study of the Wind-Driven and Intrinsic Variability of the Atlantic Ocean

Giovanni Quattrocchi
November, 2010

Ph.D. Thesis

Universitá degli Studi di Napoli "Federico II"

Scuola di Dottorato "Scienze della Terra"
"Giuseppe De Lorenzo"

Dottorato di ricerca in Scienze ed Ingegneria del Mare, XXIII Ciclo

jointly with:
Universitá degli Studi di Napoli "Parthenope"
Seconda Universitá di Napoli
in collaboration with:
Istituto per l'Ambiente Marino Costiero - C.N.R.
Stazione Zoologica "Anton Dohrn"

Tutor: Prof. Stefano Pierini
Co-tutor: Prof. Henk A. Dijkstra
Ph.D. Candidate: Giovanni Quattrocchi

Ph.D. School Director: Prof. Alberto Incoronato

A mi familia amorosa.

Contents

Preface

Model studies of the large-scale oceanic variability are presented in this thesis. The North Atlantic Ocean is the basin under investigation and the tropical and mid-latitude regions are considered separately. The adopted model is based on the nonlinear primitive equations in the shallow water, reduced-gravity approximation in the presence of schematic coastlines that mimic with some degree of realism the real continental boundaries. This model approach, that may be termed process-oriented with essential elements of realism, was recently used by Pierini (2006, 2008); Pierini and Dijkstra (2009); Pierini et al. (2009) to study the Kuroshio Extension decadal variability, and has the advantage of allowing for the identification of basic dynamical mechanisms and, to some extent, also for direct comparison with observational data. More in general, this approach belongs to the class of idealized ocean model studies that in the last 15-20 years have contributed significantly to our understanding of the wind-driven low-frequency oceanic variability (e.g., Dijkstra and Ghill 2005; Dijkstra 2005)

The studies of the low- and mid-latitude North Atlantic Ocean are aimed at analyzing the directly wind-driven and intrinsically generated variability, respectively. More precisely, in the tropical region, the model will be forced by a time-dependent wind field obtained by ECMWF Reanalysis data, that will induce a variable oceanic signal due to both the local response to Ekman pumping and the non-local response associated with the activation of teleconnection mechanisms. On the other hand, in the mid-latitude model the forcing will be provided by a time-independent climatological wind stress field, so that one can be sure that all the low-frequency variability produced by the model is to be accounted for nonlinear mechanisms internal to the ocean system. The thesis is organized as follows.

Summary and Contents

Chapter 1 is a brief introduction to the wind-driven (section 1.1) and intrinsically induced (section 1.2) dynamics of the Atlantic Ocean. It also includes the motivations on which the numerical experiments are based (see Chapter 4 and Chapter 5).

Chapter 2 provides an overview on the wind regime and the oceanographic phenomenology of the Atlantic Ocean. The main features of the basin-scale wind stress variability, the typical circulation patterns and long wave propagation are then introduced.

Chapter 3 focuses on the shallow-water equations and their derivation. The process-oriented model approach and the adopted shallow water reduced-gravity model are also discussed.

Chapter 4 is devoted to the analysis of the wind-driven seasonal variability in the tropical Atlantic basin. Theoretical aspects of the ocean dynamics are discussed on the basis of both their experimental evidence and numerical simulations.

In Chapter 5 an analysis of the intrinsic low-frequency variability in the Gulf Stream region is presented. The model response is compared with satellite observations and the similarities are analyzed in detail. In the same chapter a preliminary analysis in terms of nonlinear dynamical systems theory is also proposed in order to gain a deeper insight into the internal variability produced by the model.

Finally, Appendix A, B and C provides the theoretical background for Rossby and Kelvin waves, the EOF analysis of the wind data and an introduction to the basic aspects of dynamical systems theory, respectively.

Acknowledgements

Prof. Stefano Pierini (DiSAm, University of Naples "Parthenope") is thanked for his essential professional support of my research activity. He is an indispensable guide through whom I improved my personal skills and competences. Thanks Stefano!

I really appreciated the accurate support and advices of Prof. Henk

A. Dijkstra (IMAU, Utrecht University); his friendly collaboration and all the opportunities that he gave me. Thanks Henk!

Giovanni Zambardino (DiSAm, University of Naples "Parthenope"), Marcel Portanger, Yvonne Wouda and Sandra Tap (IMAU, Utrecht University) are thanked for their essential technical support.

I would like to thank all my colleagues, in Naples and Utrecht, for their inputs, criticisms, advises and comments. In particular I thank the following friends for providing day by day contributions and encouragement: Giovanni Sgubin, Pasquale Castagno, Carlos Querino, Giovanni Liguori, Paola De Ruggiero, Christiana Photiadou, Giuseppe Aulicino, Werner Kramer, Dorota Mrozek, Theofanis, Ivan Vigano', Elena Jurado, Adriaan Zuiderweg, Catalina Gomez Alvarez, Nicola Bertelli, Chenjuan Jiang, Supun Pathirana, Sourish Basu, Giusy Martorano, Giuseppe Agrillo, Daniele Mastrangelo, Ivan Caso, Michele Cipriano, Adel Saidi.

Desidero ringraziare la mia famiglia per il suo infaticabile supporto logistico e morale durante tutto il periodo della mia formazione professionale: Anna e Nino, Laura ed Alessio con il loro nascituro Francesco. Vi prego, continuate a regalarmi momenti di gioia e serenita' che mi permettono di superare lunghe distanze.

Grazie a te Noemi, perche' con amore e risolutezza sai guidarmi verso le imminenti e nuove prospettive della mia vita sociale e professionale.

Naples, November 2010 *Giovanni Quattrocchi*

1

Scientific motivations

1.1 The wind-driven dynamics in the tropical Atlantic Ocean

The tropical Atlantic Ocean is the oceanic portion of the Atlantic basin that is located within an equatorial band between the Tropic of Cancer (23.5 °North) and the Tropic of Capricorn (23.5 °South). Much of the critical solar radiation falls on the tropics, where the Sun lies almost directly overhead for the entire year. Uneven heating of the globe between the tropics and the poles creates, hence, heat-driven atmospheric fluxes (winds) that, in turn, define the momentum transfer to the oceanic surface.

In the tropical Atlantic region the South-East and North-East Trade Winds are the dominant cause of the oceanic variability. The latter is mainly shaped by mid-latitude (far enough from the equatorial band) baroclinic Rossby waves radiating from the eastern boundary and yielding a pronounced refraction towards the equator due to the dependence of phase speed with latitude (the so called beta-refraction). Satellite observations and model studies provide evidence of these propagating signals, and support the hypothesis of their remote origin (Philander, 1990; Pierini, 2003, 2005; Polito and Sato, 2007; Polo et al., 2008; White, 1977). Indeed coastal Kelvin waves, generated in the equatorial region by wind stress changes, may reach higher latitudes using the eastern oceanic boundary as waveguide, and, in turn, promote mid-latitude westward propagating Rossby waves. This dynamics is known to be controlled by a teleconnection mechanism identified by McCreary (1976) in the different context of El Niño phenomenon, which contributes to the global redis-

tribution of the oceanic heat content. Basin-scale climatological implications and the development of regional-scale phenomena, such as seasonal upwelling and downwelling at the eastern boundaries of the oceans, are also due to such mechanism.

Central questions and approach

The following issues arising in the context of the tropical Atlantic Ocean variability discussed above can be singled out:

- how are annual baroclinic Rossby waves radiating from the eastern boundary of the Atlantic Ocean affected by beta-refraction?
- what is the contribution to their generation from local (Ekman pumping) and remote (teleconnection mechanism) forcing?
- can seasonal upwelling (downwelling) be promoted by the teleconnection mechanism at the eastern boundary of the Atlantic Ocean?

These issues have been analyzed in the context of the Pacific Ocean by Pierini (2003) through a process-oriented model study in which westward propagating Rossby waves were found to be mainly due to a remote forcing mechanism; moreover, in a related spectral analysis (Pierini 2005), theoretical examination of the spatial structure and frequency dependence of such waves was carried out.

The present research work will follow the same approach to the similar framework of the Atlantic Ocean, but with a different, more realistic design of the numerical simulations.

A nonlinear shallow water reduced-gravity model has been implemented in a domain of integration spanning the latitudes from 35 °S to 35 °N with a schematic but relatively realistic western coastline and characterized by a correct zonal extension at all latitudes. A perpetual wind forcing was constructed from ECMWF ERA-40 Re-Analysis Project data relative to the one-year period 2001 with a 6 hr temporal resolution and a 1°spatial resolution. The inclusion in the model implementation of essential elements of realism, such as a relatively realistic coastline and wind forcing, provides an efficient tool of investigation that is in between the extremely idealized approach typical of box models and the extremely sophisticated ocean general circulation model approach. Indeed, such

model allows for comparison of the obtained results with both observations (e.g., provided by satellite measurements) and three-dimensional ocean circulation model outputs.

1.2 Mechanisms of intrinsic variability in the Gulf Stream region

The classical steady theories of the wind-driven ocean circulation due to Sverdrup (1947), Stommel (1948), Munk (1950), etc, were all based on the analytical solution of the linearized governing equations. Although the linearization was clearly not fully appropriate (especially in relation with the western boundary current dynamics) they could nonetheless provide profound insight into underlined dynamical mechanisms. On the other hand, as far as the low-frequency variability of the wind-driven ocean circulation is concerned, the numerical solution of idealized nonlinear models (see Dijkstra 2005 for a comprehensive review) have more recently provided convincing evidence that nonlinear mechanisms all internal to the ocean system are able to generate vigorous modes of variability of western boundary current extensions from the interannual to the interdecadal time scales. These results have substantially modified our current view of the ocean dynamics, since previously it was usually assumed that ocean changes had to be in some way related to substantially modified variability.

Moreover, the systematic application of the methods of nonlinear dynamical systems and chaos theories (see again Dijkstra 2005) has revolutionized the way the obtained numerical results are interpreted. On the one hand we have the principles of geophysical fluid dynamics that all oceanic motions must satisfy; on the other hand the view of the ocean as a dynamical system allows one to represent in a simple geometric fashion very complex phenomena that could not be characterized otherwise. In general, when a natural system leaves its linear behavior it may experience successive instabilities that arise at different values of some control parameter. Any instability introduces extra degrees of freedom in the system, which, in turn, can alter the behavior of the system itself by generating intrinsic variability.

In the North Atlantic and Pacific Oceans the Gulf Stream and Kuroshio Extensions are outstanding examples of such a behavior. Indeed, they are found to be characterized by a strong low-frequency variability that may partly be due to intrinsic mechanisms. In particular, the Kuroshio

Extension (see Qiu 2002; Qiu and Chen 2005) yields a marked decadal variability of bimodal character involving two different states, an "elongated", fairly stable meandering jet and a much weaker "contracted", very variable and convoluted jet. By contrast, the Gulf Stream system shows a weaker bimodal character (Auer, 1987; Bane and Dewar, 1988) on the interannual time scale involving both the Gulf Stream deflection off South Carolina and the free Gulf Stream Extension (e.g., Kelly et al. 2010).

In this framework, some relevant observed features of the Gulf Stream and Kuroshio systems have been interpreted in terms of intrinsic ocean dynamics by several authors (e.g., Dijkstra and Ghill 2005; Dijkstra and Molemaker 1999; Schmeits and Dijkstra 2001; Simonnet et al. 2003; Spall 1996a and Pierini 2006; Pierini and Dijkstra 2009; Pierini et al. 2009).

Central questions and approach

In Chapter 5 it will be shown that our process-oriented ocean model forced by steady winds is able to generate a Gulf Stream-like jet and an intrinsic low-frequency variability. Thus, the following questions arise:

- is there any correspondence between the simulated mean Gulf Stream and its variability with the corresponding observed features?
- are the observed changes generated by intrinsic mechanisms or, rather, by wind stress anomalies?

The process-oriented model study adopted for this analysis (see Chapter 5) is the same nonlinear shallow water reduced-gravity model used in the low-latitude application, here implemented in a schematic domain of the North Atlantic basin. The model is forced by a time-independent climatological wind stress derived by ECMWF Re-analysis data. The inclusion of such realistic wind stress and schematic coastline allow us to carry out a validation of the model response with satellite observations. As a result, this model implementation has allowed us to obtain a Gulf Stream-like jet whose variability is certainly due intrinsic oceanic mechanisms.

This approach follows Pierini (2006), Pierini and Dijkstra (2009) and Pierini et al. (2009), which successfully applied the same model in the North Pacific Ocean. Those model results showed a decadal chaotic os-

cillation of the Kuroshio Extension system due to intrinsic oceanic dynamics. It should be pointed out that, because of the reduced-gravity approximation, topographic effects and the interaction of the Gulf Stream with the Atlantic Deep Western Boundary Current are not considered in the present model. Those effects will, however, be analyzed in a study, already under way, based on a model with two active layers.

2

The Atlantic basin: climate and ocean

2.1 Basin-scale wind regime

The global distribution of high and low pressure zones defines the origin, the intensity and the variability of the prevailing winds in the Atlantic basin. Looking at figures 2.1 and 2.2, the most outstanding feature appears to be the large seasonal variation of the Northern Hemisphere winds in comparison to the small variation in the Southern Hemisphere. During the northern winter, the subtropical high pressure belt covers the Florida and Bermuda regions, the Canary Islands and the Azores and it runs to the east over the Sahara desert, the Mediterranean sea and Siberia. During the northern summer it reduces to a cell of high pressure centered near the Azores, known as the Azores High. In the Southern Hemisphere the position of the subtropical high is mostly stable. The Intertropical Convergence Zone (ITCZ) can be defined as an equatorial belt of low atmospheric pressure which runs between the subtropical highs. To be more precise, in the Atlantic Ocean, the mean position of the ITCZ moves Westerlies from the equator off Brazil to about $7°N$ off the Ivory Coast. Weak winds, called Doldrums, blow in this region. The prevailing winds, blowing from the subtropical highs to the equatorial low, are known as North-East and South-East Trades. They are usually stronger in winter (in February north of the equator and August in the south) than in summer on both hemispheres. The subpolar low pressure belt includes, in the northern part of the Atlantic basin, the Icelandic Low with its strong Westerlies, which follow the isobars between the subtropical

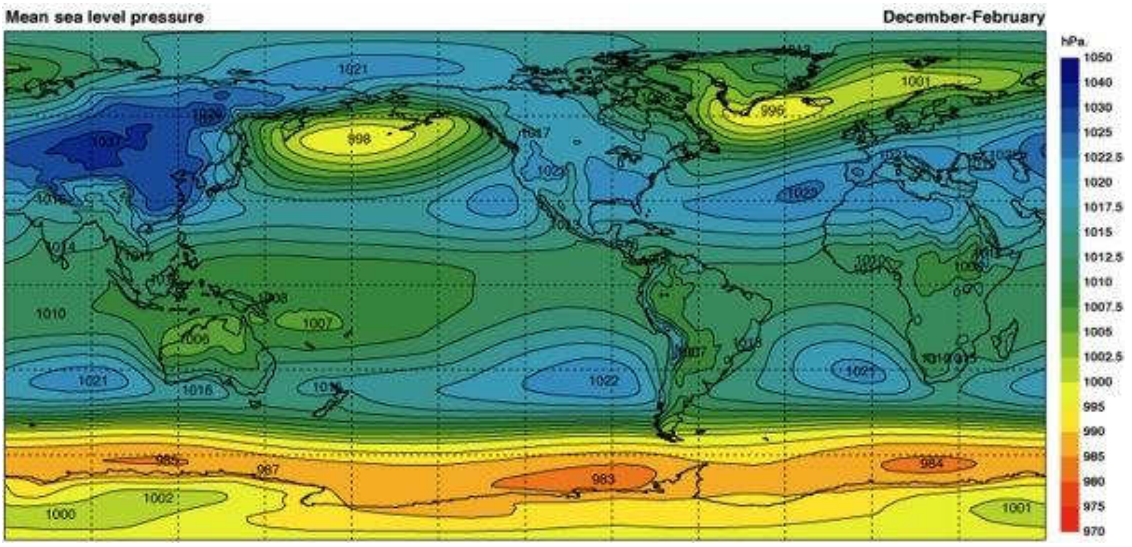

Figure 2.1: Mean Sea level pressure (December - February) derived from ECMWF Surface Climatology, ERA-40 Atlas.

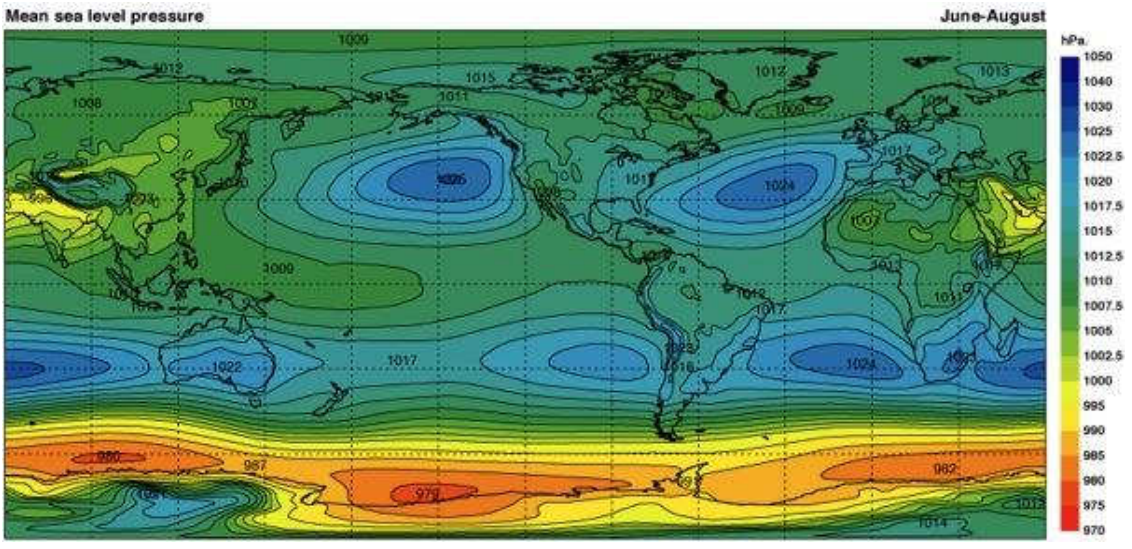

Figure 2.2: Mean Sea level pressure (June - August) derived from ECMWF Surface Climatology, ERA-40 Atlas.

---

high pressure belt and the low pressure to the north. The North Atlantic Westerlies enter the ocean from the northwest bringing cold dry air out over the Gulf Stream and its maximum strenght is oriented along a line running east-north-east (Tomczak and Godfrey, 2001). In the Southern Hemisphere the position and intensity of the subpolar low is mostly stable and the Westerlies show correspondingly less variation there. Seasonal wind reversal occurs in a very limited area along the northern boundary of the Guinea Gulf causing the seasonal upwelling events.

2.1.1 Low-latitudes wind-stress regime and its variability

In this section, a thorough analysis is devoted to the understanding of the atmospheric seasonal variability of the subtropical regions. A single year (2001) of ECMWF wind stress data was analyzed and compared with similar analysis (e.g. Risien and Chelton 2008). In the region, spanning the latitudes between 35°N and 35°S and the longitudes between 80°W and 20°E, interesting temporal and spatial scale features of the wind arise through the analysis carried out in this research work. The wind stress data, have been retrieved from "ERA40" re-analysis on a 1°× 1°grid based upon four mean data per day wind analysis.

Monthly means for both zonal (positive from the west) and meridional (positive from the south) wind stress components have been computed. Zonal wind stress fields on February (Fig. 2.3) and August (Fig. 2.4) show some notable features of the seasonal atmospheric variability. There are two dominant almost symmetric structures centered at 15°N and 15°S respectively, which represent a general shape of the Trades in the Atlantic basin. These structures yield a seasonal increase in their intensity especially during the northern summer. More precisely, the wind is strongest from June to September and it starts to relax towards the end of the calendar year (Philander, 1990). In figures 2.3 and 2.4, the lowest wind intensity belt identifies the ITCZ. During the year, the location of the ITCZ is predominantly in the Northern Hemisphere where it migrates seasonally between the neighborhoods of the equator, during the first months of the year until April, and the latitude of 12°N approximately in August and September (Philander, 1990). In this last stage, the South-East Trades, with their increasing intensity (longitude-time diagram in figure 2.5), can easily reach the equatorial area and generate seasonal equatorial waves (see Colling and CourseTeam, 2002).

Two different belts are located between 30°and 35°of latitude, both in the northern and Southern Hemisphere (Fig. 2.3 and Fig. 2.4). They

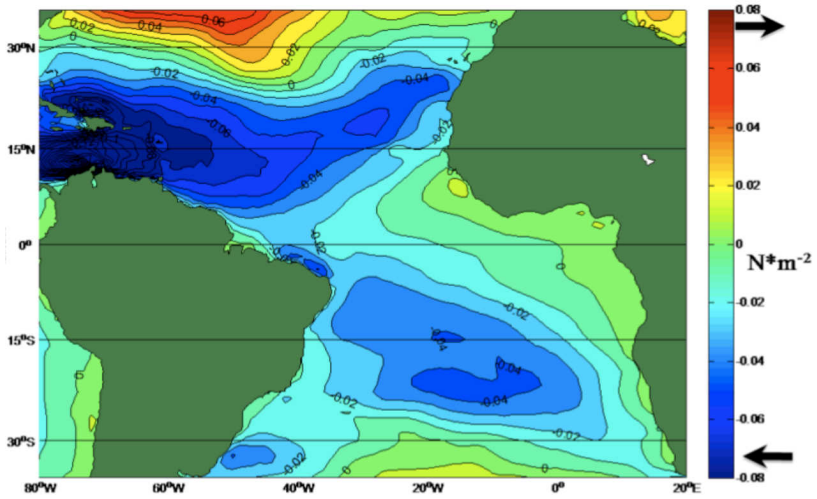

Figure 2.3: Monthly mean (February) of the zonal component of the wind stress in the tropical Atlantic Ocean ($N \cdot m^{-2}$). Red indicates eastward wind component while blue indicates westward wind component

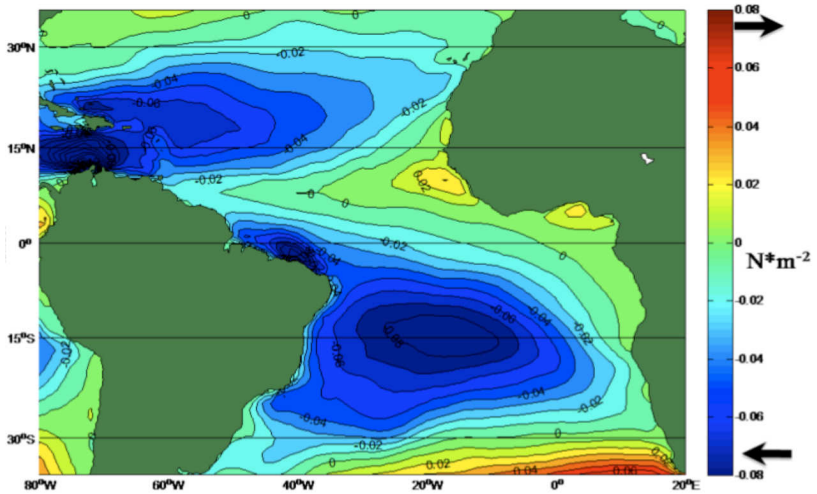

Figure 2.4: Monthly mean (August) of the zonal component of the wind stress in the tropical Atlantic Ocean ($N \cdot m^{-2}$). Red indicates eastward wind component while blue indicates westward wind component

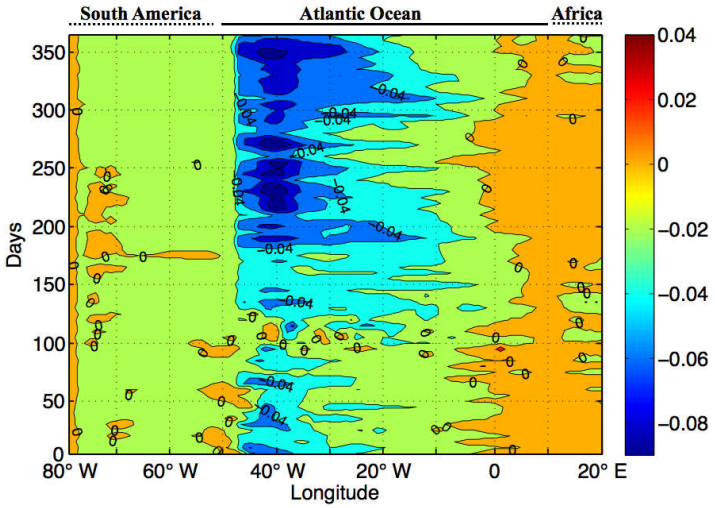

Figure 2.5: Hovmüller diagram representing an equatorial section of the zonal component of the wind stress during the year 2001 ($N \cdot m^{-2}$). Red indicates eastward wind component while blue indicates westward wind component

are the first part of the larger subtropical atmospheric circulations. As expected, the north anticyclone leaves the tropical area during the boreal summer (Fig. 2.4), while its counterpart in the south persists into the belt, with increasing intensity; such feature may plays an important role in shaping the south tropical oceanic variability. Another interesting feature, between the tropics, is the almost continuous absence of easterly forcing along the african coasts, except from June to September (figures not shown) when local faint winds can induce summer upwelling in the Guinea Gulf, close to Nigeria, Ghana, Ivory Coast and Guinea coasts.

Monthly averages of the meridional wind stress fields (see Fig. 2.6 as example) show, near the African coasts, structures centered on the tropics in both hemispheres almost during all the year. In these regions, the intensity of the meridional component of the wind stress is prominent if compared with the zonal component. This persistence of the wind forcing, together with the typical meridional orientation of the coasts, supports the formation of upwelling; indeed,close to Cape Blanc and Cape Frio, along the northern and southern directions respectively, areas of coastal upwelling are found all year round. Along the Guinea Gulf boundaries,

between Cape Frio and Cape Lopez, the meridional wind stress component increases from June to September triggering a weak confined coastal seasonal upwelling.

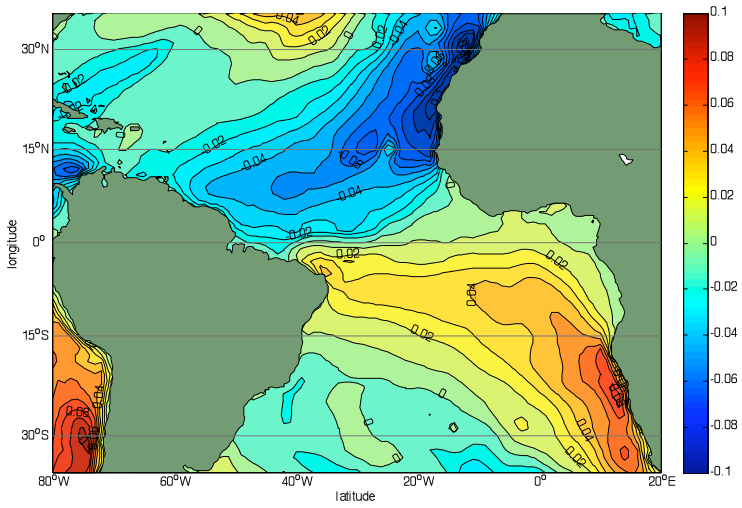

Figure 2.6: Monthly mean (April) of the meridional component of the wind stress in the tropical Atlantic Ocean ($N \cdot m^{-2}$). Red indicates northward wind component while blue indicates southward wind component

The wind-stress curl, due to its proportionality to the Ekman pumping, is another physical quantity of interest for the study of the oceanic variability. Risien and Chelton (2008) estimated global seasonal cycle of the wind stress and its derivative (curl and divergence) from the eight years record (1999-2007) of wind measurements by the NASA Quik scatterometer (QuikSCAT). Monthly means were computed by harmonic analysis that have some advantage if compared with the arithmetic mean (Risien and Chelton, 2008). The spatial resolution of the data was (0.25°x 0.25°) and the temporal resolution consisted of twice-daily observations. Although ECMWF data (here analyzed) have a coarser spatial resolution then QuikSCAT data, it is possible to compare the wind-stress curl fields and find similar structures in both large and small scale. In each hemisphere, between easterly winds and mid-latitude westerlies, two patterns are present (Fig. 2.8): negative (positive) curl in subtropical northern (southern) regions and positive (negative) curl close to the equator in Boreal (Austral) Hemisphere. Along the western continental margins of Africa there are some areas of cyclonic wind-stress curl. In the same

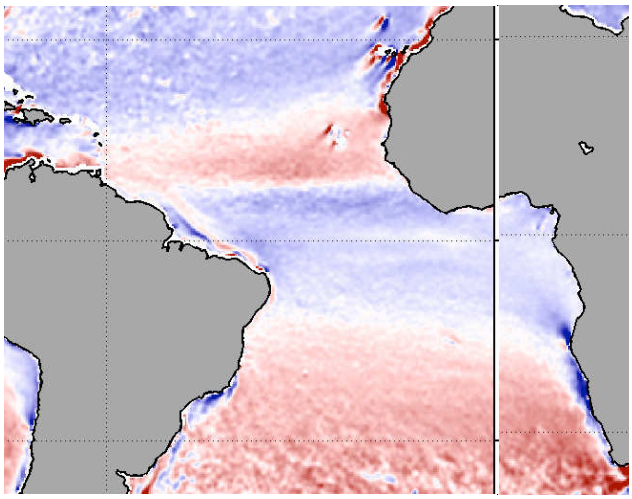

Figure 2.7: Monthly mean (August) of the vertical component of the wind-stress curl in the tropical Atlantic Ocean, obtained by the QuikSCAT data ($N \cdot m^{-3}$).

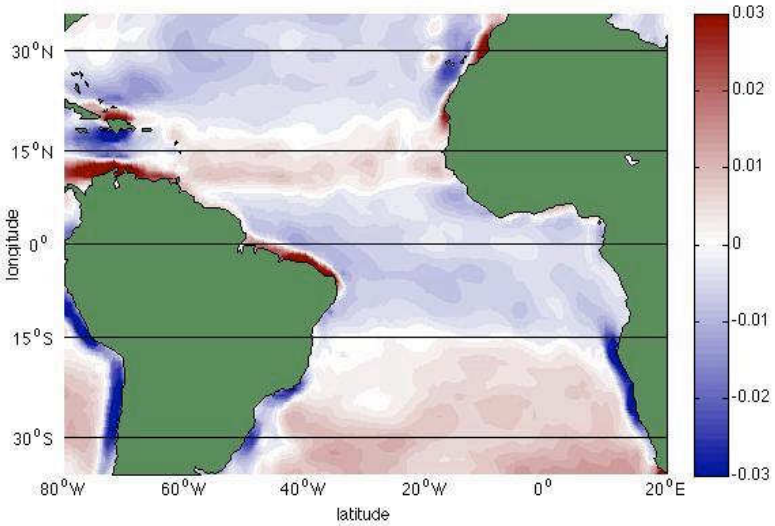

Figure 2.8: Monthly mean (August) of the vertical component of the wind-stress curl in the tropical Atlantic Ocean, obtained by the ECMWF data ($N \cdot m^{-3}$).

areas the wind-stress curl drives the upwelling phenomenon, in which cold and nutrient-rich waters raise to the sea surface with important dynamical and economical implications. Weak and limited wind-stress curl patterns are restricted to the Guinea Gulf boundaries, but it should be borne in mind that the seasonal upwelling, in this area, is not solely determined by the local wind forcing (Adamec and O'Brian, 1978; Moore et al., 1978; Polo et al., 2008).

A notable feature is the latitudinal bending of alternating negative and positive wind-stress curl which crosses the equator. This phenomenon has been well documented in the Pacific Ocean and it can be detected in the Atlantic Ocean as well. The bending is due to the influence of the sea surface temperature on surface winds (Risien and Chelton, 2008). Orographically induced features such as island corner acceleration and wind shadows can be detected in both, ECMWF and QuikSCAT data set (Xie et al., 2001). Figures 2.7 (adapted from Risien and Chelton, 2008) and 2.8 highlight such features.

2.1.2 Mid-latitudes wind-stress regime

Another wind stress data set, provided by ECMWF, has been retrieved from "ERA40" re-analysis on a 1°× 1°grid. Such data set covers a wide region of the Atlantic Ocean and spans the latitudes between 10°S and 60°N, and the longitudes between 85°W and 15°E. Monthly samples have been analyzed, for the period 1961-2001, with the aim of identifying general features of the momentum fluxes and their interannual variability. A climatological wind-stress forcing has been derived here in order to draw the contours of a mean direction and intensity of the wind field for the northern Atlantic basin. Such a climatology will also be used as a forcing for model experiments.

The zonally averaged picture (2.9) does not reveal the much greater interannual variability of the wind stress in the Atlantic basin. Indeed, these results make use of a mean annual cycle, formed by 12 mean monthly values of zonal (top panel of the figure 2.9) and meridional (bottom panel of the figure 2.9) wind stress. However, zonal (positive eastward) and meridional (positive northward) components yield their distinctive meridional location. In detail, two narrow belts of weak intensity winds are found at about 3°N off the Equator and along the latitude of 34°N. Their meridional position is mostly stable, hence, the variability is weak. A couple of wider belts include the North-East Trade winds (between about 10 °N and 34 °N) and the Westerlies (between about 34

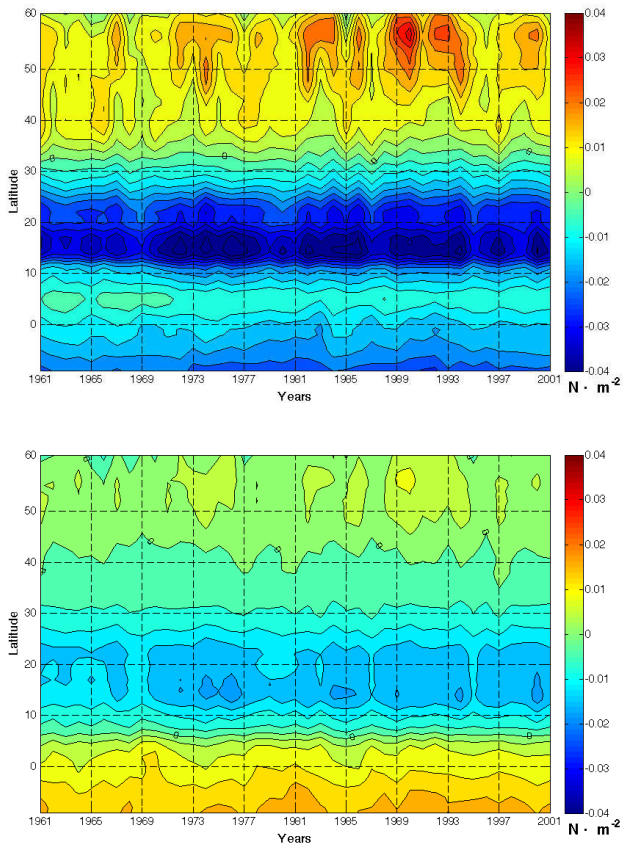

Figure 2.9: Latitude-time sections of the annual mean of the zonal τ_x [top panel] and meridional τ_y [bottom panel] wind stress ($N \cdot m^{-2}$).

°N and 60 °N). Their interannual variability yields three maxima, of the zonal and meridional wind stress intensity, localized in the middle of the figure for the period 1969-1995. Their periodicity is almost decadal and the signals have about the same phase.

Large-scale and meso-scale features of the mean wind field can be highlighted by the climatology for the northern atlantic basin (Fig. 2.10). Wind vectors (vector average direction) are superimposed over the mean wind-stress curl field. The main feature that emerges is the subtropical anticyclonic gyre, whose northern and southern edges are flanked by the cyclonic subpolar gyre and the South-East Trade Wind respectively. A close examination reveals the convergence of the arrows in the tropics

along the ITCZ, characterized by its weak wind belt. A strong upwelling favorable equatorward wind stress is found to the west of the african continent between about 10°N and 40°N. The extra-tropical region, to the north, yields two broad areas of relatively strong wind stress; one centered at about 36°N - 61°W and one centered at 48°- N 43°W in agreement with scatterometer data analyzed by Risien and Chelton (2008).

The wind-stress curl field yields a latitudinal large-scale bending of alternating negative and positive values across the equator (Fig. 2.10). Along the east coast of the United States (Fig. 2.11), between about 34°N, 36°N), parallel narrow bands of positive and negative wind-stress curl straddles the Gulf Stream. When viewed in the direction of the flow, the Gulf Stream is accompanied by wide parallel bands of negative and positive wind-stress curl to the right and left sides of the current, respectively. East of Newfoundland is a region of strong positive wind-stress curl. Finally, as argued by Josey et al. (2002), it should be noted that although the ECMWF fields appear reasonable at the basin scales (Fig. 2.10), they are known to exhibit high values for the stress at a number of island sites.

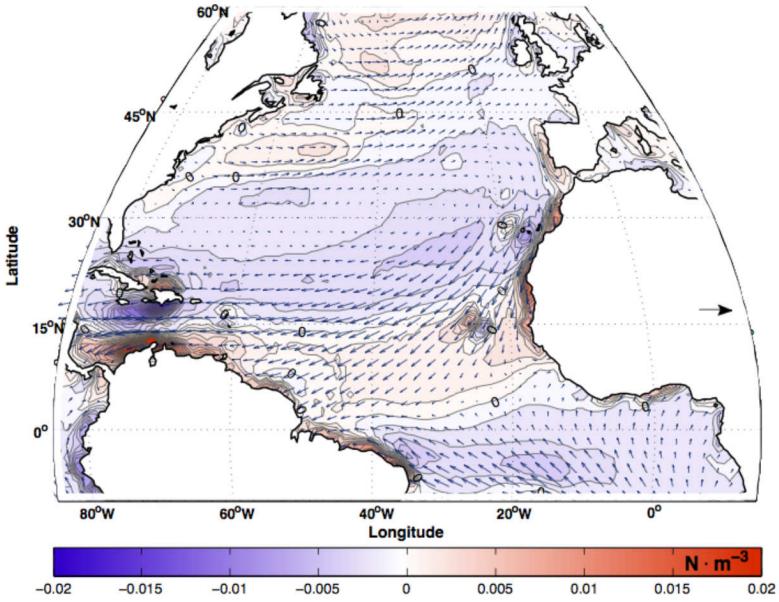

Figure 2.10: 41-yr average of the wind-stress curl ($N \cdot m^{-3}$) and the wind stress field (the arrow indicates the maximum speed [$13m/s$]) in the Atlantic Ocean, obtained from the ECMWF ERA40 re-analysis

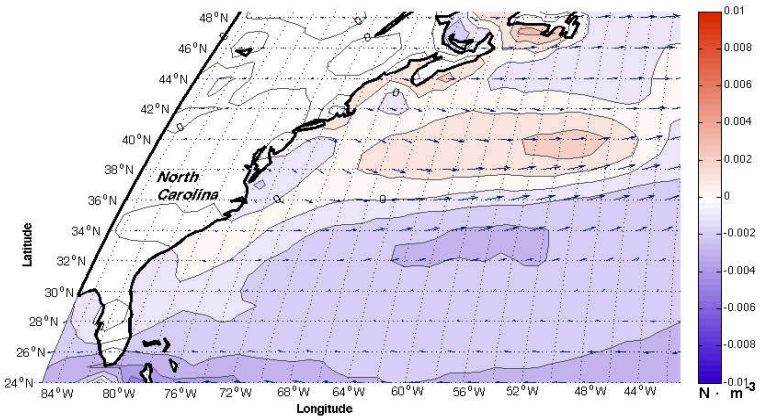

Figure 2.11: Magnification of the figure 2.10 to emphasize the Gulf Stream region climatological features

2.2 Surface circulation patterns

The large-scale ocean circulation is driven by momentum fluxes associated with the wind, heat content and fresh water at the air-sea interface. However, the surface current patterns are mainly shaped by winds and general common features can be found in the Atlantic, Pacific and Indian Oceans.

Figure (2.12) shows a qualitative scheme of the main currents in the Atlantic basin. In this figure, the Southern Ocean is characterized by the Antarctic Circumpolar Current (ACC) and the south Atlantic region by an anti-cyclonic gyre, which dominates the circulation. The stronger current on the western arm of the gyre is the Brazil Current, whose intensity is due to the western intensification (see section 5.2). Along the equator, a narrow band includes the equatorial currents which flow to the western side of the basin following the path of the Easterlies. More details of the equatorial current system will be given in section 2.2.1. The north Atlantic region shows a strong anti-cyclonic gyre, and a weaker subpolar cell. Also here, the western intensification generates the strong Gulf Stream with typical horizontal velocities of 1 $m \cdot s^{-1}$. The gyres, which are typically centered around 30°N and 30°S are called "subtropical gyres" and their boundaries nearly coincide with the zero

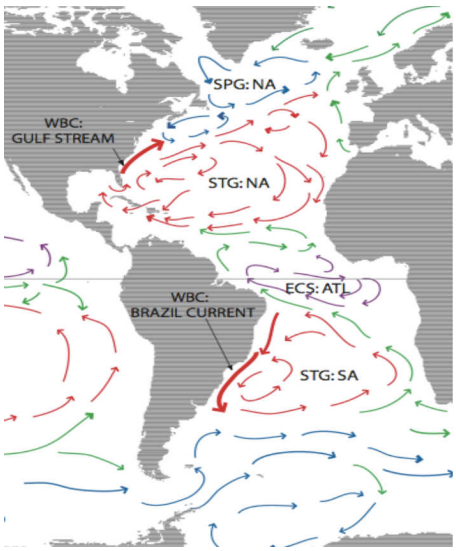

Figure 2.12: A qualitative scheme of the main currents of the Atlantic Ocean. Key: STG - Sub Tropical Gyre; SPG - Sub Polar Gyre; WBC - Western Boundary Current; ECS - Equatorial Current System; NA - NorthAtlantic; SA - SouthAtlantic; ATL - Atlantic; (Adapted from Vallis, 2006)

wind-stress curl contours. The northern subtropical gyre consists of the North Equatorial Current with its centre near 15°N, the Antilles Current, and the Caribbean Current. Once it reaches the western boundary, the Florida Current, the Gulf Stream, the Azores Current, and the Portugal and Canary Currents close the loop. The southern gyre mainly consists of the South Equatorial Current (SEC) which is centred in the Southern Hemisphere. The SEC follows the equatorial latitude until it reaches the Brazil coast, where it is known as the Brazil Current. The South Atlantic Current, and the Bengala Current close the loop in the Southern Hemisphere.

2.2.1 The equatorial current system

In a zonal belt between the tropics, a complex system of zonal currents with different features, dominates the equatorial circulation. Such a system is found, with similar behaviors in the Pacific and Indian oceans as well. The intensity of these zonal currents is very sensitive to the seasonal variability in the wind forcing. Starting from the Northern Hemisphere: the North Equatorial Current (NEC) flows westward, the North Equato-

rial Counter-Current (NECC) and the South Equatorial Counter-Current (SECC) follow the eastward direction and the South Equatorial Current (SEC) runs to the west (Fig. 2.13).

The NEC flows westward and spans the latitudes of 7 °N and 20 °N. This current forms the southern edge of the North Atlantic subtropical gyre and reaches the american continent, where it joins the Canary Current. Its horizontal velocities change with season; 10 $cm \cdot s^{-1}$ during the boreal summer and 15 $cm \cdot s^{-1}$ during the winter. The NECC runs to the east with similar intensity but it shows a strong seasonal variation which leads the current to disappear during the boreal winter (usually in December, January and February), when the North-East Trade Winds are very strong. The SEC flows westward and covers a large area from 4 °N to 15-20 °S depending on the season. It reaches the american continent, where it merges with the Bengal Current, and splits into the North Brazil Current (running to the north) and the Brazil Current (to the south). The horizontal velocities exhibit a seasonal variability from 10 to 30 $cm \cdot s^{-1}$. The SECC flows to the east and its formation region is located near 30 °W; it crosses the entire south Atlantic, at about 7 °S - 9°S, with a subsurface velocity core of 20 $cm \cdot s^{-1}$ and can experience seasonal reversal due to the seasonal increase of the intensity of the South-East Trade Winds.

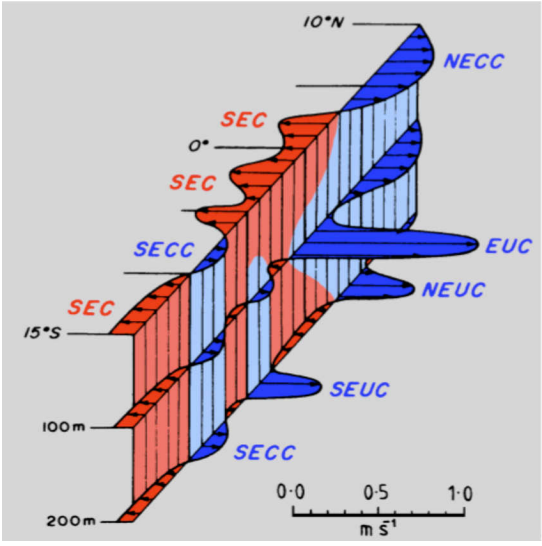

Figure 2.13: A scheme of the structure of the equatorial current system during August (Stramma et al., 1990). Acronyms: see section 2.2.1.

The generation mechanism of the equatorial current system is due to the Trade Winds at the air-sea interface. Such winds drive surface water to the west (westward currents) and water piles up against the western boundary of the Ocean. This causes a sea-surface slope up towards the west which, in turn, determines a zonal pressure gradient so that the counter-current can flow eastward along the Doldrums belt. A concomitant adjustment in the thermocline, which slopes down towards the west, is due to baroclinic compensation. Such a slope generates a subsurface eastward jet-like current known as the Equatorial Undercurrent (EUC).

2.2.2 Western boundary currents

Currents at the western side of the basins are the strongest in the world oceans. In the north Atlantic Ocean, the Gulf Stream transport is 88 Sv at 38 °N (Johns et al., 1995), and the Labrador Current transport of 7.6 Sv was calculated by Greenberg and Petrie (1988). In the south Atlantic the Brazil Current transport is 22 Sv at 28 °S (Mueller et al., 2000).

It is customary to divide the Gulf Stream into the following components: the Loop Current located in the Gulf of Mexico, the Florida Current, the Gulf Stream proper, the Gulf Stream Extension and the continuation of the jet, like the North Atlantic and Azores Currents (Tomczak and Godfrey, 2001). The Florida Current is fed from that part of the NEC that passes through the Yucatan Strait. In the Florida Strait this currentcarries about 30 Sv with speeds that can sometimes exceed 1.8 $m \cdot s^{-1}$. The Gulf Stream follows the shelf shape off Carolina and separates from the shelf itself near Cape Hatteras. The jet flows across the open Ocean as a free inertial jet and it increases the transport up to 90-150 Sv, near 65 °W, due to the Sargasso Sea recirculation (Fig. 2.14). The inertial jet, penetrates into the open ocean, becomes unstable and forms meanders, which eventually separate as eddies. Meanders which separate poleward of the jet develop into anticyclonic eddies, those separating equatorward produce cyclonic eddies. Most of the Gulf Stream eddies are formed in the Extension region and move back against the direction of the main current. The Labrador current is the western boundary current of the subpolar gyre. Since it receives considerable input of Arctic water from the East Greenland Current, its transport contains a large barotropic component. The seasonality shows that such a current is strongest in February when on average it carries 6 Sv more water than in August.

In the Southern Hemisphere the Brazil Current originates at 9 °S.

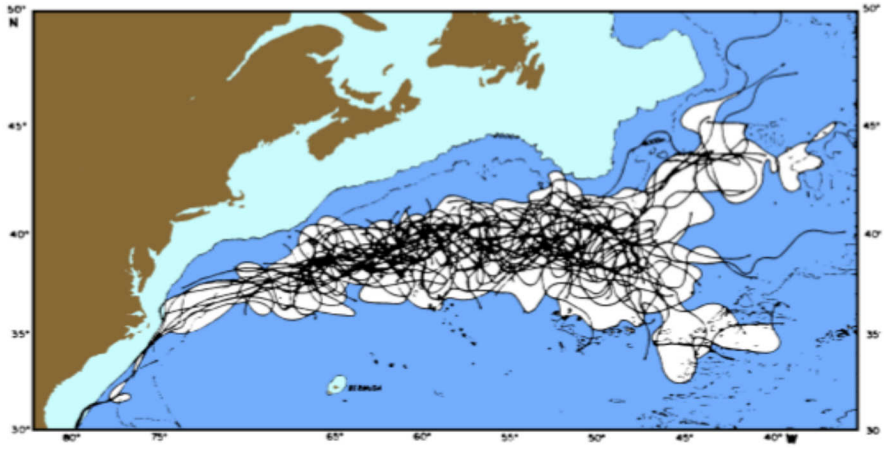

Figure 2.14: Path of satellite-tracked buoys in the Gulf Stream system from the period of 1977 to 1981. Only buoys with average velocity exceeding $0.5ms^{-1}$ were used and loops indicative of meanders were removed. From Tomczak and Godfrey, 2001

It carries warm subtropical water from about 9 °S to about 38 °S and it is generally confined to the upper 600 m of the water column. It originates where the westward flowing trans-Atlantic South Equatorial Current (SEC) bifurcates as it approaches the continental shelf off Cabo de Sao Roque in Brazil (Stramma et al., 1990). Geostrophic calculations of the transport (level of no motion near 1500 m) gave 5 Sv at 9 °S and, due to the recirculation cell south of the Rio Grande Rise, they lead to an increase in transport to 19 -22 Sv near 38 °S. The Brazil Current separates from the shelf between 33 °S and 38 °S, forming an intense front with the cold water of the Malvinas (Falkland) Current. The separation point is more northerly during the summer (December - February) than in winter, possibly as part of a general northward shift of the subtropical gyre in response to the more northern position of the atmospheric high pressure system and northward movement of the contour of zero curl (Tomczak and Godfrey, 2001). Before concluding this section it appears necessary to mention the Deep Water Circulation. The westward intensification influences the flow of Deep Water; indeed, both the southward transport of Deep Water at depth and the northward flow of the recirculation below and above the thermocline are concentrated on the western side of the Ocean. The deep water, which is a result of the thermohaline forcing, can influence the wind-driven flows and vice versa. For instance, Spall (1996b) showed that the Gulf Stream (GS)/Deep Western Bound-

ary Current (DWBC) crossover is a region of intense mixing that can alter the properties of both GS and DWBC on the basin scale.

2.3 Long waves in the ocean

The large-scale and meso-scale oceanic circulation, as well as the global climatology, are deeply affected by propagation of long-period waves, such as oceanic Kelvin and Rossby waves. They allow the energy to travel rapidly between the west and the east side of the oceanic basins and from the equator to higher latitudes and vice versa. For instance, at low, middle and high latitudes the energy is found to travel westward in the form of Rossby waves, while at low latitudes it also travels eastward within Kelvin waves propagating along the Equator. Synoptic observations are useful to detect propagation of such disturbances in the ocean. Indeed, data from recent altimetric missions, such as Topex/Poseidon, ERS 1-2, Envisat, Jason 1-2, have provided an essential tool for monitoring and investigating synoptically the oceanic variability. The dynamically active part of the sea surface height (SSH) anomaly is one of the components into which the measured anomaly can be decomposed. It can be determined by filtering the SSH anomaly related to the ocean tides, isostatic response of the ocean to external pressure fluctuations, "steric" anomaly due to heat exchanges with the atmosphere and the anomaly associated to instrumental errors (Pierini, 2002). Typical applications of altimeter measurements concern the interpretation of large-scale oceanographic processes with surface signature; the latter, in turn, can be directly used for validations of theoretical and modeling results as it was carried out in this research work.

It is known that, along the equatorial Atlantic latitude, changes in the slopes of the sea surface and thermocline occur rapidly (see Section 2.2.1). The minimum and maximum slope of the thermocline (Fig. 2.15) roughly correspond to the periods of minimum (during March-April) and maximum (during August-September) of the South-East wind stress (Katz and collaborators, 1977). Nevertheless, the rapid response of the ocean cannot be explained in term of water being transported across the equatorial Atlantic but in term of waves traveling through the ocean. Waves transmit the effects of the changes in the overlying wind field from one oceanic region to another.

Such waves can be barotropic and baroclinic waves and the vertical displacement may be greatest where there is a strong vertical density gra-

dient as in the tropical and subtropical regions; while barotropic waves involve the entire depth of the fluid with a non-zero integrated net transport, baroclinic (internal) waves appear, within a stratified ocean, in a layer with large density gradient which acts as an interface. The net integrated transport for baroclinic waves is equal to zero. Example of such density gradient in the ocean is the thermocline, which separates the oceanic mixed layer and the much deeper layer of cold water below.

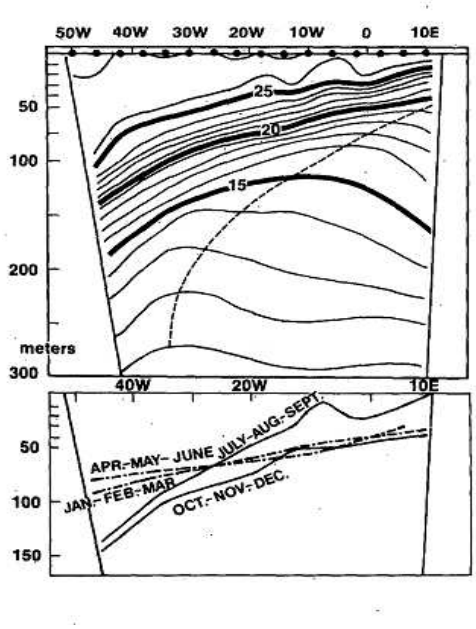

Figure 2.15: Top: isotherms (°C) along the equatorial latitude. Bottom: 23 °C isotherm along the equatorial latitude in different seasons. The slope is small when the Trade winds are weak (first part of the year), and it is large when the winds are intense (second half of the year (Philander, 1990).

Since these waves have very long wavelengths and periods, they feel the effect of the Earth's rotation. As a result, motion occurs in both horizontal and vertical direction as may be seen in the flow pattern associated with Kelvin waves and planetary (Rossby) waves. The generation mechanisms of Kelvin and Rossby waves, their features and their role in the oceanic variability is presented in this section. One may refer to Appendix A, Pedlosky (2003) and Vallis (2006) for a complete derivation and a comprehensive theoretical treatment of the subject.

Kelvin waves are a special type of gravity waves that are affected by the Earth's rotation. It is possible to distinguish Kelvin waves in

two basic types: coastal trapped (or coastal) Kelvin waves and equatorial trapped (or equatorial) Kelvin waves. A Kelvin wave can either be barotropic or baroclinic. The passage of a coastal or equatorial baroclinic Kelvin waves have the effect of bringing cooler, sub-thermocline water to the surface, promoting periodic upwelling events of strong intensity. Kelvin waves move equatorward along an oceanic western bound-

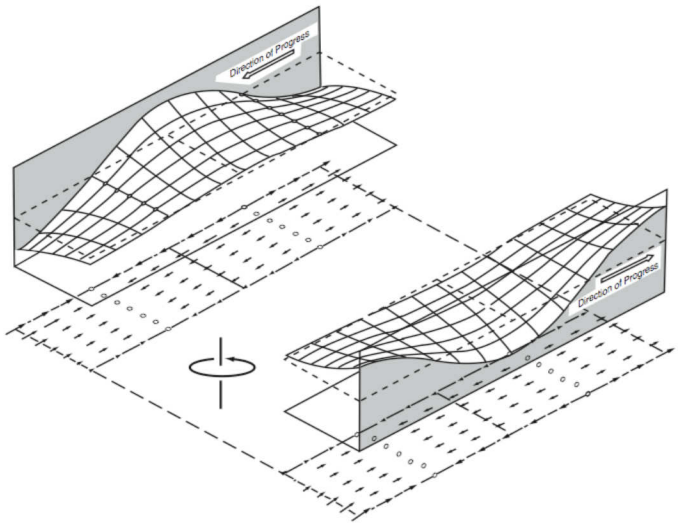

Figure 2.16: Northern Hemisphere Kelvin waves on opposite sides of a channel. In each vertical plane parallel to the coast, the currents (shown by arrows) are within the plane. The surface elevation varies exponentially with distance from the coast in order to satisfy the geostrophic balance. Kelvin waves move with the coast to the right in the Northern Hemisphere and on to the left in the Southern Hemisphere. (From Gill, 1982)

ary, poleward along an eastern boundary and cyclonically around a closed boundary, counter-clockwise in the Northern Hemisphere and clockwise in the Southern Hemisphere (Fig. 2.16). The wave amplitude is largest at the boundary and decays exponentially from it. The wave amplitude is significant only within an e-folding distance, of the order of the Rossby radius of deformation, from the lateral boundary or from the equator for equatorial Kelvin wave. For deep water and at mid-latitude in the ocean, the external Rossby radius is given by $R_e = \sqrt{gH}/f$ and its magnitude is of the order of O (1000 km) while the internal Rossby radius is given by $R_i = \sqrt{g'H}/f$ and its magnitude is of the order of O (100 Km). In the vicinity of the equator one should consider the equatorial Rossby radius,

whose magnitude is of the order of O (2000 km) for barotropic waves and of the order of O (200 km) for baroclinic waves (Gill, 1982). In the expressions above g is the Earth gravity; $g' = g\Delta\rho/\rho$ is the reduced gravity; f is the Coriolis parameter and H is the depth of the fluid. At the Equator, Kelvin waves always propagate eastward and the maximum magnitude decays exponentially from it with increasing latitude. Thus, the existence of the Kelvin wave relies on the Earth gravity, a stable stratification, the Coriolis acceleration and a waveguide, such as a boundary or the equator.

Rossby waves dominate the large-scale sub-inertial variability of the atmosphere and the oceans. The restoring force, which leads to the generation and propagation of such waves, is the variation of the Coriolis parameter with latitude, called β-effect. Rossby waves can also be generated by a variation in depth of the sea-floor, through an equivalent topographic β-effect. The generation and propagation of the Rossby waves, can be explained in term of conservation of potential vorticity (Fig. 2.17). Consider a stationary fluid parcel along a line of constant latitude of a barotropic ocean, and suppose that some disturbance causes displacement to another latitude. In the displacement, the potential vorticity of the fluid is conserved, and in the simplest case of barotropic flow the potential vorticity on the β-plane is $\beta y + \zeta$ where ζ is the relative vorticity of the fluid. Thus, in either hemispheres, a northward displacement leads to the production of positive relative vorticity (clockwise rotation of the fluid parcel), indeed, the parcels move to regions of higher positive planetary vorticity f. The relative vorticity gives rise to a velocity field which, in turn, advects the parcels to the previous latitude and the flow oscillates around the original latitude. The overall effect of the cyclonic and anti-cyclonic rotation is to cause the disturbance to move westward. In more complex situations, such as a continuously stratified flow, the mechanism is essentially the same.

The phase velocity depends on the latitude (a Rossby wave can travel westward across the equatorial Atlantic Ocean within a period of 2 months, whereas it can travel at tropical latitudes within a period of two years), it decreases from the Equator and determines a series of small and large-scale phenomena with oceanographic, biological and climatological implications. Oceanic Rossby waves are an important means which transfer heat and communicate climatic changes due to variability in the wind and buoyancy forcing.

Unlike the Kelvin waves, Rossby waves are much slower and propagate zonally westward. Kelvin and Rossby waves are part of a huge natural

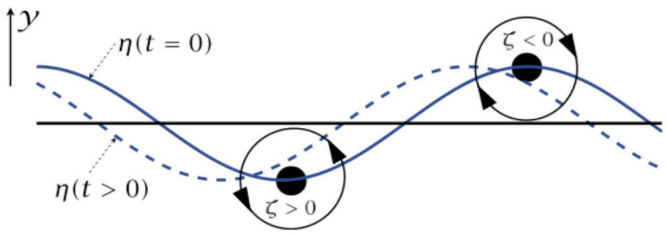

Figure 2.17: The mechanism of a two-dimensional (x-y) Rossby wave. An initial disturbance displaces a material line at constant latitude(the straight horizontal line) to the solid line marked η (t=0). Conservation of potential vorticity, $\beta y + \zeta$, leads to the production of relative vorticity, as shown for two parcels. The associated velocity field (arrows on the circles) then advects the fluid parcels, and the material line evolves into the dashed line. The phase of the wave has propagated westwards (Vallis, 2006)

integrated communication system of the oceans for the heat exchanges and energy transmission, commonly called *teleconnection mechanism.*

2.3.1 Waveguides and teleconnection processes

In the previous section the existence and propagation of the Kelvin waves was discussed; how they rely to gravity, Coriolis acceleration and the presence of a waveguide (vertical meridional boundaries or the equator). Here we discuss the waveguide, which is a structure that confines waves propagation. Disturbances are confined within the waveguide due to total or partial reflection from the vicinity of the coasts or the Equator (fictitious "wall" of the waveguide). For instance, coastal boundaries act as a waveguide for the propagation of coastal Kelvin waves and the equatorial band, within $\pm 5°$ from the equator, acts as a waveguide for waves propagating parallel to the equator such as equatorial Kelvin and Rossby waves.

Matsuno (1966) stressed that the equatorial area of the tropical oceans acts as a waveguide for a set of equatorial waves that propagate eastward (equatorial Kelvin waves) and westward (equatorial and mid-latitude Rossby waves). A decade later, Adamec and O'Brian (1978) showed, by the means of a linear model, on an equatorial β-plane, that an increase in the south-east Trades, in the western Atlantic Ocean, excites an equatorially trapped Kelvin wave which, in turn, propagates eastward along the

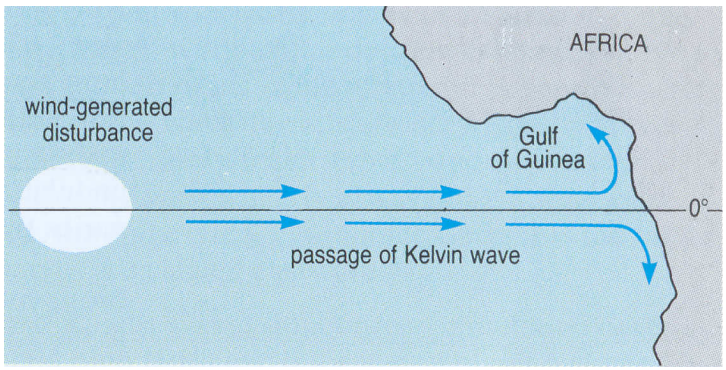

Figure 2.18: A disturbance in the west side of the basin may be generated in the Atlantic Ocean and travels eastwards as an equatorial Kelvin wave; at the eastern boundary, this splits in to two coastal Kelvin waves (Colling and CourseTeam, 2002)

equator. Then, a comprehensive mechanism, triggered by changes of the wind regime, was identified. When an equatorial Kelvin wave reaches the eastern boundary, radiation of energy occurs through radiation of Rossby waves, reflected from the eastern boundary (Gill, 1982), and propagation of coastal Kelvin waves, which leave the equatorial area and propagate poleward in both hemispheres (Fig. 2.18). The reflected Rossby waves, when reaching the western boundary, can then potentially trigger a new Kelvin wave at the western equatorial region.

This system of consecutive waves, running through the tropical Atlantic, establishes a connection between zonal and meridional borders of the basin. Waves carry energy around the basin and drive the seasonal and annual adjustment of the ocean to the wind-stress forcing. Such a phenomenon, known as *teleconnection*, was proposed by (McCreary, 1976) in the context of El Niño dynamics. Since the satellite altimetry has become available, these results were validated (TOPEX/POSEIDON was launched in 1992) and several papers were devoted to the investigation of the nature of the inter-seasonal sea surface height (SSH) signal and its contribution to the teleconnection processes within the tropical area of the Atlantic Ocean (Adamec and O'Brian, 1978; Moore et al., 1978; Polo et al., 2008).

3

Dynamical equations and model approach

The mathematical description of the oceanographic wind-driven dynamics requires the application of the equations of motion for a material volume element [1] in a fluid. The Navier-Stokes equations, whose derivation may be found in a number of fluid-dynamics texts (e.g. Batchelor, 1967, Gill, 1982 and Vallis, 2006), represent a generic problem of motion for a fluid element. They state the equality between the rate of change of momentum of the volume element and the net force acting on it. In the first section the Navier-Stokes equations and their approximation, for oceanographic applications, through the shallow water model are presented. The second section elucidates the model approach adopted in this research work.

3.1 The Navier-Stokes equations

The Navier-Stokes equations for an incompressible fluid can be formulated as follows

[1] deformable volume of fluid

$$\frac{\partial u}{\partial t} + u\frac{\partial u}{\partial x} + v\frac{\partial u}{\partial y} + w\frac{\partial u}{\partial z} = -\frac{1}{\rho}\frac{\partial p}{\partial x} + \frac{\mu}{\rho}\left(\frac{\partial^2 u}{\partial x^2} + \frac{\partial^2 u}{\partial y^2} + \frac{\partial^2 u}{\partial z^2}\right) \tag{3.1a}$$

$$\frac{\partial v}{\partial t} + u\frac{\partial v}{\partial x} + v\frac{\partial v}{\partial y} + w\frac{\partial v}{\partial z} = -\frac{1}{\rho}\frac{\partial p}{\partial y} + \frac{\mu}{\rho}\left(\frac{\partial^2 v}{\partial x^2} + \frac{\partial^2 v}{\partial y^2} + \frac{\partial^2 v}{\partial z^2}\right) \tag{3.1b}$$

$$\frac{\partial w}{\partial t} + u\frac{\partial w}{\partial x} + v\frac{\partial w}{\partial y} + w\frac{\partial w}{\partial z} = -g - \frac{1}{\rho}\frac{\partial p}{\partial z} + \frac{\mu}{\rho}\left(\frac{\partial^2 w}{\partial x^2} + \frac{\partial^2 w}{\partial y^2} + \frac{\partial^2 w}{\partial z^2}\right) \tag{3.1c}$$

$$\frac{\partial u}{\partial x} + \frac{\partial v}{\partial y} + \frac{\partial w}{\partial z} = 0 \tag{3.1d}$$

where, on the left side of the equations of motion (3.1), the total derivative evaluates the acceleration of each component of the velocity vector $\mathbf{u}$. Using the vector notation, while the first term $\partial\mathbf{u}/\partial t$ (local derivative) takes into account the temporal variation of the velocity field, evaluated in a specific point of a frame of reference, the terms $(\mathbf{u}\cdot\nabla)\mathbf{u}$ (advective terms of the total derivative) define the spatial variation of the velocity field, experienced only as the fluid parcel moves. On the right side of (3.1), the pressure gradient force $-1/\rho\nabla p$, where ρ is the fluid density, takes into account the variations of the pressure in the space, and the viscous forces per unit volume are approximatively equal to $\mu/\rho\nabla^2\mathbf{u}$, where μ is the dynamic viscosity of the fluid. In the equation (3.1c) g is the gravity acceleration. While the *equations of motion* (3.1a), (3.1b) and (3.1c) are the expression of the Newton's second law [2], the *continuity equation* (3.1d) states the condition of mass conservation for incompressible fluids.

In order to apply such equations for oceanographic purposes a number of assumptions must be introduced. Indeed, it should be borne in mind that the oceans flows are highly turbulent and their motions, within the entire spectrum of length scales, involve several complex physical mechanisms. For these reasons simplified physical models, which stress the essential processes, are often designed with the aim of helping the understanding of low-frequency phenomena. This is the case of the shallow water model approximation, very common for wind-driven model studies of the oceanic variability.

[2] the total force applied on a body is equal to the time derivative of momentum of the body

3.1.1 The shallow water approximation

The shallow water model describes the dynamics of a thin homogeneous layer of fluid in hydrostatic balance. On the top, a free surface is supposed to be an interface between the layer and another fluid of negligible inertia, conversely, the bottom can be a flat or rough rigid surface. The horizontal scale of the motion is supposed to be a much greater than the layer depth. This assumption represents a very good approximation for the large-scale ocean dynamics. Indeed, in the observed ocean the horizontal length scale of the motion is very huge when compared with the vertical length scale. Moreover, this model leads to a simplification of the momentum and the mass continuity equations through a reduction of the number of equations and variables.

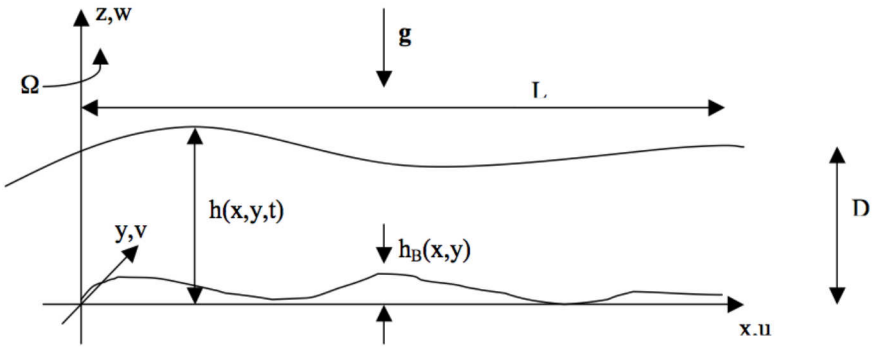

Figure 3.1: A shallow water system. $h(x, y, t)$ is the mean thickness of a water column. The oceanic bottom is defined by $z = h_b(x, y)$ and the free surface is defined by $z = D + \eta(x, y, t)$, where $\eta(x, y, t) = h(x, y, t) - D$. From Pedlosky, 1987

Derivation

The key condition which characterizes the shallow water model is

$$\delta = \frac{D}{L} \ll 1$$

where D is assumed to be the typical length scale for the vertical motion and L the typical horizontal length scale for a particular phenomenon, i.e., the aspect ratio of the motion is small. Such condition implies that, the vertical velocity cannot be larger than the horizontal one and consequently the vertical accelerations can be negligible with respect to

the horizontal accelerations (this in turn implies the hydrostatic balance). Let us assume that the rotation axis of the fluid coincides with the z-axis in the model and the effective Coriolis force has component $2\,\overrightarrow{\omega} \times \overrightarrow{u} = (-fv, fu, 0)$. Start with the mass conservation equation for an incompressible fluid of constant density .

$$\frac{\partial u}{\partial x} + \frac{\partial v}{\partial y} + \frac{\partial w}{\partial z} = 0 \tag{3.2}$$

If U and W are the characteristic scale for the horizontal and vertical velocity, respectively, and L is the horizontal length scale for the motion, it follows that the scale of the first two terms in (3.2) is O(U/L). Moreover the scale for the third term O(W/D) cannot be larger than O(U/L), that is, $W \leqslant (\delta U)$, which represent an upper bound on vertical velocity.

If one estimates the order of magnitude of each term the momentum equation (3.3)

$$\frac{\partial u}{\partial t} + u\frac{\partial u}{\partial x} + v\frac{\partial u}{\partial y} + w\frac{\partial u}{\partial z} = +fv - \frac{1}{\rho}\frac{\partial \tilde{p}}{\partial x} \tag{3.3a}$$

$$\frac{U}{T} \quad \frac{U^2}{L} \quad \frac{U^2}{L} \quad \frac{UW}{D} = fU \quad \frac{P}{\rho L} \tag{3.3b}$$

$$\frac{\partial v}{\partial t} + u\frac{\partial v}{\partial x} + v\frac{\partial v}{\partial y} + w\frac{\partial v}{\partial z} = -fu - \frac{1}{\rho}\frac{\partial \tilde{p}}{\partial y} \tag{3.3c}$$

$$\frac{U}{T} \quad \frac{U^2}{L} \quad \frac{U^2}{L} \quad \frac{UW}{D} = fU \quad \frac{P}{\rho L} \tag{3.3d}$$

$$\frac{\partial w}{\partial t} + u\frac{\partial w}{\partial x} + v\frac{\partial w}{\partial y} + w\frac{\partial w}{\partial z} = -\frac{1}{\rho}\frac{\partial \tilde{p}}{\partial z} \tag{3.3e}$$

$$\frac{W}{T} \quad \frac{UW}{L} \quad \frac{UW}{L} \quad \frac{WW}{D} = \quad \frac{P}{\rho D} \tag{3.3f}$$

where T is a characteristic scale for time and P is the scale for the pressure field. The total pressure p is defined as

$$p(x, y, z, t) = -\rho g z + \tilde{p}(x, y, z, t) \tag{3.4}$$

Since, by continuity $W \leqslant (\delta U)$, $UW/D = O(U^2/L)$, it follows from (3.3a) and (3.3c) that the pressure scale is given by

$$P = \rho U \left[\frac{L}{T}, U, fL\right]_{max} \tag{3.5}$$

in order that the horizontal pressure gradient might be relevant in the horizontal momentum balance; for otherwise the flow would be unaccelerated. This implies that the ratio of the terms on the left-hand side of (3.3e) to the vertical pressure gradient is bounded by the larger of

$$\rho\frac{dw/dt}{\partial\tilde{p}/\partial z} = \frac{\delta^2(1/T, U/L)_{max}}{(1/T, U/L, f)_{max}} \tag{3.6}$$

A very interesting case is for small Rossby number ($U/fL \ll 1$). In this case the vertical pressure gradient is bounded by δ^2 and, since by hypothesis $\delta^2 \ll 1$, in terms of the total pressure one has

$$\frac{\partial p}{\partial z} = -\rho g + O(\delta^2) \tag{3.7}$$

which is the hydrostatic approximation. It is possible to integrate (3.7) and obtain

$$p = \rho g(h - z) + p_{atmosphere}, \tag{3.8}$$

if $p(x, y, h) = p_{atmosphere}$. Now note that the horizontal pressure gradient is independent of z, that is

$$\frac{\partial p}{\partial x} = \rho g\frac{\partial h}{\partial x} \tag{3.9a}$$

$$\frac{\partial p}{\partial y} = \rho g\frac{\partial h}{\partial y} \tag{3.9b}$$

so that the horizontal accelerations must be independent of z, such as the horizontal velocities, if they are so initially. The horizontal momentum equations become

$$\frac{\partial u}{\partial t} + u\frac{\partial u}{\partial x} + v\frac{\partial u}{\partial y} = +fv - g\frac{\partial h}{\partial x} \tag{3.10a}$$

$$\frac{\partial v}{\partial t} + u\frac{\partial v}{\partial x} + v\frac{\partial v}{\partial y} = -fu - g\frac{\partial h}{\partial y} \tag{3.10b}$$

Since, u and v are independent of z, the equation (3.2) can be integrated in z to yield

$$w(x, y, z, t) = -z(\frac{\partial u}{\partial x} + \frac{\partial v}{\partial y}) + \tilde{\omega}(x, y, z, t). \tag{3.11}$$

It is possible to obtain the constant of the integration with the no-slip boundary condition at the bottom $z = h_b = \eta_b$

$$w(x, y, h_b, t) = u\frac{\partial h_b}{\partial x} + v\frac{\partial h_b}{\partial y}. \tag{3.12}$$

Therefore

$$\tilde{\omega}(x,y,h_b,t) = u\frac{\partial h_b}{\partial x} + v\frac{\partial h_b}{\partial y} + h_b(\frac{\partial u}{\partial x} + \frac{\partial v}{\partial y}) \tag{3.13}$$

so that

$$w(x,y,h_b,t) = (h_b - z)(\frac{\partial u}{\partial x} + \frac{\partial v}{\partial y}) + u\frac{\partial h_b}{\partial x} + v\frac{\partial h_b}{\partial y}. \tag{3.14}$$

The kinematic condition at the surface $z = h(x,y,t) = \eta(x,y,t)$ is

$$w = \frac{\partial h}{\partial t} + u\frac{\partial h}{\partial x} + v\frac{\partial h}{\partial y} \tag{3.15}$$

which, when combined with the (3.14), yields the equation of mass conservation (3.16)

$$\frac{\partial H}{\partial t} + \frac{\partial}{\partial x}(uH) + v\frac{\partial}{\partial y}(uH) = 0 \tag{3.16}$$

if $H = h - h_B$ is the total depth.

The (3.16) states that the local horizontal divergence of volume $\nabla \cdot (\mathbf{u}_H H)$ is positive and it should be balanced by a local decrease of the layer thickness, directly associated with a drop in the free surface η. If one substitutes the (3.16) into the (3.14), obtains

$$w(x,y,z,t) = (\frac{z - h_b}{H})\frac{dH}{dt} + u\frac{\partial h_b}{\partial x} + v\frac{\partial h_b}{\partial y}) \tag{3.17}$$

which implies that

$$\frac{d}{dt}\left[\frac{z - h_b}{H}\right] = 0 \tag{3.18}$$

so that the relative height from the bottom of each fluid element, $(z - h_b)/H$, is conserved following the motion of each fluid element.

The dissipation terms should be included in the momentum equations (3.10). In the context of large scale motions, as the shallow water model requires, the role of the molecular viscosity (previously commented for the Navier-Stokes equations) begin to appear less significant, within the force balance. Thus, the way in which the ocean dissipates the energy can be explained by the theory of the turbulent *cascade of energy* [3]. The RANS [4]

[3] The kinetic energy introduced at large scales will not turn quickly into thermal energy, but will feed smaller and smaller turbulent structures without any dissipation. When the size of such structures become small enough, kinetic energy will be dissipated

[4] Reynold Averaged Navier-Stokes

method formulates a optimum parameterization for the turbulent motions of the oceans. Such kind of statistical method defines two coefficients A_H and A_V, called the *horizontal* and *vertical turbulent viscosity coefficients* respectively. In the equations of motion they play the same role as the molecular viscosity in the (3.1), even if they are referred to a large-scale flow velocity. Since the details of the turbulent flow are ignored, A_H and A_V cannot be calculated, and ocean estimates can be obtained by the application of the "Prandtl theory". Typically, A_H, up to $10^5\ m^2 \cdot s^{-1}$ and A_V, up to $10^{-1}\ m^2 \cdot s^{-1}$; (Pond and Pickard, 1991). Therefore the horizontal momentum equations of the shallow water system become

$$\frac{\partial u}{\partial t} + u\frac{\partial u}{\partial x} + v\frac{\partial u}{\partial y} = +fv - g\frac{\partial h}{\partial x} + A_H\nabla_H^2 u + \frac{1}{\rho H}(\tau_{x\,wind} - \tau_{x\,bottom}) \tag{3.19a}$$

$$\frac{\partial v}{\partial t} + u\frac{\partial v}{\partial x} + v\frac{\partial v}{\partial y} = -fu - g\frac{\partial h}{\partial y} + A_H\nabla_H^2 v + \frac{1}{\rho H}(\tau_{y\,wind} - \tau_{y\,bottom}) \tag{3.19b}$$

(3.19c)

where the integrated vertical transfer of momentum is defined by the wind stress and bottom stress at the boundaries (eq. 3.20)

$$\int_{\eta_b}^{\eta} A_V \frac{\partial^2 u_i}{\partial z^2} dz = \tau|_{z=\eta} - \tau|_{z=\eta_b} = \tau_{i\ wind} - \tau_{i\ bottom} \quad i = 1, 2 \tag{3.20}$$

3.1.2 Multilayer shallow water equations

In order to extend the shallow water (SW) model (section 3.1.1) to a stratified ocean, a multilayer model, that consists of a set of superimposed SW layers of immiscible fluid, can be used. For a three layers ocean in a cartesian frame of reference, the related nonlinear primitive equations with a free surface are:

Layer I

$$\frac{\partial u_1}{\partial t} + u\frac{\partial u_1}{\partial x} + v\frac{\partial u_1}{\partial y} = +fv_1 - g\frac{\partial \eta_1}{\partial x} + A_H\nabla_H^2 u_1 + \\ + \frac{\tau_{x\,wind}}{\rho_1 H_1} - \Gamma_{x12} \tag{3.21a}$$

$$\frac{\partial v_1}{\partial t} + u\frac{\partial v_1}{\partial x} + v\frac{\partial v_1}{\partial y} = -fu_1 - g\frac{\partial \eta_1}{\partial y} + A_H\nabla_H^2 v_1 + \\ + \frac{\tau_{y\,wind}}{\rho_1 H_1} - \Gamma_{y12} \tag{3.21b}$$

$$\frac{\partial H_1}{\partial t} + \frac{\partial}{\partial x}(H_1 u_1) + \frac{\partial}{\partial y}(H_1 v_1) = 0 \tag{3.21c}$$

Layer II

$$\frac{\partial u_2}{\partial t} + u\frac{\partial u_2}{\partial x} + v\frac{\partial u_2}{\partial y} = +fv_2 - \alpha_2\frac{\partial \eta_1}{\partial x} - g_2'\frac{\partial \eta_2}{\partial x} + A_H\nabla_H^2 u_2 + \\ + \Gamma_{x12} + \Gamma_{x23} \tag{3.22a}$$

$$\frac{\partial v_2}{\partial t} + u\frac{\partial v_2}{\partial x} + v\frac{\partial v_2}{\partial y} = -fu_2 - \alpha_2\frac{\partial \eta_1}{\partial y} - g_2'\frac{\partial \eta_2}{\partial y} + A_H\nabla_H^2 v_2 + \\ + \Gamma_{y12} + \Gamma_{y23} \tag{3.22b}$$

$$\frac{\partial H_2}{\partial t} + \frac{\partial}{\partial x}(H_2 u_2) + \frac{\partial}{\partial y}(H_2 v_2) = 0 \tag{3.22c}$$

Layer III

$$\frac{\partial u_3}{\partial t} + u\frac{\partial u_3}{\partial x} + v\frac{\partial u_3}{\partial y} = +fv_3 - \alpha_3\frac{\partial \eta_1}{\partial x} - g_2'\frac{\partial \eta_2}{\partial x} - g_3'\frac{\partial \eta_3}{\partial x} + \\ + A_H\nabla_H^2 u_3 + \Gamma_{x23} - \Gamma_{x34} \tag{3.23a}$$

$$\frac{\partial v_3}{\partial t} + u\frac{\partial v_3}{\partial x} + v\frac{\partial v_3}{\partial y} = -fu_3 - \alpha_3\frac{\partial \eta_1}{\partial y} - g_2'\frac{\partial \eta_2}{\partial y} - g_3'\frac{\partial \eta_3}{\partial y} + \\ + A_H\nabla_H^2 v_3 + \Gamma_{y23} - \Gamma_{x34} \tag{3.23b}$$

$$\frac{\partial H_3}{\partial t} + \frac{\partial}{\partial x}(H_3 u_3) + \frac{\partial}{\partial y}(H_3 v_3) = 0 \tag{3.23c}$$

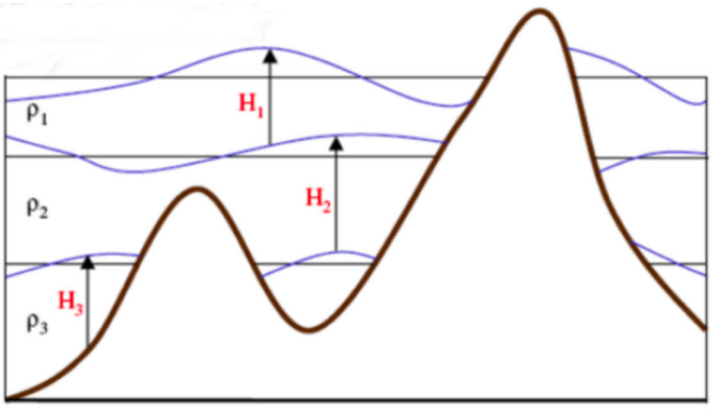

Figure 3.2: A three-layers shallow water system; H_i and ρ_i are the thickness and the density of each layer, with $i = 1, 2, 3$.

In the equations (3.21), (3.22) and (3.23) g is the acceleration of gravity, $g'_2 = g(\rho_2/\rho_1)$ and $g'_3 = g(\rho_3 - \rho_2)/(\rho_2)$ are the reduced gravity. $\alpha_2 = g\rho_1/\rho_2$ and $\alpha_3 = g\rho_1/\rho_3$; $\boldsymbol{u_i} = (u_i, v_i)$, ρ_i and H_i $(i = 1, 2, 3)$ are the upper- and lower-layer vertically averaged velocities, densities and layer thickness, respectively. η_1, η_2 and η_3 are the sea surface and two main discontinuity surfaces displacement, respectively; A_H is the lateral eddy viscosity coefficient, $\boldsymbol{\tau} = (\tau_{x\,wind}, \tau_{y\,wind})$ is the surface wind stress and the term $\Gamma_i = \gamma_i(\boldsymbol{u}_i - \boldsymbol{u}_{i+1})|\boldsymbol{u}_i - \boldsymbol{u}_{i+1}|$, where γ is the *interfacial drag coefficient*, prescribes the interfacial or bottom friction with $u_4 = 0$.

3.2 A process-oriented model approach

Several mathematical models are nowadays available for many different oceanographic studies and theoretical analyses. A classification of the various oceanographic models is proposed by Kantha and Clayson (2000). As an example, according to a geographical criterion, models may be designed for the world ocean (*global models*) or for the basin- or coastal-scales. According to the vertical discretization of the water column, one may speak of three-dimensional, *sigma-coordinate* or *layered* models and depending on the physical processes described, *dynamic*, *thermodynamic* or both models may be adopted. Such wide variety of models spans from highly sophisticated ocean general circulation models (OGCM) to extremely simplified low-order models, governed by ordinary differential

equations and implemented in box domains. OGCMs, often including data assimilation, are aimed at simulating, with the highest possible realism, most of the physical processes involved in the phenomena under study. The limit of this approach is the difficulty in identifying single, significant processes that contribute to shape the global circulation. On the contrary, the most idealized models, which are certainly unable to provide realistic information, are designed to focusing on specific aspects and neglecting others, and they may help understanding and interpreting basic physical processes (the model of Lorenz, 1963, is a classical example). Thus, the choice of a particular modeling approach heavily depends on the oceanographic applications and its advantages and disadvantages should be evaluated on a case-by-case basis.

The approach followed in this research work is intermediate between the most realistic and the most idealized modeling: we may speak of a process-oriented approach with important elements of realism. Indeed, the dynamics will be governed by a purely dynamical model (see eq. 3.21, 3.22 and 3.23). It is a relatively simple wind-driven shallow water model, that does not allow for thermohaline overturning, but certainly introduces a number of much more realistic features if compared with a low-order model. Moreover, the domain of integration will not be a box, as often done in idealized studies, but it will include important elements of realism, such as the shape of the continental boundaries (see section 3.2.3). The aim is, thus, not only to identify and interpret basic physical processes, but also to allow for comparison with real data. This approach was followed by Pierini (2006) in his implementation of the reduced-gravity shallow water equations for the study of the intrinsic low-frequency variability of the Kuroshio Extension (KE). In a subsequent study Pierini (2008) analyzed the role played by a schematic coastline along the western ocean boundary and he showed how a correct zonal extension of the domain is an important element for the formation of a relatively realistic low-frequency variability.

3.2.1 The reduced-gravity model

The model here adopted is the same reduced-gravity version of the multilayer wind-driven shallow water model governed by the equations (3.21), (3.22) and (3.23) used by Pierini (2006). Since the baroclinic motion is the only one computed by the model, this set up allows for a relatively quick responses (two orders of magnitude less then a barotropic model with free surface) and a satisfactory representations of the oceanic

dynamics especially at low latitudes.

Let us assume to retain all the stated approximations for a shallow water model (see section 3.1.1) and suppose to introduce an additional new one: it is, indeed, customary to assume that the fluid, below the main thermocline, moves much slower than that above the main thermocline. In this approximation, one assumes that the fluid in the lower layer is near quiescent. Such kind of model is called *reduced-gravity model* and, in this case study, it has only one uppermost active layer; of course, the model can also be multilayer. The model is derived by considering a two-layer shallow water system; the pressure in the upper layer is given by integrating the hydrostatic equation down from the upper surface. Thus, at a height z in the upper layer

$$p_1(z) = g\rho_1(\eta - z)$$

where η is the height of the upper surface. In the lower layer the pressure is also given by the weight of the fluid above it. Thus, at some level z in the lower layer,

$$p_2(z) = \rho_1 g(\eta - \tilde{\eta}) + \rho_2 g(\tilde{\eta} - z)$$

where $e\tilde{t}a$ is the height of the lower surface. But if this layer is said to be motionless the horizontal pressure gradient in it is zero and therefore

$$\rho_1 g\eta = -\rho_1 g'\tilde{\eta}$$

. The momentum equation becomes the (3.24) and the system is completed by the mass conservation equation (3.25). The latter equations are the governing equations for the reduced gravity model with only one active layer:

Momentum equation:

$$\frac{\partial \mathbf{u}}{\partial t} + (\mathbf{u}\cdot\nabla)\mathbf{u} + f\mathbf{k}\times\mathbf{u} = -g'\nabla\tilde{\eta} + \frac{\boldsymbol{\tau}}{\rho H} + A_H\nabla^2\mathbf{u} + \gamma\mathbf{u}|\mathbf{u}| \qquad (3.24)$$

Mass conservation equation:

$$\frac{\partial \tilde{\eta}}{\partial t} + \nabla(H\mathbf{u}) = 0 \qquad (3.25)$$

---

where $\nabla = (\partial/\partial x, \partial/\partial y, 0)$ and $\mathbf{k} = (0, 0, 1)$. $\mathbf{u} = (u, v, 0)$ is the vertically averaged horizontal velocity, $f = 2\Omega_{earth} \sin\varphi$ (where φ is the latitude) is the vertical component of the planetary vorticity and $g' = g(\rho_2 - \rho_1)/(\rho_1)$ is the reduced gravity, where ρ_1 and ρ_2 are the density of the first and the second layer of fluid, respectively. $\tilde{\eta}$ is the thermocline displacement and H represents the layers' thickness. The forcing is prescribed at the top layer by the term $\boldsymbol{\tau}/\rho H$ where $\boldsymbol{\tau} = (\tau_x, \tau_y, 0)$ is the wind stress and ρ the density of the upper layer. The dissipation in the system is provided by the scalar A_H, the lateral eddy viscosity, and by the interfacial friction, weighed by the drag coefficient γ. Nevertheless, the free surface η could be computed from the thermocline displacement $\tilde{\eta}$ through the relation $\eta = \tilde{\eta}\Delta\rho/\rho$ where ρ is the density of the layer and $\Delta\rho$ is the density jump between the two layers (the lower one being heavier). This does hold at low-latitude regions where a well defined vertical structure of the ocean is observed in contrast with midlatitudes where the wind-driven dynamics is known to be mainly barotropic and the baroclinic instability should be taken into account. Nevertheless the same model set up was used by Pierini (e.g. Pierini, 2006, 2008) for the study of the intrinsic low-frequency variability of the Kuroshio Extension (KE), with relative successful validation with altimeter data.

In this thesis the reduced-gravity model is adopted for the understanding of adjustment processes in the equatorial waveguide (see Chapter 4). Moreover a comparison with altimeter results is carried out. Finally, the possibility of adopting a two-layer shallow water model represents a next level of complexity, which leads this research towards future perspectives. Indeed, the baroclinic instability, that may be described by a two-layer model, represents one of the driving mechanisms of the Gulf Stream variability. It cannot be neglected and the inertial processes are the only simulated by the reduced-gravity model. The latter, however, is correctly applied as minimal model of the low-frequency variability in the Gulf Stream region (see Chapter 5).

3.2.2 Numerical details

The finite-difference numerical scheme used to solve the governing equations is the same developed by Pierini (1996). The mesh used is an Arakawa staggered C-grid. The numerical differencing scheme for the approximation of the differential equations (3.24) and (3.25) is an explicit[5]

[5]calculate the state of a system at a later time from the state of the system at the current time

leapfrog finite-difference scheme. The *leap-frog* scheme is a multi-step[6] method defined as follows:

$$u^{k+1} = u^{k-1} + 2\Delta t F^k + o(\Delta t^2) \tag{3.26}$$

where F^k is a function which approximates the temporal derivative of u at time $k\Delta t$.

The stability of such explicit numerical scheme depends on the Courant-Friedrichs-Lewy (CFL) condition. The latter, for one-dimensional case, states the follow relationship between the time step and the grid size in physical space

$$c\frac{\Delta t}{\Delta x} \leqslant 1$$

that is, the time step allowed for solutions is limited by the speed of propagation of the disturbance in the model (c is the gravity wave speed).
The applications proposed in Chapter 4 and Chapter 5 of this thesis require *free-slip* and *no-slip* boundary conditions, respectively. Such conditions, imposed along a closed contour lines ($\partial\Gamma$), state the normal component of the vector velocity being zero (*Free-slip conditions*) $u_{\perp\partial\Gamma}(x, y, t)|_{\partial\Gamma} = 0$ and the vector velocity being zero, (*No-slip conditions*) $\mathbf{u}(x, y, t)|_{\partial\Gamma} = 0$ respectively. The model is integrated forward in time starting from vanishes initial conditions, so that, the velocity field at the time t_0 is then prescribed as $\mathbf{u}(x, y, t_0) = 0$ and the interface displacement as $\boldsymbol{\eta}(x, y, t_0) = 0$

3.2.3 Domain of integration and wind forcing

As previously stressed, recently Pierini (2008) showed that elements of realism in the geometry of the domain of integration can play a crucial role in shaping the low-frequency variability of the Kuroshio Extension, in the boreal Pacific basin. In the framework of the process-oriented approach adopted in this research it seems reasonable to follow the same approach. Therefore, the reduced-gravity shallow water equation are solved in a domain with schematic coastal geometry. The latter is composed of a number of segments delimited by several coastal points of specific geographical coordinates. Such points are defined onto the $x-$ and $y-$ axis of the cartesian frame of reference, by mean of the mercator equal-area projection (more details will be given for each specific domain in

[6] three temporal steps

Chapter 4 and Chapter 5) [7]. The picture (3.3) provides an example of different ways to define part of the east coast, in the North America. The introduction of a schematic coastline provides a number of advan-

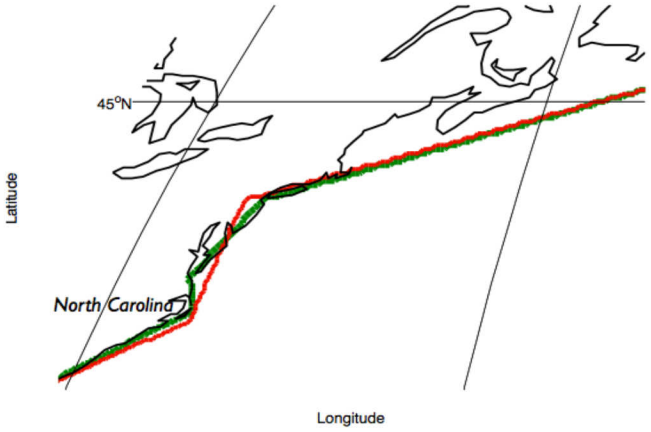

Figure 3.3: Two different way to pass from a real (black line) to schematic coastlines (red and green lines)

tages: (i) the possibility of filtering out small-scale motion induced by analogues small-scale features of the coastlines (useful when one is interested in large-scale studies),(ii) highlight the role played by the coastline in shaping the oceanic dynamics, (iii) a profound, not negligible, effect on the degree of realism of the model response (absolutely essential if any comparison with observations has to be carried out).

In the context of the present methodological approach, the degree of realism, introduced by the schematic coastline, requires the use of relatively realistic winds. Thus, zonal and meridional components of the wind velocity, provided by the European Centre of Medium-range Whether Forecasting (ECMWF), have been retrieved from the ERA-40 Re-Analysis Project and interpolated in the domain of integration. For this research, two different domains and wind forcings were implemented in the model, depending on the studied phenomena, and they will be

[7] The north-south scale is the same everywhere at the central meridian and the length of each parallel is proportional to the cosine of the latitude, it is defined by $x = (\lambda - \lambda_0)\cos\varphi$ and $y = \varphi$ where $\varphi, \lambda, \lambda_0$ are the latitude, the longitude and the central meridian respectively.

discussed in detail and separately in Chapter 4 and Chapter 5.

4

Wind-Driven dynamics in the tropical Atlantic Ocean

4.1 Introduction

Due to a number of peculiar geophysical features of low latitude regions, the tropical oceanic variability represents one of the most intriguing aspects of the global ocean dynamics. First, one should mention the vertical structure of the tropical oceans, which is characterized by a stable stratification. This implies that the variations of heat content and momentum exchanges are the main driving agents of the large-scale dynamics of the upper mixed layer. Thus, in process-oriented model studies, low-latitude oceans are usually approximated as a two-layer system, so that variations in depth of the thermocline directly reflect variations in the sea surface height (Polo et al., 2008). Moreover, in the tropical Atlantic, as well as in the tropical Pacific Ocean, the wind regime is characterized by the convergence of the prevailing Trade Winds along the ITCZ. Such winds predominantly blow from North-East and from South-East and they yield seasonal variations in intensity, driving the equatorial oceanic variability. Finally, the equator provides a waveguide for eastward propagating equatorial Kelvin waves and westward propagating Rossby waves, the latter being crucial in shaping the seasonal and interannual variability of the tropical oceans (Moore et al., 1978).

In the last two decades, satellite altimetry (e.g. Robinson, 1994) allowed one to monitor the global surface oceanic variability and, in detail, Kelvin and Rossby waves (e.g. Chelton and Schlax, 1996). The TOPEX/Poseidon mission, Ers1-2 and Jason 1-2 missions as well as EN-

VISAT mission provided altimetric measurement. Satellite altimeters are able to measure the sea surface height (SSH) down to a few centimeters with a relatively short repeat cycle on a widely-spaced ground tracks; thus, the obtained SSH data have been extensively used in several studies addressed at the understanding of the large-scale variability in the oceans. As evident from such observations and model responses (Fu and Chelton, 2001; Han et al., 2008; Philander and Pacanowsky, 1986; Polito and Sato, 2007; Polo et al., 2008), the tropical Atlantic sea level variability is dominated by the seasonal cycle because of annual variations of the wind stress. The prevailing and very energetic signature of such wind-driven seasonal variability in the tropical Atlantic is represented by the presence of annual baroclinic Rossby waves. They radiate from the eastern boundary of the basin and are shaped by the *beta*-refraction effect, due to the dependence of the phase speed with latitude. With regard to the generation mechanism of such waves (and their Pacific counterpart, which is conceptually the same system) different opinions exist: the effect of local seasonally varying winds (Hermann and Krauss, 1989; White, 1977) is opposed to the remote (nonlocal) generating mechanism (McCreary, 1976; Pierini, 2003, 2005).

In a study of the eastern Pacific variability, McCreary (1976) proposed a teleconnection mechanism that trigger the propagation of mid-latitude baroclinic Rossby waves. In that analysis the author shows that poleward propagating coastal Kelvin wave, generated in the equatorial region by wind stress anomalies, are part of the cited teleconnection. Two years later Adamec and O'Brian (1978), with the aim of understanding the remote forcing origin of seasonal upwellings along the Guinea Gulf boundaries, showed that equatorial eastward propagating Kelvin waves move poleward along the eastern boundary and produce coastal upwellings. In this framework, a teleconnection mechanism, suitable for the Pacific and Atlantic Ocean too, may be identified. As an example, in the western Atlantic Ocean wind stress anomalies may excite equatorially trapped Kelvin waves, which propagate eastward; once such waves reaches the eastern boundary (african coasts), radiation of energy occurs through reflected westward propagating equatorial Rossby waves (Gill, 1982) and coastal Kelvin waves, which propagate poleward in both hemispheres.

According to previous investigations (e.g. Moore and Philander, 1977) the local wind forcing, due to seasonal variations of the mesoscale winds, seems to play a marginal role in driving the eastern boundary dynamics. Indeed, very energetic processes take place in the eastern tropical

Atlantic Ocean and the remote forcing is thought to be the main driving mechanism. The issue addressed in this research will present evidences of the role played by a remote equatorial forcing in shaping the eastern tropical Atlantic variability. This analysis is also aimed at the understanding of the origin of the seasonal upwelling in the Gulf of Guinea: when is it caused by the coastal Kelvin waves, involved in the above mentioned teleconnection mechanism, instead of a local wind forcing?

Answers to these problems were previously provided, in the Pacific counterpart, by means of a process-oriented model approach (Pierini, 2003, 2006, 2008). In the present research a similar approach will be used. Hence, elements of realism will be introduced in the implementation of a simplified physical model, with the aim of obtaining, oceanic responses directly comparable with altimetric data. Therefore, the model is forced by wind stress fields, obtained from the ERA-40 project of the European Centre for Medium-Range Weather Forecasts (ECMWF), and the domain of integration is defined by a pseudo-realistic coastline, which reproduces the large scale features of the tropical Atlantic Ocean.

This chapter is organized as follows. In section 4.2 the mathematical model is discussed; it is a reduced gravity primitive equation ocean model, implemented in the intertropical Atlantic basin. Following subsections concern the description of the wind forcing and the domain chosen for the implementation. A reduced-gravity primitive equation ocean model is implemented in the intertropical Atlantic basin. In section 4.3 the basin-scale model response, in the form of mid-latitude baroclinic Rossby waves, is presented. The problem of their likely remote origin and the role of the $\beta - effect$ is considered by means of a series of sensitivity experiments. In section 4.4 is stressed the mesoscale prominent features of the eastern boundary dynamics with a focus on seasonal coastal upwelling along the Guinea Gulf boundary.

4.2 The mathematical model

As previously stressed in Chapter 3, the choice of a model should be carefully considered, indeed, it strongly depends on the dynamical mechanisms to be analyzed. In view of a process-oriented model study, aimed at understanding physical processes, an opportunely simplified ocean model can be a suitable tool for this research. Here we adopt a reduced-gravity, shallow-water, non linear primitive equation ocean model, which, includes the main effects related to the wind-driven oceanic variability. It consists

of a thin upper layer superimposed on a much deeper quiescent lower layer. The governing equations are given by (3.24) and (3.25), where $\mathbf{u} = (u, v, 0)$ is the upper layer horizontal velocity in the vertically average, f is correctly defined at each latitude. $g' = g(\rho_2 - \rho_1)/\rho_1$ is the reduced-gravity, $\tilde{\eta}$ is the interface displacement and H represents the layer thickness. The forcing is prescribed by the term $\boldsymbol{\tau}/\rho H$ where $\boldsymbol{\tau} = (\tau_x, \tau_y, 0)$ is the surface wind stress and ρ the density of the upper layer. The dissipation is provided by the lateral eddy viscosity coefficient A_H, and by the interfacial friction, weighed trough the drag coefficient γ.

Table 4.1: Imput parameter values

Parameter	**Value**
Depth	$H = 200\ m$
Grid size	$\Delta x = \Delta y = 20\ km$
Time step	$\Delta t = 20\ min$
reduced-gravity	$g' = 0.020\ m \cdot s^{-2}$
Boundary condition	Free-slip
Interfacial friction	$\gamma = 5 \cdot 10^{-4}$
Eddy viscosity coefficient	$A_H = 200\ m^2 \cdot s^{-1}$

It should be stressed once more that the stable vertical structure of the tropical ocean makes such model an appropriate tool of investigation. Indeed, the variable $\tilde{\eta}$, solution of the system, directly describes the variability of a thermocline, whose depth can be properly chosen. Nevertheless, a correct value for the free surface η can be indirectly computed at low-latitudes from the thermocline displacement $\tilde{\eta}$. The relation is given by $\eta = \tilde{\eta}\Delta\rho/\rho$ where ρ is the density of the layer and $\Delta\rho$ is the density jump between the two layers.

The equations are solved through an explicit leapfrog finite-difference scheme on the Arakawa C-grid, as in Pierini (1996), etc.. Table (5.2) lists the parameter values used in the present implementation. The depth of the active layer, $H = 200\,m$, is a typical depth of the mixed-layer at low-latitudes. The spatial grid steps, 20 km, are the same in both latitudinal and longitudinal, so that the model is eddy-permitting. The temporal step is $\Delta t = 20\ min$. The reduced-gravity value was derived from two mean densities, obtained, for each layer, from vertical sections of the WOCE Atlas (http://sam.ucsd.edu/). Free-slip boundary conditions are imposed along the closed boundaries and integration is carried out

starting from the state at rest. The interfacial friction $\gamma = 5 \cdot 10^{-4}$ is the same used by Pierini (2006) in a similar study on the variability of the tropical north Pacific Ocean.

This model is the same tool used in Pierini (2006, 2008) and Pierini and Dijkstra (2009). For those studies, schematic coastlines and analytical wind stress, which included a realistic spatial and temporal structure, were used. A subsequent successful comparison with altimeter data, proved the importance of including such elements of realism in the model implementation. Indeed, they have led to more realistic response of the model when compared with the solutions of other commonly used mechanistic models. This research follows that approach by introducing a schematic basin geometry, that follows the real coastline, and a fully-realistic wind stress forcing, derived from ECMWF re-analysis.

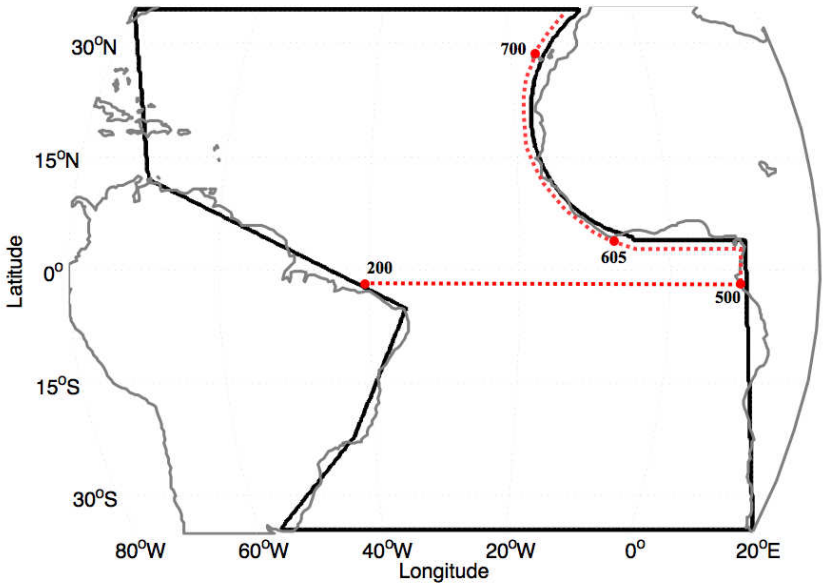

Figure 4.1: Domain of integration (black line) overlapped to real coastline (gray line) retrieved from NOAA, WCL (1:5,000,000); http://rimmer.ngdc.noaa.gov/. The red dotted line refers to the detection path used for figures 5.8 and 5.14

4.2.1 Basin geometry

In this framework, schematic coastlines, correctly representing the large-scale shape of the continental boundaries between the latitudes of 35°S and 35°N, in such a way that is the effects. The wide latitudinal range allows us to include all the main features of the tropical variability, in such a way that side effects along the North and South boundaries are minimized. The zonal width of the domain was chosen as to extend between the longitude of 80 °W and 20°E, spanning all the tropical Atlantic.

The schematic geometry, that takes into account the real geographic extension of the Atlantic basin, is composed of several segments delimited by as many coastal points of specific geographical coordinates. Such points are defined onto the $x-$ and $y-$ axis of the cartesian frame of reference, by mean of the mercator equal-area projection. The latter is defined by the relations $x = (\lambda - \lambda_0)\cos\varphi$ and $y = \varphi$ where $\varphi, \lambda, \lambda_0$ are the latitude, the longitude and the central meridian respectively. The connection between five points: $(35°S, 57°W)$, close to Montevideo, $(22°S, 39°W)$, off Rio de Janeiro, $(5°S, 35°W)$, $(12°N, 70°W)$ and $(35°N, 80°W)$ draws the contours of the western side of the Atlantic basin. To the east, a circle and a straight line join the points $(35°S, 20°E)$ and $(4°N, 10°E)$ and represent the boreal and austral Africa, respectively (Fig. 2.3).

4.2.2 Wind Forcing

If a schematic coastline correctly represents the large-scale features of the continental boundaries, it seems essential to include more realistic wind fields rather than analytical winds, extensively used for process-oriented box-model studies. Indeed, one would expect that the inclusion of realistic winds could improve the degree of realism in the model response. Thus, zonal and meridional components of the wind velocity, provided by the ECMWF, have been retrieved from the ERA-40 Re-Analysis Project with a resolution of one degree in the space and six hours in time. Recently, Polito and Sato (2007) used altimeters' time series to estimate a 13-years trend in sea surface height anomaly of the global ocean. Their anomalies evidenced very energetic Rossby waves and eddy activity, showing a trend in the amplitude of such transient events. Since Rossby waves variability is mainly driven by momentum fluxes associated with the wind, a single year (2001) of wind velocity data, which is included in the above mentioned time series, has been chosen as forcing

period for this model study.

Estimates of the zonal (τ_x) and meridional (τ_y) components of the surface wind stress have been here computed from the wind velocity through the usual bulk formula in component form:

$$\tau_x = \rho C_D u_x (u_x^2 + u_y^2)^{1/2} \quad (4.1)$$

$$\tau_y = \rho C_D u_y (u_x^2 + u_y^2)^{1/2} \quad (4.2)$$

where u_x and v_x are the zonal and meridional components of the wind speed, respectively. The 10-m neutral drag coefficient C_D formulation, of Smith (1980), has been adopted. While highly simplified models are forced with climatological wind products (e.g. Arnault et al. 1992), weekly ERS-1 and -2 wind stress (e.g. Polo et al. 2008) or monthly mean based on shipboard wind estimates, (e.g. Busalacchi and Picaut 1983), in the context of this research high frequency wind forcing is applied.

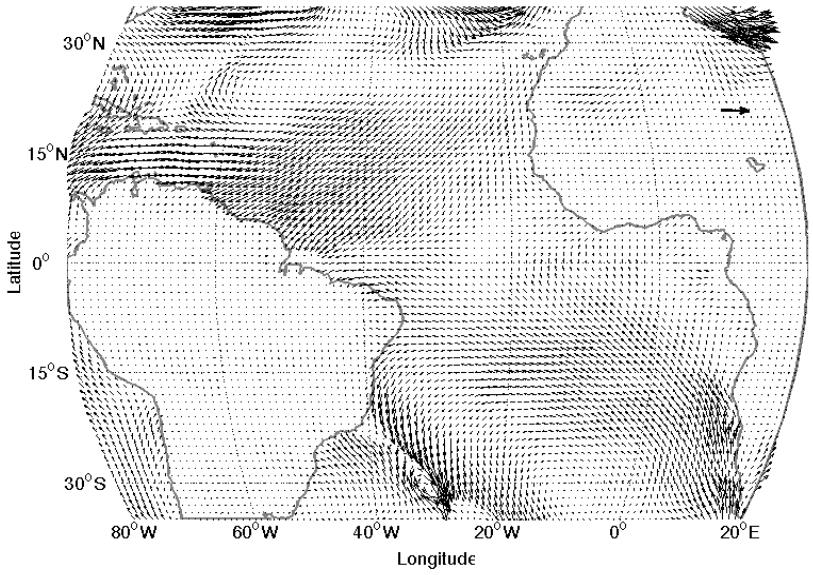

Figure 4.2: Snapshot of $\tau(x, y)$ surface wind stress at January 1^{st}, 2001, used for *EXP. A.* (unit arrow $10m\,s^{-1}$)

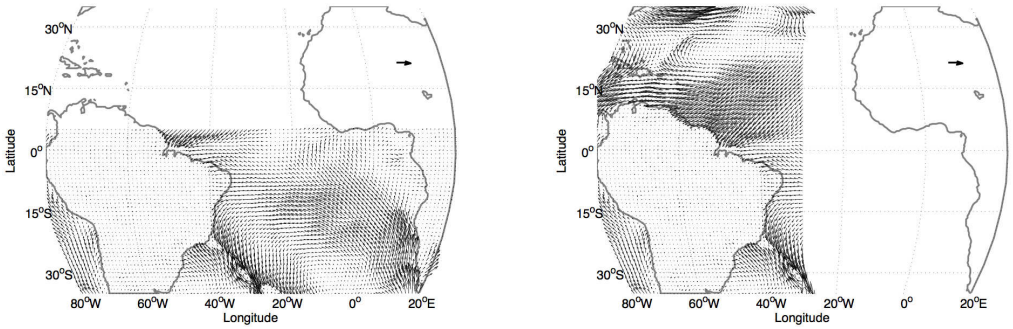

Figure 4.3: The same snapshot as in Fig. 2.4 with meridionally confined wind stress (a) and zonally confined wind stress (b), used for *EXP. B* and *EXP. C*

EOF and confined wind forcing

The wind stress data were decomposed in empirical orthogonal functions (EOF) via singular value decomposition method (see Appendix B). The patterns of variability have been computed for each wind stress component, and specific areas of the main variability were localized in the tropical Atlantic Ocean (not shown). Moreover, a truncated linear combination of the spatial patterns and their corresponding time series were used to compute a new wind stress data set as follows:

$$\widetilde{\tau}(x_i, t_n) = \sum_{k=1}^{s} a_k(t_n) u_k(x_i) \tag{4.3}$$

where $\widetilde{\tau}(x_i, t_n)$ is the truncated wind field and $a_k(t_n)$ are the amplitudes of the orthogonal functions $u_k(x_i)$. Indeed, it is possible to reconstruct the wind stress fields involving only a limited number of bases functions of the EOF decomposition. The functions, which retain most of the variance explained by the data, were used to obtain new wind stress fields, in order to force the model with a more spatially and temporally smoothed wind. In this way, lower or higher frequencies of the wind variability can be transfered in the model response and several sensitivity experiments can be performed (not showed).

Moreover, different sensitivity experiments (see Table 4.2), in which the wind stress forcing is confined to specific latitudinal bands including

the equator and longitudinal bands, have been performed in this chapter (see confined wind stress forcing in Fig. 4.3a and Fig. 4.3b). The aim of such experiments is to find, in the Atlantic Ocean, similar results as in Pierini (2003) for the Pacific counterpart, where was found that the seasonal wind-driven variability is determined in a narrow latitudinal belt very few degrees around the equator.

Table 4.2: List of the performed experiments

Wind forcing design	**Expriments**
Full wind forcing, Fig. (2.4)	*EXP. A*
Meridionally confined wind forcing, Fig. (4.3a)	*EXP. B*
Zonally confined wind forcing, Fig. (4.3b)	*EXP. C*

4.3 Basin-scale model response

The present section concerns the analysis of the seasonal variability of the large- and meso-scale oceanic circulation. The momentum flux associated with the winds is known to be the main forcing mechanism for large-scale variability within such seasonal periodicity. Moreover, significant momentum exchanges are mainly located in the upper mixed layer so that tropical oceans can be approximated as a two layer system. In this chapter all the figures display the SSH variability, obtained, as previously stressed in section 3.2.1, from the reduced-gravity model response, through the relation $\tilde{\eta} = \eta\Delta\rho/\rho$; moreover, if otherwise stated, all the figures represent the response of the reference experiment (Exp. A), in which the wind stress is prescribed over the entire domain. Maps of absolute dynamic topography (SSH with respect to the geoid) derived from satellite altimeter products (developed by Ssalto/Duacs and distributed by Aviso, with support from Cnes; http://www.aviso.oceanobs.com/duacs/) are also showed: they will be used for direct comparison with the model response.

Figure (4.4) and (4.6) show the $\lambda - t$ diagrams (where λ are degrees of longitudes) of the absolute dynamic topography (ADT) during 2001 and along zonal sections, at latitudes of $\phi = 20°N$ and $\phi = 10°N$, respectively. This altimetric signal provides an observational evidence that Rossby waves are emanating from the eastern boundary. Their zonal length scale, associated with the westward penetration, decreases with

increasing latitude and the inclination of the isolines describes their westward propagation during the year. While at $20°N$ the signal is zonally confined at around $40°W$, at the same time Rossby waves travel up to $50°W$ at the lower latitude of $10°N$. Similar results have been obtained by means of the *Exp. A* model implementation (see Fig. 4.10 and Fig. 4.9). If compared with observations in Fig. (4.4) and (4.6), the simulated signal shows the same phase and the same westward penetration. Of course a number of features are not reproduced by the model response due to the simplified dynamics taken into account. The eddy activity is not adequately represented and the role of the oceanic bottom topography is neglected in shaping Rossby waves propagation.

Figure (4.8) is also qualitatively comparable with the picture of ADT in the same area (Fig. 4.7); they represent annual average of the SSH, obtained from the model response and altimeter satellite, respectively. Fig. (4.8) yields a deficit of surface water in the east and a corresponding run up in the west equatorial region, induced by the prevailing winds. The equatorial divergence is bounded in the northern and southern hemisphere by mid-latitude Rossby waves.

The location of the main surface currents, within the Atlantic equatorial current system, should be also considered. Based on the distribution of the SSH (Fig. 4.8), the North Equatorial Current is located between 20 °N and 7 °N and the North Equatorial Contourcurrent is confined within 7 °off the Equator in the northern hemisphere. The South Equatorial Current, with its westward flowing current, is broad and it is bounded by latitudes of 4 °N and 15 °S; all these estimates provide a validation of the model setup and show a basic agreement with literature, observations and OGCM response.

In the following sections, the reasons of the different westward penetration of Rossby waves (section 4.3.1) will be considered and the identification of local and remote forcing, as generation mechanisms of such waves (section 4.3.2) will be analyzed.

4.3.1 β-refraction

Within the tropics, Rossby waves yield different patterns (Fig. 4.7) and periodicity in the southern and in the northern hemisphere. Indeed, during the year, two Rossby waves emanate from the southern eastern boundary while a single strong wave leaves the eastern boundary in the north hemisphere (Fig. 4.6 and 4.5). Differences in the shape of the patterns can be due to distinct cells of the overlaying positive wind stress

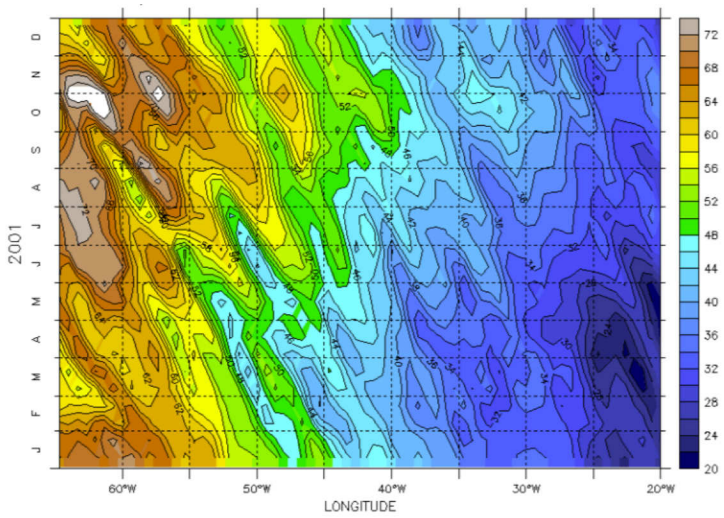

Figure 4.4: $\lambda - t$ diagram at $\phi = 20^{\circ}N$ of satellite derived Absolute Dynamic Topography Merged (amplitude: cm), http://www.aviso.oceanobs.com/

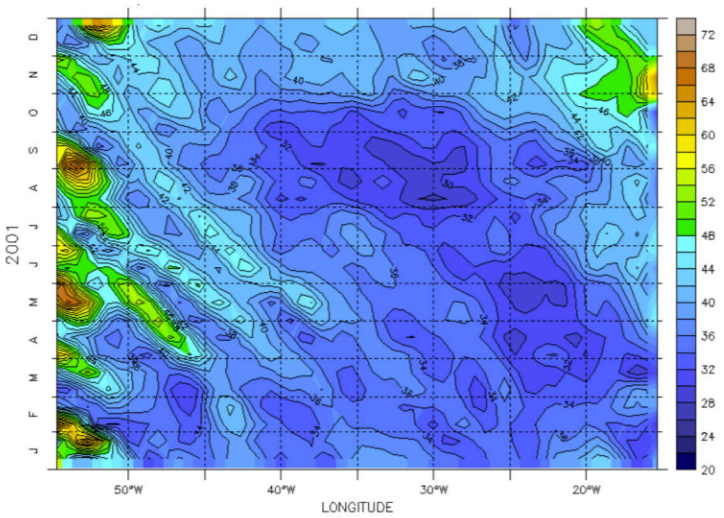

Figure 4.5: $\lambda - t$ diagram at $\phi = 10^{\circ}N$ of satellite derived Absolute Dynamic Topography Merged (amplitude: cm), http://www.aviso.oceanobs.com/

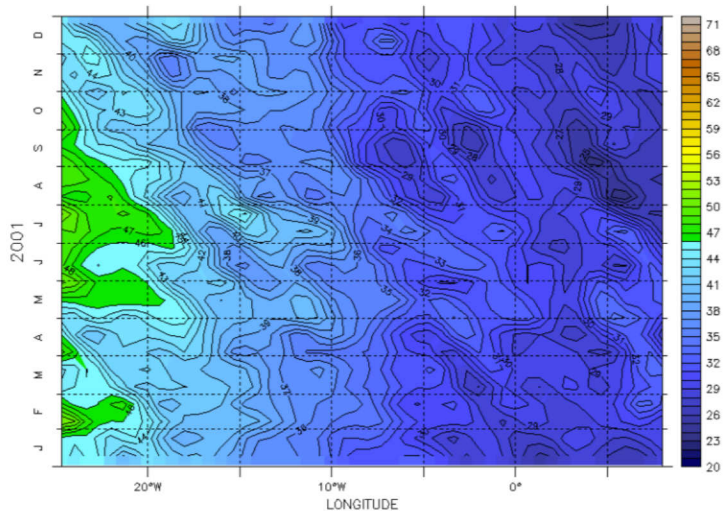

Figure 4.6: $\lambda - t$ diagram at $\phi = 10^{\circ}S$ of satellite derived Absolute Dynamic Topography Merged (amplitude: cm), http://www.aviso.oceanobs.com/

curl, which is driving the Ekman pumping, in the northern and southern tropical area. The different periodicity of their generation from the eastern boundary depends, instead, on the shape of the african coastline. The latter does not yield similar features in both hemisphere and it affects the generation mechanism of mid-latitude Rossby waves, as it will be shown in the next section.

Figure (4.8) shows a snapshot of the SSH fields, as obtained from the model response, which mirrors the pycnocline displacement. As previously stressed it yields the prominent signature of baroclinic mid-latitude Rossby waves. The large latitudinal extension of Rossby waves makes them feel different values of planetary vorticity. Due to the existence of such planetary vorticity gradient, after having left the eastern boundary toward the west, a wave packet of Rossby waves undergoes a refraction toward the equator, such effect being known as beta refraction (Chelton and Schlax, 1996; White, 1977). This refraction generates wide western gaps in which Rossby waves cannot penetrate, and such confinement was analyzed by Pierini (2005) in the frequency space.

For equivalent studies, on the Pacific domain, Pierini 2003, 2005 interprets the beta-refraction signature by observing that the offshore scale of the response, for forcing frequencies higher than the Rossby cutoff frequency $\overline{\omega} = -\beta R_i/2$ (the maximum frequency for which Rossby waves can exist), is the internal Rossby deformation radius $R_i = \sqrt{g'D}/f$, on the contrary, for lower forcing frequencies, such offshore scale is equal to the

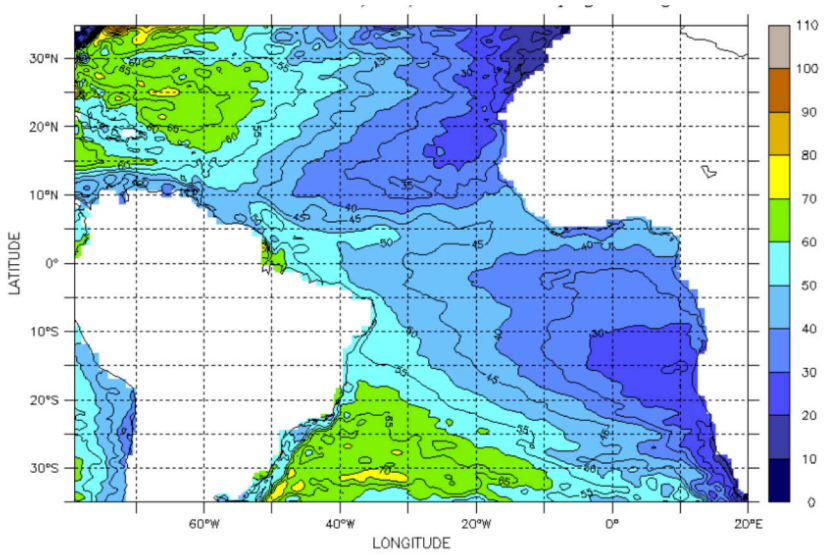

Figure 4.7: Annual mean (2001) of satellite derived Absolute Dynamic Topography Merged (amplitude: cm), http://www.aviso.oceanobs.com/

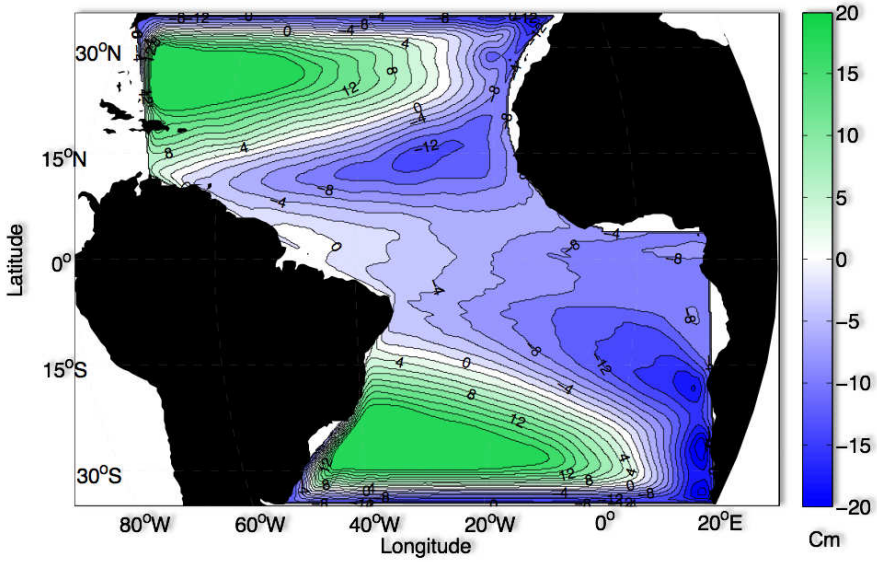

Figure 4.8: SSH as obtained from the model response, snapshot at t=5 days (amplitude: cm)

distance covered by Rossby wave during a period. Indeed, for intertropical latitudes, where the cutoff period is around 1 year, the westernmost isoline of the Rossby wave signature obtained by the model response, is located at a distance from the eastern boundary about equal to $d = c_g T$, where T represents the annual period and c_g is the zonal component of the group velocity. The latter is given by $c_g \approx c_p \approx -\beta R_i^2$, nearly equal to the phase velocity because, at intertropical latitudes, baroclinic Rossby waves are virtually nondispersive. For instance, at 10 °N, a theoretical value for the offshore distance is $d = 4015\,km$, which is in basic agreement with the estimate from the model response, as shown by the overlaid white arrow in figure (4.11); the same approach can be adopted for estimates at 15 °and 20 °N (Fig. 4.10 and 4.9).

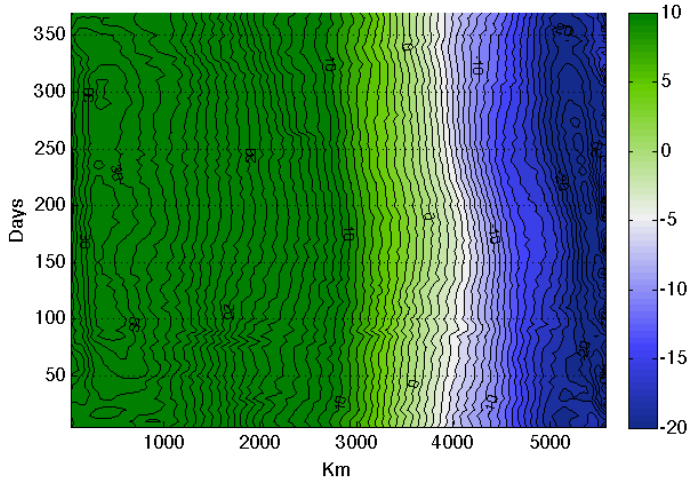

Figure 4.9: SSH as obtained from the model response, $x - t$ diagram at $\phi = 20°N$ (amplitude: cm)

4.3.2 On the origin of mid-latitude Rossby waves

A teleconnection mechanism, triggering the eastern tropical Pacific Ocean variability, was proposed by (McCreary, 1976). When an equatorial Kelvin wave reaches the eastern boundary, Rossby waves reflect from the eastern boundary and poleward propagation of coastal Kelvin waves occurs in both hemispheres; in turn, such coastal signals act as forcing for westward-propagating midlatitude Rossby waves.

In the tropical Atlantic basin, Polo et al. (2008) quantified, by means

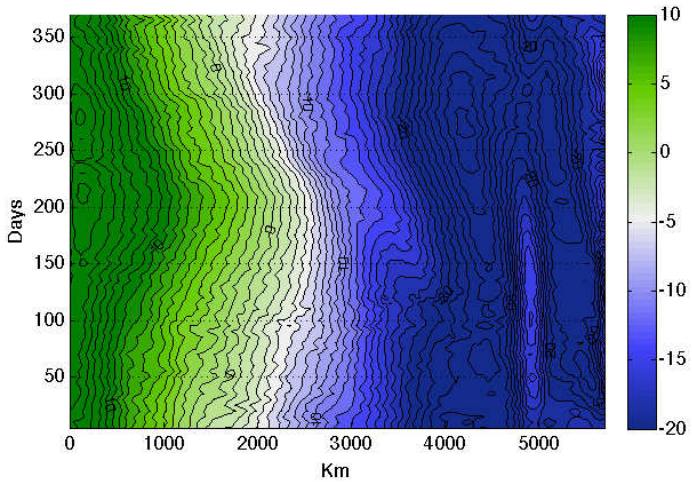

Figure 4.10: SSH as obtained from the model response, $x-t$ diagram at $\phi = 15^{\circ}N$ (amplitude: cm)

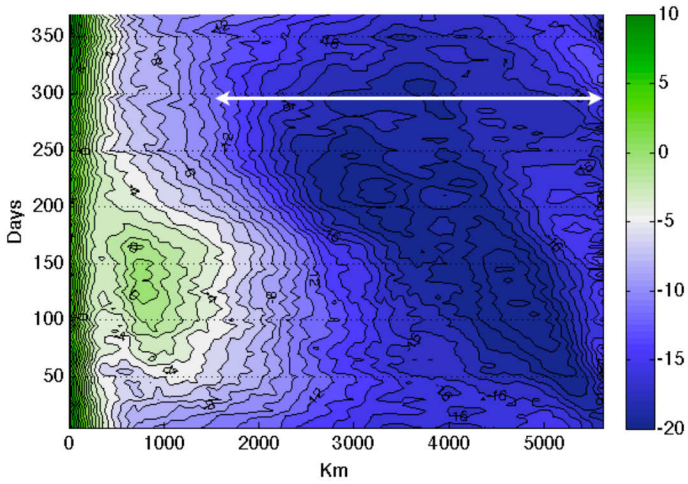

Figure 4.11: SSH as obtained from the model response, $x-t$ diagram at $\phi = 10^{\circ}N$ (amplitude: cm)

of SSH satellite TOPEX/Poseidon observation and an OGCM, how SSH intraseasonal variability along the eastern boundary is remotely controlled by wave propagation. They observed a teleconnection between the equator and low-latitude regions, whose influence appears to break down beyond 12°of latitude, suggesting other types of coherent local forcing. The same dynamical mechanism is identified in the present study by means of a purely dynamic reduced-gravity model. An hovmöller $(\phi - t)$ diagram of the SSH (Fig. 4.13), along the equator and the northwest african coast (see Fig. 2.3 for detection path), highlights that equatorial Kelvin waves are propagating along the equator and, once they reach the african coast, away from it (in this case towards the North). The coastal waves phase speed can be evaluated from the isoline inclination; empirical values, obtained in this way, correspond to $c = 1.42\, m\, s^{-1}$. This value is in basic agreement with the theoretical value, which is equal to $c = 1.97\, m\, s^{-1}$ and obtained from the relation $c = \sqrt{g' D}$. The tele-

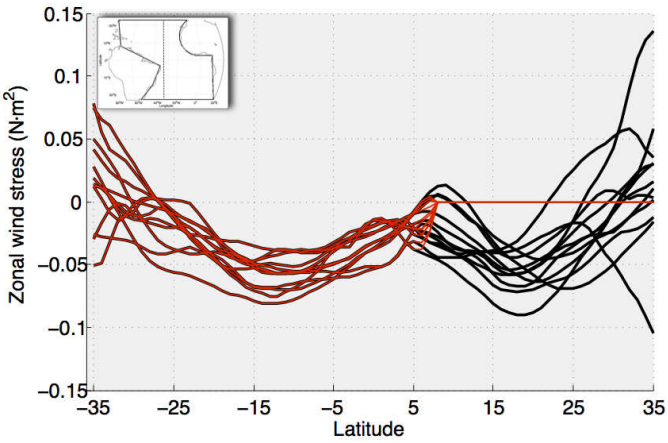

Figure 4.12: $\lambda = 35°W$ meridional section; black lines represent monthly means of the amplitude of the zonal wind stress forcing used for *Exp. A*; overlapped red lines represent the same signals meridionally confined at 5 °N, used for *Exp. B*

connection mechanism and its role in promoting westward propagating Rossby waves is clearly identified by means of a sensitivity experiment in which the wind stress forcing has been meridionally confined at 5 °N and, therefore, smoothly set to zero (*Exp. B*). Fig. 4.12 shows meridional

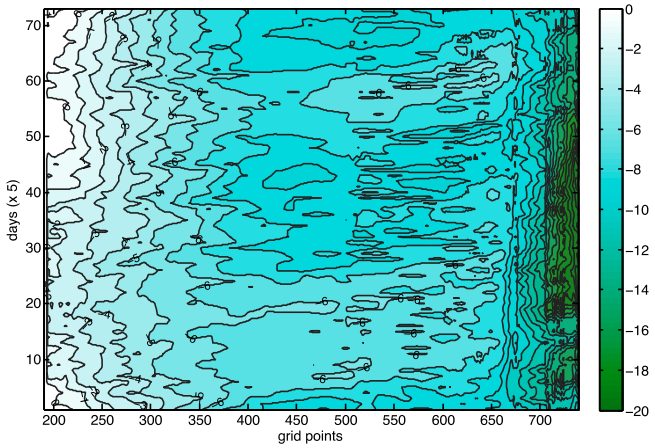

Figure 4.13: Hovmöeller diagrams of the model response (*Exp. A*) along the equator and the northern african coast; SSH (cm) following the track of figure 2.3.

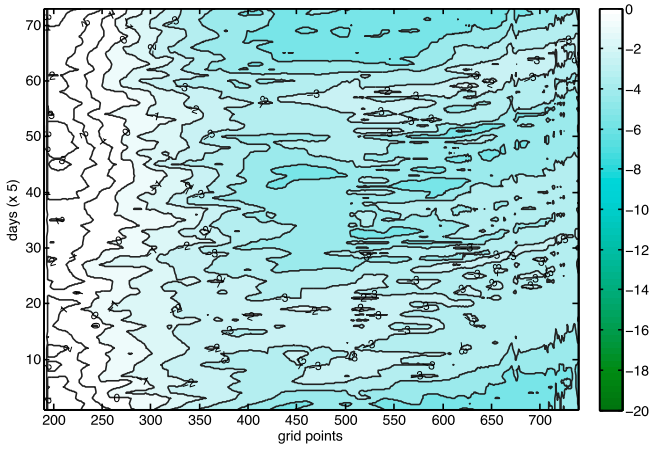

Figure 4.14: The same as in figure 5.8, the model response refers to experiment *Exp. B*

sections, at 35 °W, in which the black lines represent monthly means of the wind stress and the red overlapped lines the same wind, meridionally confined at 5 °N. Thus, the continuous propagation of Kelvin waves, from the western side of the equator up to 35 °N of latitude can be identified by figure 4.14; it represents the model response from *Exp. B*, in which the effect of local winds is not take into account at latitudes higher than 5 °N. Differently from the results of Polo et al. (2008), a comparison between figures (4.14) and (4.13) underline the prevalent effect of the local forcing beyond 17 °N.

Figure (4.15a) and (4.15b) show the $x-t$ diagrams of the SSH along the $\phi = 10°N$ zonal section as given by experiments *Exp. A* and *Exp. B*, respectively. Fig. (4.15) shows, in the left panel, the westward propagation of mid-latitude Rossby waves, as explained in section 4.3.1; in the right panel, SSH evolution yields westward propagating signals, however, such model response does not include the effect of local wind forcing. This implies that a remote forcing, due to poleward propagating coastal Kelvin waves, would be the only mechanism able to generate mid-latitude Rossby waves. Indeed, for the Pacific counterpart, also Pierini (2003) elucidated how the passage of Kelvin waves at the eastern boundary excites mid-latitude Rossby waves.

The difference between the SSH evolution obtained from *Exp. A* and *Exp. B* emphasize the effective role of local wind forcing in shaping the mid-latitude Rossby wave field (Fig. 4.16). Along this section $\phi = 10°N$, local winds affect the oceanic variability. Wind effects are very strong during the boreal summer within a range of 110 days (160-270) and may affect the model response in both, eastern boundary and mid-basin region, with different intensities. Indeed, the temporal evolution of the wind stress curl, detected at the same latitude (Fig. 4.16b), yields an optimal correlation with SSH variability displayed in figure (4.16a), showing that the role of the induced Ekman pumping is not negligible. Thus, the local forcing is able to profoundly modify the large-scale shape of Rossby waves and their zonal penetration towards the western boundary of the Atlantic basin.

4.4 Eastern boundary dynamics

Coastal upwelling is one of the most prominent phenomenon that take place along the eastern boundaries of the main oceans, where warm nearshore surface water is replaced by cold water from below. Alongshore

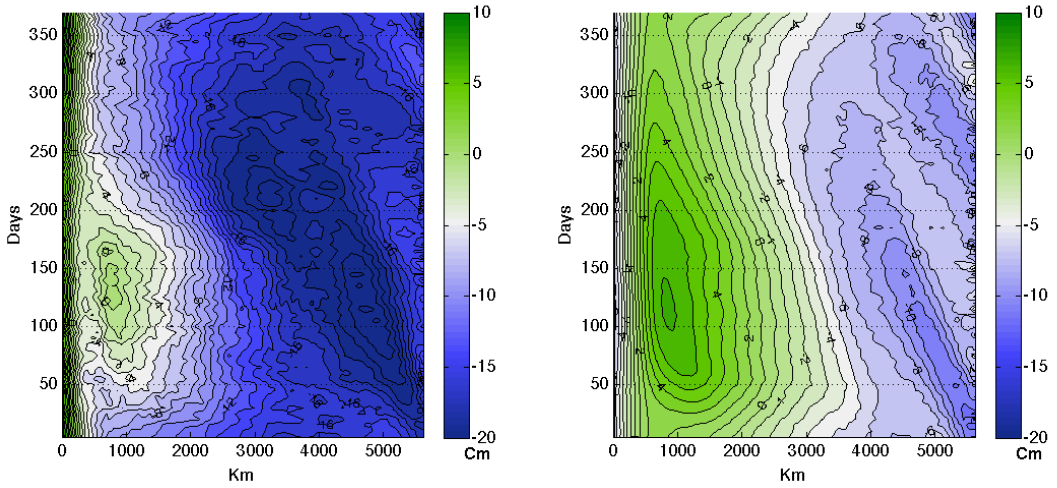

Figure 4.15: Left panel (a): SSH $x-t$ diagram at 10 °N of the model response from *Exp. A*. Right panel (b): SSH $x-t$ diagram at 10 °N of the model response from *Exp. B* (amplitude: cm).

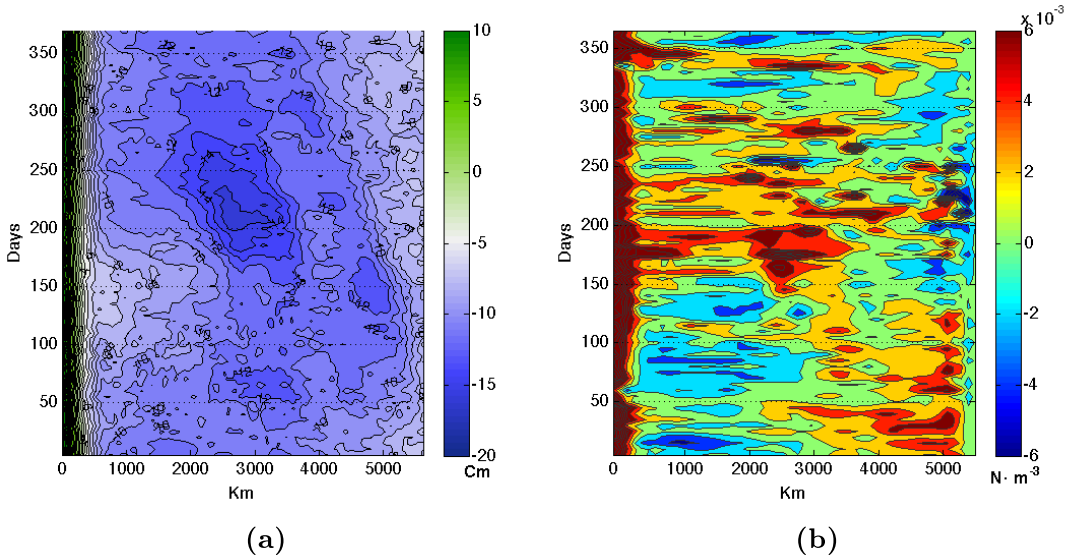

Figure 4.16: Left panel (a): SSH $x-t$ diagram at 10 °N representing the difference (*Exp. A-Exp. B*), i.e. the effect of the Ekman pumping (amplitude: cm), directly comparable with right panel (b) representing the wind stress curl over the same section for the same temporal range (amplitude: $N\,m^{-3}$).

winds may induce strong coastal upwelling through offshore Ekman drifting of surface water, so that deep water, rich of minerals, rises up and promotes biological production.

In the southern hemisphere, the Atlantic Ocean presents strong upwelling events affecting Angola, Namibia and South Africa all year round. Similar features are present in the northern hemisphere as well, indeed, Morocco, Mauritania, Senegal and Gambia, exhibit upwelling due to the persistence of the wind forcing, together with the favorable meridional orientation of the coastline.

Another important upwelling area is located along the northern boundary of the Gulf of Guinea. Upwelling events, in this area, display a seasonal periodicity, as they occur every summer from early July through September. Coastal winds are known to be the main forcing of alongshore upwellings; nevertheless, local winds appear to be inadequate to explain the Guinea Gulf seasonal upwellings. Houghton (1976) confirmed that no significant correlation between the coastal wind and observed upwelling exists in that region. In this context Adamec and O'Brian (1978) suggested that Kelvin waves propagating along the equator would be a remote driving mechanism for the Guinea Gulf seasonal upwelling. Recently, Polo et al. (2008) showed Hovmöller diagrams of the satellite derived SSH along the equator and the northern (southern) african coast for the 1993-2000 period. Positive and negative signals alternate during each year, confirming the poleward propagation of coastal Kelvin waves. Although, not all the signals show continuity from the equator to the african coast, the majority of coastal Kelvin waves start at the african coast and leave the equator propagating all around the northern and meridionally oriented boundary of the Guinea Gulf. The same authors show a climatology of the intraseasonal SSH anomalies and estimate the propagation speed to be 1.4-1.8 $m\,s^{-1}$.

The shape of the western african coasts, as well as the local winds, represents another basic component of the oceanic variability, affecting upwellings and their local and remote generation mechanism. In the southern hemisphere, between the equator and 35 °S, the african coastline is meridionally oriented, therefore, southward propagating coastal Kelvin waves can quickly leave the equatorial region using the coast as waveguide. In the northern hemisphere, between 35 °N and 4 °N, the african coastline exhibits a meridional orientation, but the coastline of the Gulf of Guinea, between 4 °N and the Equator, is characterized by a zonally oriented coastline, along 4 °North. Due to such configuration of

the coastline, Kelvin waves are confined at the near-equatorial region for a longer time than in the southern hemisphere. Moreover, the Kelvin wave amplitude is significant only within an e-folding distance of the order of the Rossby radius of deformation $R = (c/f)^{1/2}$, where $c = (g'D)^{1/2}$ is the baroclinic wave speed and f the Coriolis parameter at the local latitude. Therefore, the role of the coastal kelvin waves in shaping the thermocline and, in turn , induce coastal upwelling (or downelling) become marginal with increasing latitude.

In the next section, a sensitive experiment (*Exp. C*) is proposed with the aim of clarifying the role of the remote and local forcing in generating upwelling events along the eastern Atlantic boundaries; an analysis on the frequency of occurrence will also be carried out.

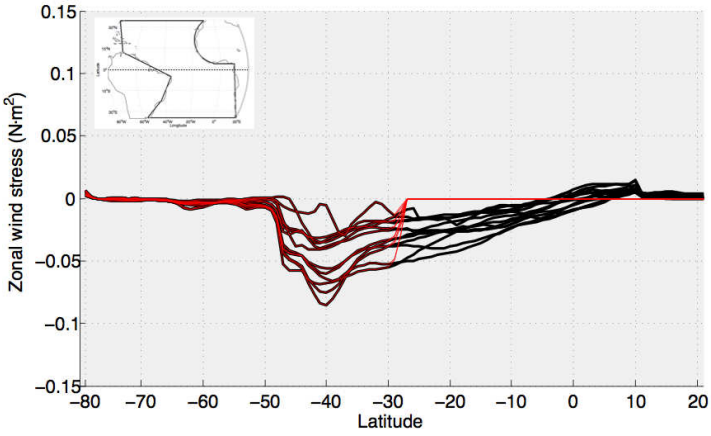

Figure 4.17: $\phi = 0°$ zonal section; black lines represent monthly means of the amplitude of the zonal wind stress forcing used for *Exp. A*; overlapped red lines represent the same signals zonally confined at 35 °W, used for *Exp. C*

4.4.1 Locally and remotely forced coastal upwelling

Polo et al. (2008) stressed that the upwelling (May to October) and downwelling (November to April) season at the eastern equator, coincide with the strengthening and weakening of the Trade Winds in the western

side at the equator. During the year 2001 (here analyzed), ECMWF wind stress data show that the zonal wind stress along the equator intensifies during the boreal summer both in the western and eastern side of the Atlantic basin; see Fig. (2.5) in section (2.1.1). Such seasonal increase implies a factor 4.5 in the west and a factor of 2 in the east side of the basin, where, moreover, the zonal wind stress is favorably oriented, to promote coastal upwelling, along the northern boundary of the Guinea Gulf.

In order to analyze, through the model response, the local effect of the wind in that region, we confine the wind stress over a side of the domain, as similarly done in the previous section and in a number of process-oriented model studies (Busalacchi and Picaut, 1983; Pierini, 2003). In this section, the wind stress forcing has been zonally confined at the longitude of 35 °W (Fig. 4.17) and, therefore, smoothly set to zero (*Exp. C*). Comparison with the model response from *Exp. A*, will highlight the temporal and spatial scale of coastal upwelling forced by local and non-local winds.

For the experiment *Exp. C* the wind forcing is prescribed as shown in Fig. (4.17), in which zonal sections of the wind stress taken along the equator are reported; the black lines represent monthly means of the wind stress and the red overlapped lines the same averages, zonally confined at 35 °W.

The Hovmöller diagrams of figures (4.18), (4.19) and (4.20) display the SSH evolution during the year along the entire Atlantic border of the african continent, between 35 °N and 35 °S. While figures (4.18) and (4.19) represent the response of the model experiments *Exp. A* and *Exp. C*, respectively, figure (4.20) shows the difference between such experiments, i.e., the oceanic response to local wind forcing. In figure (4.18), the northward and southward positive gradient of the SSH all year round is the most prominent feature. Such intense coastal divergence north of the tropics (more precisely north of about 25 °of latitude) is related to the prevailing winds in that area, indeed, the Trade Winds are meridionally oriented and flow parallel to the coast at those latitudes (see Fig. 4.2 for the meridional wind stress spatial distribution). Moreover, during the year, the intertropical latitudes (± 23 °) show a weaker divergence, which yields intraseasonal variability. In the same figure one can observe downwelling alternates to upwelling events, within a narrow latitudinal band including the Equator (5 °S - 5 °N); in turn, such signals propagate poleward, as evident from isoline inclination.

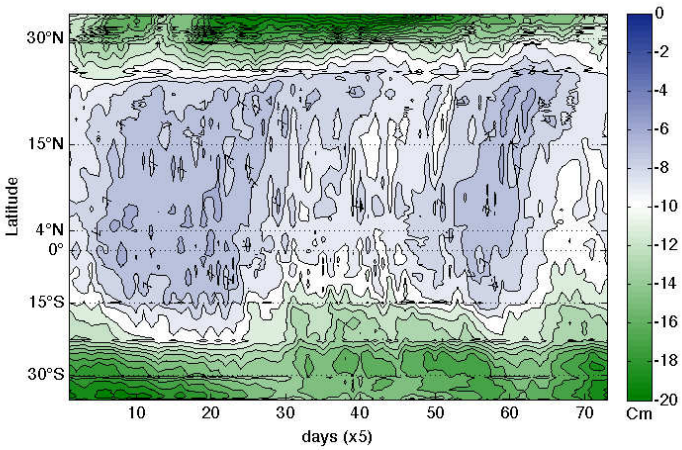

Figure 4.18: SSH (amplitude: cm). Hovmöeller diagrams of the model response (*Exp. A*) along the entire western african border (40 Km off the coast).

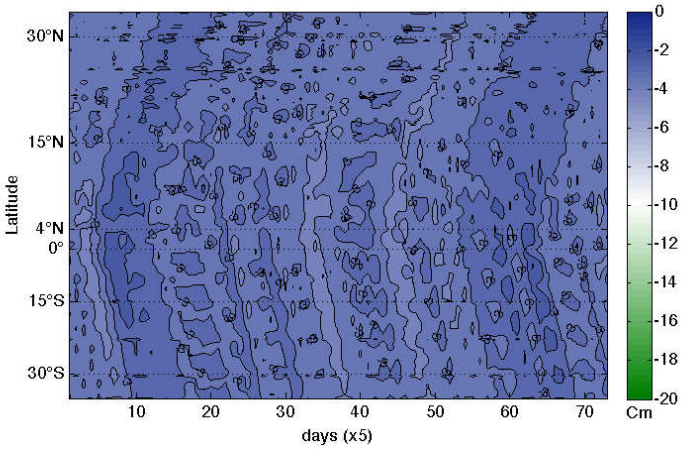

Figure 4.19: SSH (amplitude: cm). Hovmöeller diagrams of the model response (*Exp. C*) along the entire western african border (40 Km off the coast).

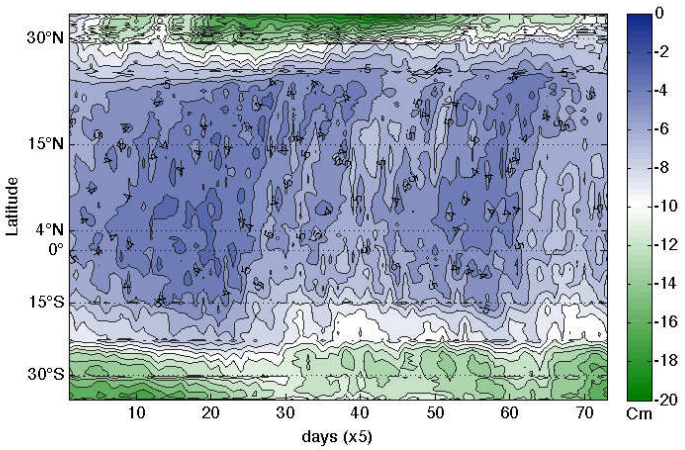

Figure 4.20: SSH (amplitude: cm). Hovmöeller diagrams representing the difference (*Exp. A-Exp. C*), i.e. the effect of the local wind forcing.

With more detail, a first downwelling season is found in a period starting from around the second half of January (25-125 days); at the end of April downwelling is replaced by upwelling for about four months, up to the end of August (265 days). During September and October a new short downwelling event occurs and then, upwelling dominates up the end of the year. In figure (4.19) poleward propagating Kelvin waves are generated by purely remote forcing, their speed can be estimated, from the isoline inclination, in $155.6\,km/day$. Therefore, a strong waves activity is clearly evident up to high latitudes and it occurs during time ranges corresponding to January-March, May-August and September-November. The generation of each signal yields a 20-40 days periodicity, which includes the maximum spectral peak found by Han et al. (2008) for the SSH Anomaly east of 10°W, during 2002-2003.

By means of our experiments, the alongshore winds effect may be evaluated through figure (4.20). If one compares such response (obtained from the difference between *Exp. A* and *Exp. C*) with the response of the reference experiment (*Exp. A*), it appears that local winds induce, within the same period, weaker coastal divergences (convergences) than in *Exp. A*. Moreover, January-May period coincides with the January-May 2002 period found by Han et al. (2008). These statements suggest that strong upwellings (downwellings), in the Guinea Gulf region, occur when local and remote forcing yield the same phase; in this case study, a factor of 1.75 establishes the difference between their effects.

4.5 Discussion

In this chapter was presented an analysis of the wind-driven tropical Atlantic variability by means of a process-oriented model approach. A purely dynamic reduced-gravity primitive equation ocean model was implemented in a domain with realistic coastline configuration of the Atlantic Ocean. The wind stress forcing was provided by one year (2001) of fine resolution data, obtained from ERA-40 Re-Analysis (ECMWF).

The model response yields annual beta-refracted baroclinic Rossby waves, radiating from the eastern boundary. Altimeter data from AVISO database and similar model studies, with application on the Atlantic and Pacific Ocean (Han et al., 2008; Polo et al., 2008), describe a qualitative agreement that confirm our results. The role of the beta-refraction in shaping such basin-wide Rossby waves has been investigated and theoretical validation of empirical analysis on the different westward penetration of such waves has been carried out.

Interesting information, obtained from ad hoc sensitivity experiments, concern the mechanism through which the seasonal variability is generated at the eastern tropical Atlantic boundary. A teleconnection mechanism seems connect the oceanic variability at the western and eastern side of the basin, triggered by the seasonal changing of the wind stress intensity. The same mechanism is decisive in shaping the eastern boundary variability, and it was found to be the remote mechanism for the generation of the above mentioned westward propagating mid-latitude Rossby waves, as showed by Pierini (2003) in a similar process oriented model study devoted to describing the tropical Pacific seasonal variability.

Finally, coastal Kelvin waves activity and the role of their poleward propagations in generating seasonal upwellings (downwellings), within the Guinea Gulf region, has been investigated. Eastward propagating Equatorial Kelvin waves seem transfer potential energy at the eastern oceanic boundary in form of the above mentioned coastal waves that, in turn, together with alongshore local wind forcing, represent a generating component of coastal upwelling (downelling), due to remote origin. The remote forcing signal, obtained through the model response, displays similar periodicity like those found by Polo et al. (2008), through OGCM and SSH fields analysis.

A technical statement concerning the model approach, deserve to be mentioned in this section. Although, the reduce gravity shallow water model introduces simplification of the real physical processes involved in the oceanic variability, it proves that a significant part of the seasonal dy-

namic height signal can be analyzed in the context of purely wind-driven nonlinear processes. Nevertheless essential features must be included in the implementation in order to obtain a realistic oceanic response, at least qualitatively comparable with observations. Indeed, the large-scale features of the basin geometry, as well as the zonal width of the basin at each latitude (Pierini, 2008), must be taken into account under the model implementation. Moreover, the fine temporal and spatial resolution of the wind fields allow us to resolve the oceanic mesoscale variability.

The last comments concerns the possibility to go into more detail of the wind-driven tropical Atlantic processes and, in this context, a specific path has already been drawn. The implementation of a two-layer model configuration (from which the reduced-gravity model derive) appears essential to investigate the barotropic response of the ocean and its interaction with the first baroclinic mode (the only mode that a two-layer model can describe). Moreover, such model would allow us (differently from the reduced-gravity version) to include topographic effects. The bottom topography would increase the degree of realism of the model response, especially in the central oceanic region, where the Atlantic mid-oceanic ridge rises up to one thousand meters from the mean depth. Thus, the interesting effect of the bottom topography in modifying the shape and phase of mid-latitude westward propagating Rossby wave could be evaluated.

5

Intrinsic low-frequency variability in the Gulf Stream region

5.1 Introduction

In this chapter the results of a process study on the role of nonlinear inertial effects in generating low-frequency variability of the Gulf Stream (GS) and GS Extension (GSE) jet will be presented. Like the Kuroshio, located in the North Pacific Ocean, the GS is the major western boundary current (WBC) of the North Atlantic basin. These currents transport huge volumes of hot and salty water poleward, so that their dynamics profoundly affects the global climate system.

Both the GS and Kuroshio display intense low frequency variability of different character on the interannual and interdecadal time scales. Experimental evidence indicates that the Kuroshio displays bimodal meandering behavior off the southern coast of Japan, with transitions occurring between a small and a large meandering mode. Each mode can persist over periods ranging from few years to a decade (Qiu, 2002).

For the GS region, evidence was provided by Bane and Dewar (1988) of a bimodal behavior of the current seaward deflection off South Carolina. Although less pronounced than in the Kuroshio, transitions between both states occur on an intermonthly time scale. Other studies of the GS path using in situ measurement and advanced very high resolution radiometer (AVHRR) data show indication of a bimodal character of the stream in the area just after separation, at 71 °W, where a shift of

0.5 °in latitude occurs (Auer, 1987).

The two currents, hence, display a bimodal behavior, with the Kuroshio undergoing more energetic changes. Modeling results of the wind-driven circulation in idealized rectangular basins (Dijkstra and Katsman, 1997; S.Jiang et al., 1995) and in more realistic configurations with continental geometry and realistic wind stress (Dijkstra and Molemaker, 1999) confirm that multiple equilibria are present in both the North Pacific and Atlantic Oceans. A high-resolution ocean general circulation model (OGCM) and a barotropic shallow water model have also showed evidence that multiple states are dynamically possible in the GS and in the Kuroshio jets (Schmeits and Dijkstra, 2001). Although the Atlantic and Pacific oceans have different dimensions, the mean wind stress fields have very similar spatial patterns; yet the GSE and KE variability are quite different. Hence, the basin geometry (both in terms of its zonal width and coastline structure) must play a role in shaping the intrinsic oceanic dynamics (e.g. Pierini 2008).

A model study of the Kuroshio Extension (KE) system, whose solution yields a mean meandering path and a decadal variability of the jet in significant agreement with observations is proposed by Pierini (2006). The dynamics is governed by a reduced-gravity nonlinear shallow-water model implemented in an idealized North Pacific Ocean, with a schematic western coastline. The wind stress has a double-gyre structure including aspects of the real atmospheric forcing. In such a study the climatological wind produces an intrinsic decadal self-sustained chaotic oscillation of the KE, that is often considered as the response to a time-dependent atmospheric forcing (Qiu, 2002; Qiu and Chen, 2005). Subsequent analyses based also on nonlinear dynamical system theory (Pierini and Dijkstra, 2009; Pierini et al., 2009) have also supported the hypothesis that the KE bimodality is mainly controlled by intrinsic effects.

In this context it is clear that nonlinear western boundary jets may develop meanders as a consequence of inertial effects only. Therefore, in this Thesis the same reduced-gravity nonlinear model used in Pierini (2006) was implemented in the North Atlantic basin, with the aim of investigating the origin of the GS low-frequency variability, in order to verify whether intrinsic mechanism actually play a role in the low frequency variability. The model implementation was enriched by a schematic coastline of the Atlantic basin with the aim of preserving the essential geometric features of the coast and the zonal width of the integration domain (Pierini (2008) showed the crucial role played by the basin geometry in

shaping the variability of the Kuroshio). Moreover, a climatological wind stress forcing was derived by 41 years of wind velocity obtained from ECMWF monthly fields. When compared with the usual double-gyre wind forcing, the present climatology provides an essential element of realism that should not be neglected if pseudo-realistic coastlines are taken into account.

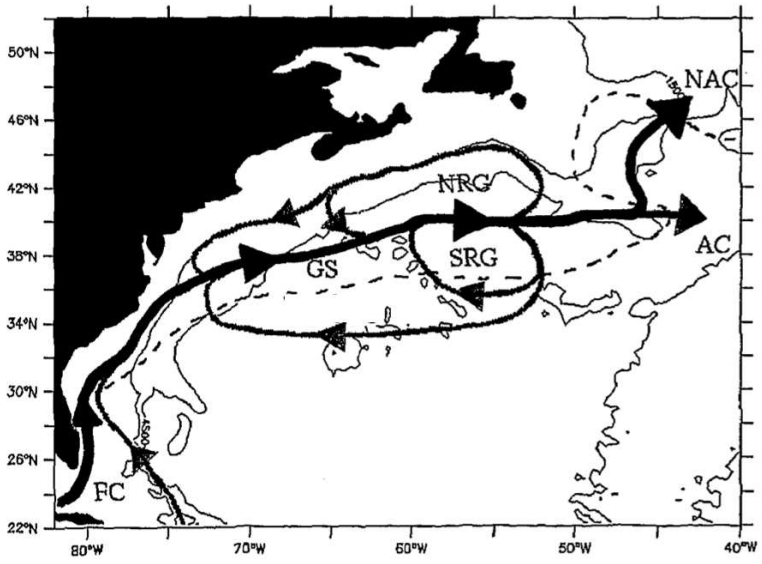

Figure 5.1: Sketch of the GS region from (Deng et al,1996). The FC and GS branch into the North Atlantic Current and Azores Current. Northern and Southern recirculation gyres (NRG and SRG, respectively) are also depicted

The chapter is organized as follows. In Section 5.2 a short review of the main physical mechanisms involved in the generation of WBCs is presented, moreover, the prominent features of the GS and Kuroshio variability are considered in the relative subsections. The model and technical aspects of the implementation are discussed in Section 5.3, along with an insight of the wind stress forcing climatology and the domain of integration. In Section 5.4 the intrinsically generated GS mean jet is discussed and compared with satellite derived climatological observations, in order to validate the model results. A description of the simulated low-frequency variability of the GS system is addressed in Section 5.5, and a preliminary analysis of the obtained variability. The latter is discussed

in Section 5.6 in terms of nonlinear dynamical systems theory. Finally, conclusions are presented in Section 5.6, where future perspectives are also outlined.

5.2 Western Boundary Currents in the Atlantic and Pacific Oceans

Along the western sides of these oceans, WBCs flow poleward as intense and narrow currents. The strongest currents are located in the northern hemisphere; the Kuroshio in the North Pacific and the Gulf Stream in the North Atlantic. By contrast, in the southern Hemisphere, the Brazil Current and the East Australian Current are weaker WBCs . This because the South Atlantic and South Pacific are open to the Southern Ocean and, furthermore, the currents experience a different coastal constrain. The eastern boundaries are instead characterized by wide, equatorward currents with slow surface velocities an order of magnitude weaker than WBCs (Colling and CourseTeam, 2002).

The oceanography of the WBCs was discussed in section 2.2.2; the present section will be devoted to define the main physical mechanisms involved in the generation of WBCs; moreover, in two subsections the description of the prominent features of the GS and Kuroshio systems variability will be considered. This is a brief overview (the reader can refer to WOCE 2001 for more details) which, however, focuses on a number of relevant aspects that will be discussed in the context of this research work.

The Sverdrup balance (i.e. the response of the ocean interior to an applied wind stress curl forcing) does not allow for a steady solution at the western boundary; indeed, nonlinearity and dissipation are not taken into account in such a balance, thus it cannot explain the existence of intense WBCs. In 1948 Stommel considered the effect of a symmetrical anticyclonic wind field on a rectangular rotating basin; in his calculations he included a linear variation of the Coriolis parameter with latitude (the beta-plane) and bottom friction, so that westward intensification arises when the wind stress and frictional forces balance out.

In terms of of vorticity (or conservation of angular momentum), this experiment shows how the anticyclonic wind field and the variation of the Coriolis parameter with latitude (towards regions of larger planetary vorticity) supply negative relative vorticity (clockwise rotation) into the ocean, leading to a continuous gain of speed at the western boundary,

which is, hence, balanced by frictional forces. By contrast, in the oceanic interior the negative relative vorticity supplied by the wind, is balanced by the positive vorticity supplied by the change in latitude towards regions of smaller planetary vorticity. That model was extended by Munk (1950) by considering a horizontal eddy viscosity.

The coastline orientation and the ocean bottom topography may also have an important influence on the vorticity budget. Indeed, the GS and the Kuroshio cross the continental rise leaving the shallow continental shelf (about 1000 meters) towards the open sea, where the bottom topography drops sharply to 5000 meters within a few hundred kilometers. As far as the coastal orientation is concerned, in terms of potential vorticity conservation, $f + \zeta/D$ (where f is the planetary vorticity, ζ the relative vorticity and D the depth of the flow), the speed and direction of the stream is the result of a balance between the varying bottom topography and the orientation of the coastline that may induce a slower or faster changing in planetary vorticity.

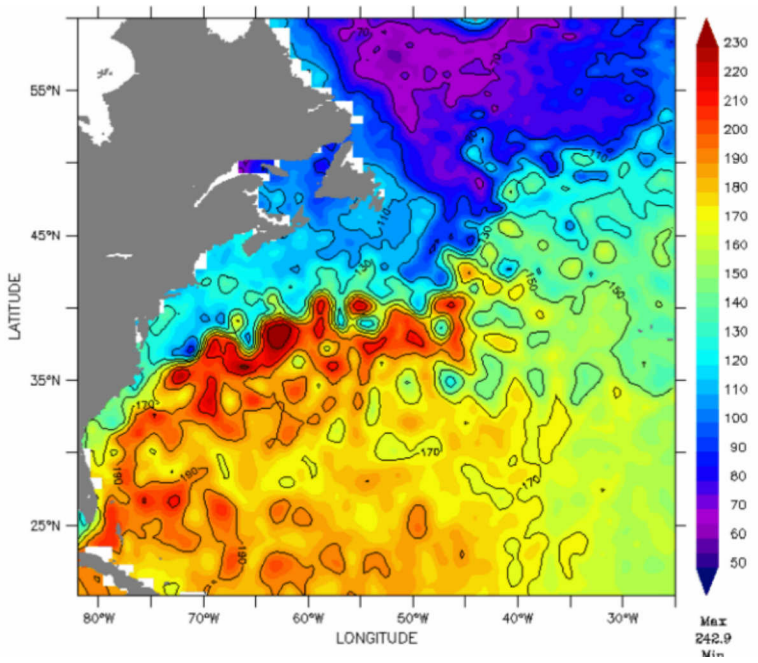

Figure 5.2: Snapshot of the October 5, 2005 absolute dynamic topography (distributed by Aviso/Cnes) over the GS and GSE region, (amplitude: cm), http://www.aviso.oceanobs.com/.

5.2.1 The Gulf Stream

Since the seventeenth century the Gulf Stream has been intensively explored, and nowadays it is a continuously surveyed region. A sketch of the near-surface circulation in the GS region is given in Fig. 5.1 (by Dengg et al. 1996). Although in situ investigations and satellite observations supply a well defined time-mean path of the GS (Auer, 1987; Kelly et al., 2010; Lee and Cornillon, 1995), several aspects of the variability and its origin are still controversial; this subsection will summarize the current knowledge on the variability of the GS.

As previously stated in section (2.2.2), the GS can be arbitrarily subdivided into the Loop Current located in the Gulf of Mexico, the Florida Current, the Gulf Stream proper, the Gulf Stream Extension and the continuation of the jet into the North Atlantic and Azores Currents. Since the stream flows into the northwest Atlantic Ocean from the Florida Straits, it follows the Florida coasts as a stable parallel flow (Florida Current). A snapshot of the absolute dynamic topography of the GS region is plotted in Fig. 5.2. Following the southeast United States coastline the GS yields a seaward deflection off South Carolina, as revealed by satellite observations (Bane and Dewar, 1988) and OGCM simulations. Bane and Dewar (1988) suggested that such seaward deflection has a bimodal character, with transitions occurring on intermonthly time scale; however, Auer (1987) showed by means of yearly averages of the GS edge (the cold wall of the GS due to the large temperature gradient across it) a small interannual variability in the same region (see his figure 4).

The GS continues along its northward path as far North as Cape Hatteras, where it leaves the american continent without any pronounced change in curvature. The separation point (defined by Dengg et al. 1996 as the cross-over point with the shelf edge) is fairly stable if compared with the variability of the downstream region; nevertheless, it also displays little temporal variations that result in meridional excursions of $\pm 50\,Km$ (Auer, 1987). Once the GS leaves Cape Hatteras, it gives rise to the GSE oriented north-eastward along 38-40 °N accompanied by a strong meandering with a variability from the monthly to the interannual scales and typical spatial scale of 500 Km. Moreover, large cold-core rings and warm-core rings are formed as a final stage of meander development, where the meander is detached from the main current (Dijkstra, 2005). By means of AVHRR-derived infrared images subannual (9 months) and near-annual (12-months) periodicities have been identified as the dominant variability of the GSE (see Lee and Cornillon 1995). Although large

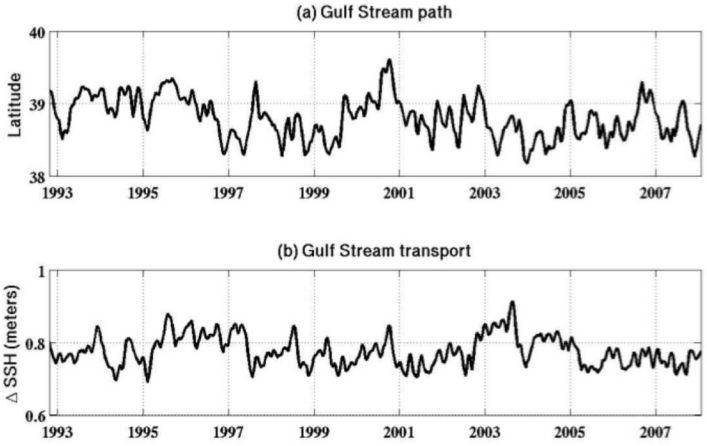

Figure 5.3: Indices in the Gulf Stream region. Zonally averaged index of GS path latitude (top panel) and GS surface transport for 72-52 °W (bottom panel), from Kelly et al. (2010).

uncertainties on the driving physical mechanisms persist, the authors correlate such periodicities to the wind forcing and the internal ocean dynamics, respectively.

Westward of 70 °W the GSE variability may be profoundly affected by regional ocean dynamics and thermodynamic processes. Dengg et al. (1996) presented a review on the mechanisms of the GS separation at Cape Hatteras and the factors controlling the subsequent jet path, that are still under debate The most reliable theories discussed by Dengg include: directly wind-forced separation, separation by detachment, vorticity crisis, inertial overshooting, topographic effects and JEBAR (Joint Effect of Baroclinicity And Relief). The author suggests that the GS separation is the result of a combined effect of nonlinearity, coastline inclination, bottom topography and stratification; moreover, after the separation the mean position of the stream axis is probably determined by dynamics of the Northern Gyre. Recently Pierini et al. (2010) have presented laboratory simulations that strongly support the inertial overshooting mechanism. Additional influences are also due to the GS interaction with the Deep Western Boundary Current (DWBC). As reported by Chassignet and Marshall (2008) the DWBC may influence GS separation through two distinct mechanisms: southward "advection" of the separation point and generation of an adverse pressure gradient within the GS, through the vortex stretching induced by the descent of the

DWBC. In this context, for instance, Spall (1996a) finds low frequency oscillations and he attributes them to the entrainment of the upper core of the DWBC into the separating GS.

Recently Kelly et al. (2010) provided indices that describe temporal variations in strength and latitude of the current axis of the Gulf Stream and Kuroshio Extension. Their results, here reported in figure 5.3, display the interannual variability of the zonally averaged (52 °-72 °W) mean path and transport of the GS. Such figure is directly comparable with Fig. 5.4 in which the mean path position and transport of the KE display its prominent decadal periodicity.

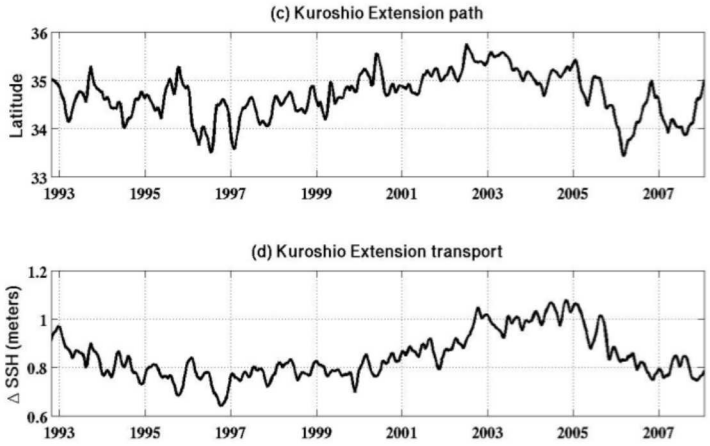

Figure 5.4: Indices in the Kuroshio Extension region. Zonally averaged index of KE path latitude (top panel) and KE surface transport for 140Ð160 °E (bottom panel), from Kelly et al. (2010).

5.2.2 The Kuroshio

The Kuroshio is the intense WBC of the North Pacific Ocean. After the separation from the coast of Japan, near 140 °E and 35 °N (Qiu, 2002), the separated jet called KE. A prominent feature upstream of the KE is the presence of two quasi-stationary meanders with their ridges located at 144 °E and 150 °E , respectively. Fig. 5.5 shows a map of the mean sea surface topography adapted from Qiu (2002), in which this feature is evidenced. Moreover, near 159 °E, the KE often bifurcates, and a secondary branch extends north-eastward to 40 °N, where it joins the Subartic Current (SC). Eastward of 170 °E the mean path of the stream broadens and the distinction between the KE and the SC is no longer

clear (Fig. 5.5).

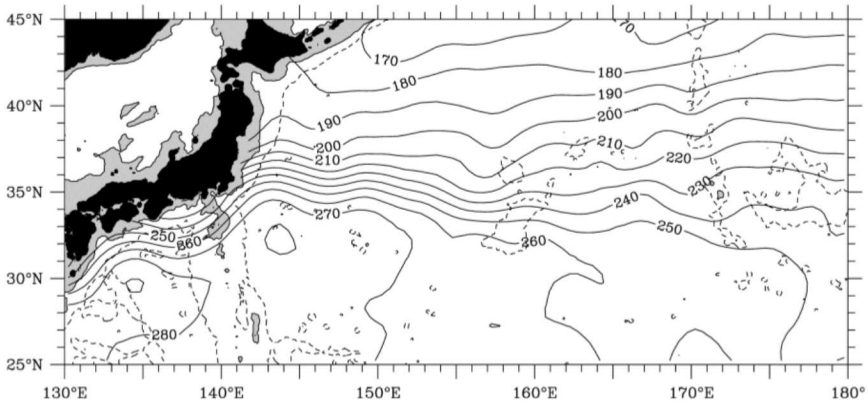

Figure 5.5: Satellite and in situ climatology of the sea surface topography (in meters) relative to 2000 dbar, adapted from Qiu (2002).

In the KE region the highest level of eddy kinetic energy in the Pacific Ocean is reached (Wyrtki et al., 1976): many investigators have thus examined the spatial and temporal changes of the KE. Significant progresses have been achieved in the description of the propagation of mesoscale eddies and seasonal changes of the KE (see Qiu 2002 for references). However, in comparison with the knowledge of mesoscale variability, the understanding of the large-scale, low-frequency variability of the KE is more limited (Qiu, 2002).

In Qiu and Chen (2005) twelve years of SSH data have been used to investigate low-frequency changes in the KE jet. He found a dominant signal with a decadal time scale that is characterized by a succession of elongated and contracted states. The path of the KE exhibits, thus, a bimodal behavior, and the transition from an elongated a contracted state occurs within a couple of months, as showed by altimetric measurements (Qiu and Chen, 2005). The two contrasting modes may be verified by inspecting two observed SSH maps in Fig. 5.6, adapted from Qiu (2002); the elongated state (top panel) yields small meandering, has a larger eastward surface transport, a greater zonal penetration and a more northerly zonal mean-path. By contrast in its contracted state (bottom panel) the KE has a smaller eastward surface transport, a more southerly mean-path and yields a large meandering.

Interannual-to-decadal changes in the basin-wide wind stress curl field (Qiu and Chen, 2005) and internal nonlinear dynamics (McCalpin and Haidvogel, 1996; Pierini, 2006) are known to be possible causes of the

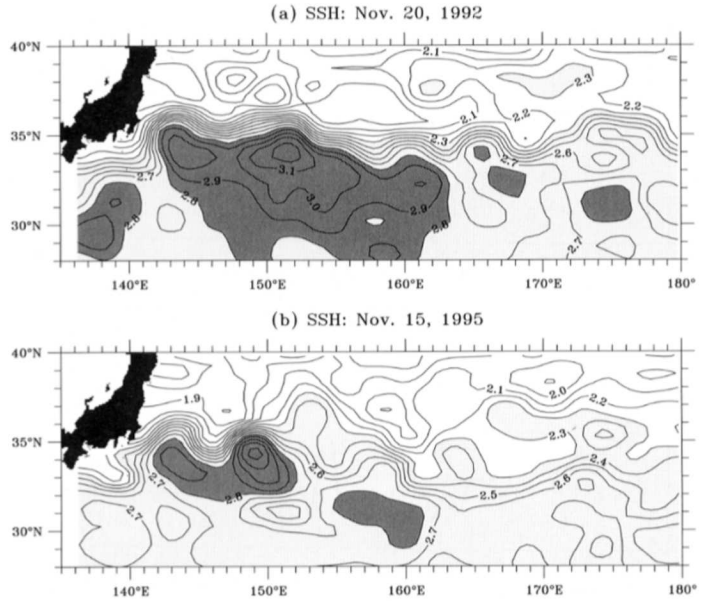

Figure 5.6: SSH fields on 20 November 1992 (top panel) and 15 November 1995 (bottom panel) representing an elongated and contracted mode of the KE, respectively, adapted from Qiu (2002).

above mentioned bimodal behavior of the KE system. By means of a reduced-gravity primitive equation ocean model forced by a steady double-gyre wind field, Pierini (2006, ,2009a) analyzed the role of nonlinear inertial effects in both the mean structure of the KE and its variability. His results showed that nonlinear inertial effects alone may play a fundamental role in determining the observed structure of the mean jet and its bimodal oscillation.

5.3 Implementation of the mathematical model

The model used in this analysis of the GS intrinsic low-frequency variability is the same one that, in Chapter 4, was applied to the tropical Atlantic Ocean to analyze the wind-driven seasonal variability. It is a reduced-gravity, shallow-water, nonlinear primitive equation ocean model (see Chapter 3 for governing equations, formulated as in (3.24) and (3.25, and their derivation), here implemented on the northern Atlantic basin.

In recent model studies on the analysis of the low-frequency variability of the Kuroshio Extension the same reduced-gravity model was successfully applied to the Pacific counterpart (Pierini, 2006).

This model, consisting of a thin upper layer superimposed on a much deeper motionless lower layer, was correctly adopted in the context of the tropical basin. Although in the context of the GS the applicability of the same model is less appropriate (e.g., the barotropic component is not negligible), in view of a process-oriented model study its use is still justified. Obviously a two-layer model would be the ideal tool in the same context but it requires much longer numerical simulations due to the introduction of the external mode in the system and the necessity to comply with the CFL condition: its implementation with a parallel version of the code is underway. Table (5.2) lists the parameter values have been chosen for the implementation of the model. The depth of the active layer is chosen to be $H = 1000\,m$, so that the entire vertical shear of the stream is included. The spatial grid steps, 20 Km, have been chosen in both the latitudinal Δy and longitudinal Δx directions; indeed, it has been recognized (Chassignet and Marshall, 2008) that eddy-permitting models are able to reproduce the main features of the GS; the temporal step is $\Delta t = 20\ min$.

The reduced-gravity value was derived from mean densities obtained, for each layer, from vertical sections of the WOCE-Atlas (http://sam.ucsd.edu/). No-slip boundary conditions are imposed along the closed boundaries and the time integration is carried out starting from vanishing initial conditions for fifty years of integration time. The interfacial friction coefficient $\gamma = 5 \cdot 10^{-4}$ is the same used by Pierini (2006) in his study on the KE. Different values of the lateral eddy viscosity A_H will be considered in sensitivity experiments, as we will see below, but the basic value is $A_H = 100 m^2\, s^{-1}$. The free surface displacement η is computed from the thermocline displacement $\tilde{\eta}$ through $\eta = \tilde{\eta}\Delta\rho/\rho$ where ρ is a mean density and $\Delta\rho$ is the density difference between the two layers.

Table 5.1: Imput parameter values

Parameter	value
Depth	$H = 1000\ m$
Grid size	$\Delta x = \Delta y = 20\ km$
Time step	$\Delta t = 20\ min$
reduced-gravity	$g' = 0.021\ m \cdot s^{-2}$
Boundary condition	Free-slip
Interfacial friction	$\gamma = 5 \cdot 10^{-4}$
Eddy viscosity coefficient	$A_H = 100\ m^2 \cdot s^{-1}$

Domain of integration

The domain of integration, shown in Fig. 5.7, includes schematic coastlines which correctly represent the large-scale shape of the continental boundaries between the latitudes 60°N and 10°S (the inclusion of the southern Hemisphere allows us to take into account aspects of the equatorial ocean dynamics). This choice is justitified by the analysis of Pierini (2008) who showed that a correct representation of the ocean boundaries is essential in shaping both the mean flow and the low-frequency variability of the KE. Moreover, the present approach is in line with that used here to study the wind-driven seasonal variability of the tropical Atlantic Ocean (see Chapter 4) explained in detail in section (4.2.1).

The zonal width extends between the longitudes 75 °W and 15°E, spanning the entire north Atlantic basin. Several segments, delimited by as many coastal points of specific geographical coordinates, connect eleven points along the western boundary: $A = (10°S, 34°W)$, $B = (6°S, 35°W)$, $C = (9°N, 60°W)$, $D = (16°N, 61°W)$, $E = (22°N, 79°W)$, $F = (31°N, 81°W)$, $G = (35°N, 75°W)$, $H = (40°N, 73°W)$ and $I = (46°N, 52°W)$, $L = (54°N, 56°W)$ and $M = (60°N, 63°W)$. The eastern boundary of the Atlantic basin is delimited by a border that excludes the adjacent seas from the integration domain, and the boreal Africa is represented by a circle (see the green line overlapped to real coastline and wind stress curl in Fig. 5.7).

Wind forcing

In several analogous process-oriented model studies, analytical wind stress fields derived from observations have been adopted (Hogg et al., 2005; McCalpin and Haidvogel, 1996; Pierini, 2006; Simonnet et al., 2003; S.Jiang et al., 1995). In a study of the north Atlantic wind-driven ocean circulation Dijkstra and Molemaker (1999) showed that more realistic flows may be obtained if a realistic wind stress forcing (in that case obtained from the Hellerman-Rosenstein data set) is used in a reduced-gravity shallow water model. Moreover, other studies (Chassignet and Marshall, 2008; Dengg et al., 1996) showed that the geographical distribution of vanishing wind stress curl may affect the representation of a number of GS and GSE features.

As a consequence, in this process study zonal and meridional components of the wind velocity have been retrieved from the ERA-40 Re-Analysis Project data set of the ECMWF. In detail, forty-one years (1961-2001) of monthly mean fields, which include the entire domain of integra-

tion, have been used to calculate an individual climatological field with spatial resolution of four degrees in both horizontal directions. Estimates of the zonal (τ_x) and meridional (τ_y) components of the surface wind stress have been computed here from the wind velocity through the bulk formulation as shown in section (4.2.2). The obtained wind stress climatology (Fig. 5.7) is used as the time-independent forcing for our model.

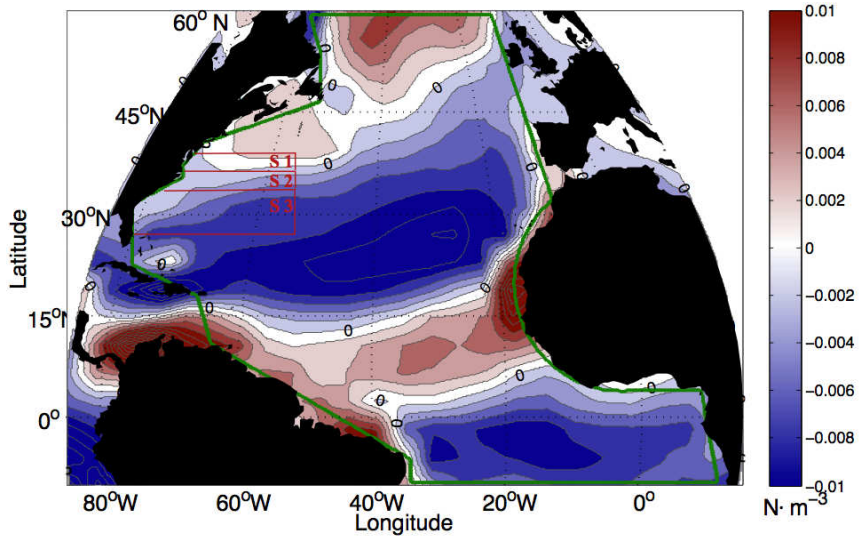

Figure 5.7: Domain of integration (green line) overlapped to real coasts (black patch) and 41 years (1961-2001) climatology of ECMWF derived wind velocity, here represented as wind stress curl.

5.4 The Gulf Stream Extension jet

An overview of the GS system was given in section 5.2.1. In this section an analysis of the model solution and relative comparison with observations will be presented; several simulated features of the GS System will be identified and compared with observations.

After spinup (15 years; see time series in Fig. 5.11), a time average

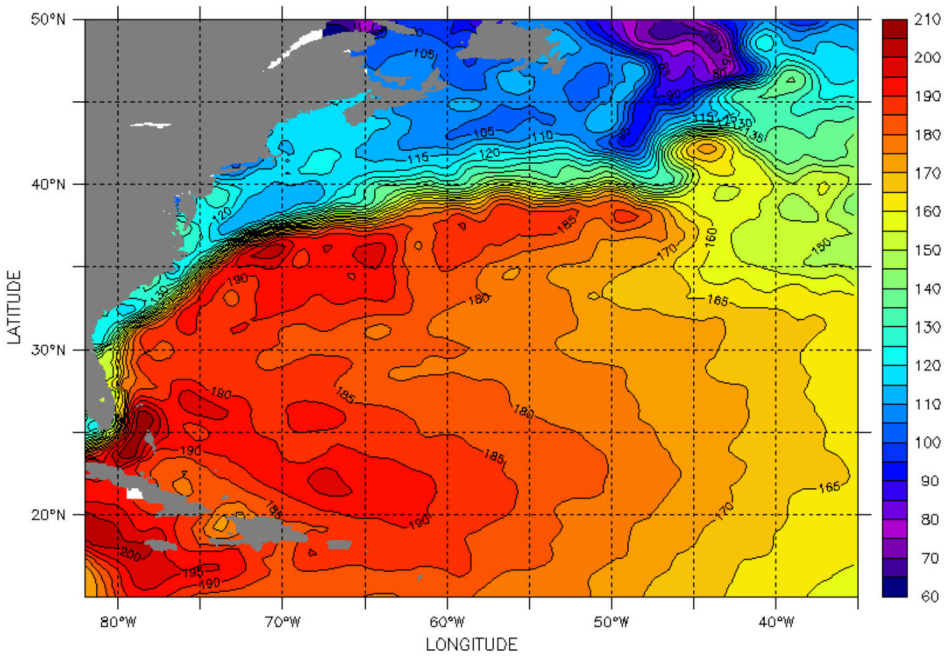

Figure 5.8: 7-years (08 May 2002 - 22 July 2009) climatology of absolute dynamic topography (distributed by Aviso/Cnes) over the GS and GSE region; (amplitude: cm).

of the SSH over the period $t = 24 - 50$ years, where t is the time of integration, was computed. The resulting mean SSH field, shown in Fig. 5.9, can be compared with the $7 - year$ climatology (Fig. 5.8) of the absolute dynamic topography derived from satellite altimeter products (distributed by Aviso/Cnes). The large-scale model response to the climatological wind stress forcing shares several features with observations, especially far from the western boundary, where the Sverdrup balance determines the flow in the oceanic interior. The numerical solution yields a weak recirculation cell (its southern edge include the Antilles Current) which extends along the northern boundary of the Caribbean archipelago up to the Florida coast.

In the simulated SSH a weak southern recirculation cell is found, while North of Cape Hatteras a wide divergence area, due to the atmospheric cyclonic circulation at high latitudes, characterizes the response of the model (Fig. 5.9). As for the position of the GSE, in the model response the jet is shifted southward by about 3 °of latitude (see section 5.4.3) when compared with the real jet (Fig. 5.8). To better understand the simulated features of the western intensification we divide the GS system

into three geographical regions, as explained in the following section.

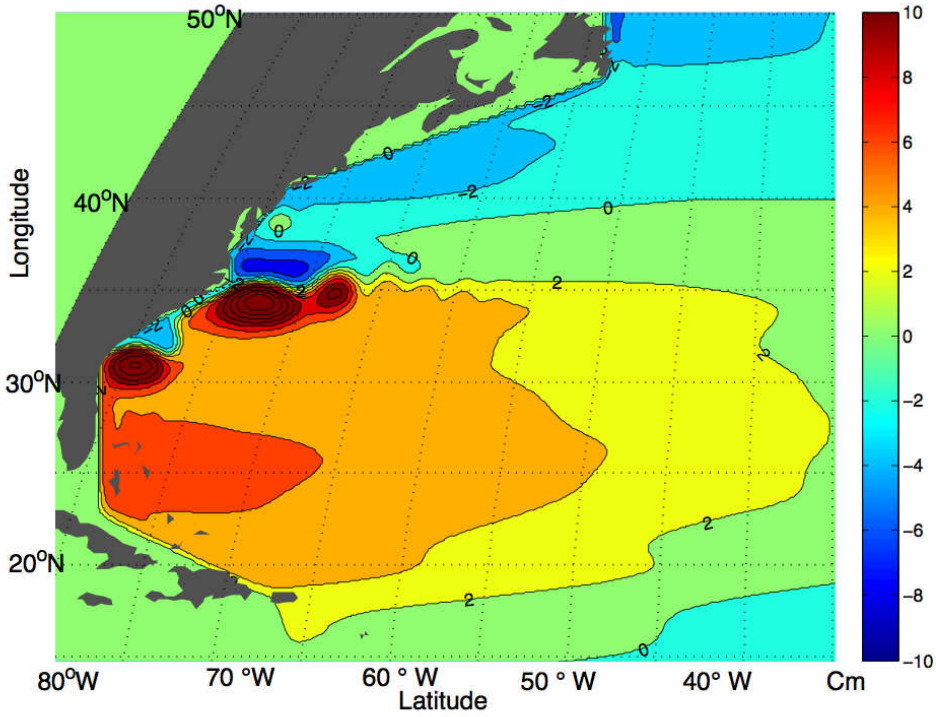

Figure 5.9: 26-yr mean of the simulated SSH fields over the GS and GSE region, directly comparable with Fig. 5.8, (cm)

5.4.1 Florida Current

It is well known that the Florida Current (FC) flows almost parallel to the coastline. Its transport is the result of two main contributions: the Antilles Current and the Loop Current. The latter is found to be the most significant one, originating in the Gulf of Mexico and flowing into the GS through the Florida Straits. Recent estimates provided by Wilson and Johns (1997), suggest an influx of 17.5 Sv in this passage. The flow in that location is highly variable and may in part account for the considerable variability of the Florida Current, that is affected by both seasonal and interannual changes (Wilson and Johns, 1997). The present model solution (Fig. 5.9) does not include the Gulf of Mexico region, so that the simulated response does not take into account dynamical processes occurring there. This implies that the simulated FC, correctly

flows along the coastline, is more stable and weaker than the observed one.

Once the FC reaches the South Carolina coasts a seaward deflection of the mean flow is observed (Fig. 5.8). Bane and Dewar (1988) state that the presence of a topographic irregularity known as the Charleston Bump, off South Carolina (near 31 °N), may affect the path of the FC. They also note that such deflection has been shown to be show bimodal character, with the FC assuming either a weakly or strongly deflected state. A seaward deflection of the FC is also present in the simulation (Fig. 5.9) as the northern edge of a strong recirculation gyre centered at 31 °N and 79 °W (the latter being quite different from the real one). The deflection breaks the meridional orientation of the FC and, since the reduced-gravity model does not take into account topographic effects, this premature separation from the coast must be due to a combination of inertial effects and coastline orientation.

Premature separations have also been found in model studies on the role of the viscosity parameterization on the GS separation at Cape Hatteras (Chassignet and Garaffo, 2001) and in the output of the Parallel Ocean Climate Model (Schmeits and Dijkstra, 2001). There, the GS seems to separate twice, first too far south compared to reality and then too far north.

Adcroft and Marshall (1998) demonstrated that piecewise-constant coastlines exert a spurious form stress on model boundary currents depending on the implementation of lateral boundary conditions and can, in some cases, introduce premature western boundary current separation. Thus, although mutual interactions between the stream and the topographic irregularity should be take into account, an hypothesis that we want to put forward is that the Charleston Bump may be a consequence of a premature separation of the stream and not a cause of the seaward deflection.

5.4.2 Gulf Stream and upstream Gulf Stream Extension jet (77 °W - 67 °W)

At about 33 °N, beyond the seaward deflection, the stream rejoins the coastline and continues North to Cape Hatteras (recognized as GS), where it leaves the coast at about 35 °N, 74 °W (the separation point, see Lee and Cornillon 1995). A quantitative comparison between obser-

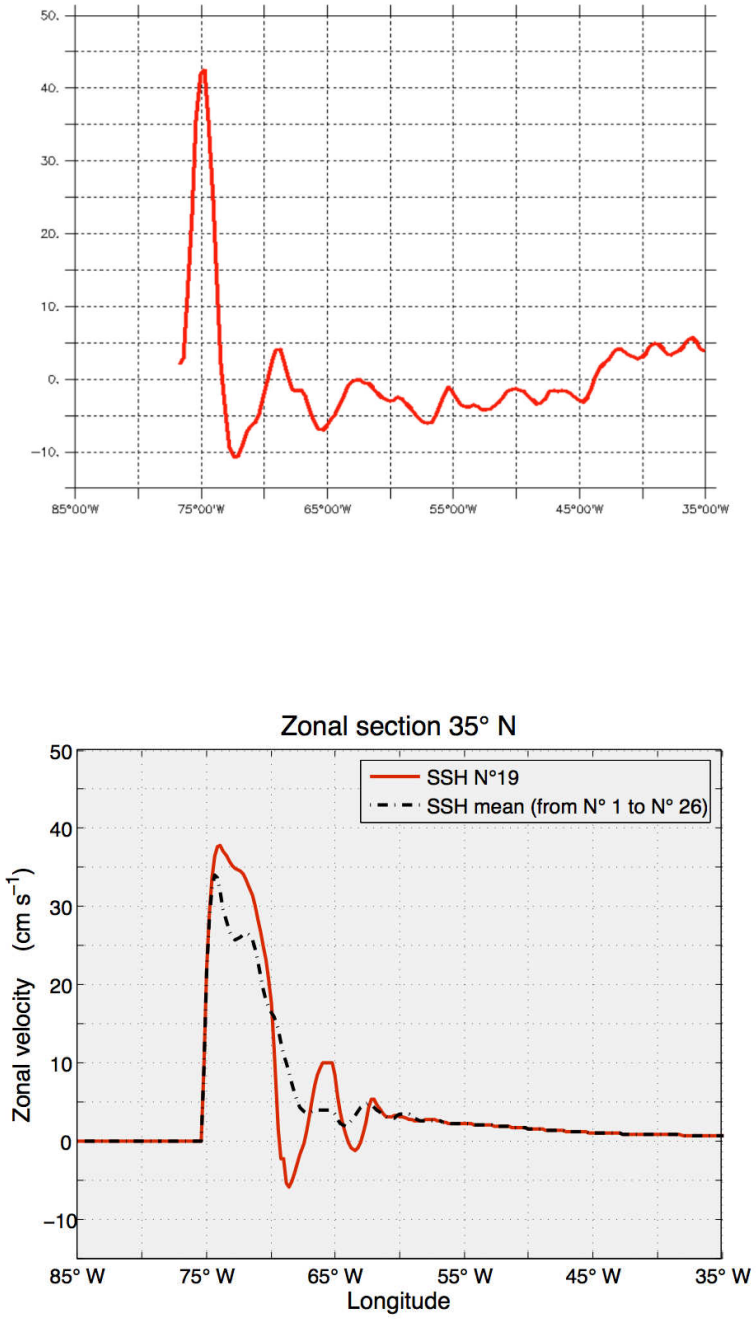

Figure 5.10: Top panel: 7-years (08 May 2002 - 22 July 2009) climatology of the absolute geostrophic velocity (distributed by Aviso/Cnes) along 35 °N; Bottom panel: 26-samples average (dotted black line) and one snapshot, at the integration year=19, (red line) of the simulated geostrophic velocity along 35 °N.

vations and model response can be performed through figure 5.13. In the bottom panel the red line indicates that the model simulates a strong zonal current, whose intensity is in good agreement with the observed absolute geostrophic zonal velocity (top panel).

Moreover, a comparison between Fig 5.8 (the observed climatology) and Fig 5.9 (the model response) shows that the model is able to correctly reproduce the separation location. Nevertheless, the observed GS does not display a pronounced change in curvature at the separation point as the model response does. In reality the upstream GSE jet deviates northeastward, but further north in latitude if compared with the model solution, displaying two weak meanders at 62 °W and 67 °W, respectively, and a quite strong recirculation cell centered at 36 °N and 72 °W. Beside this, the model response yields two meanders as well, with comparable zonal location but larger curvature. The location of the recirculation cell is also correctly reproduced by the model simulation.

5.4.3 Downstream Gulf Stream Extension jet (67 °W - 57 °W)

Downstream, eastward of 67 °W the GSE loses its inertial feature and starts broadening. Far from the constraint of the coastal boundaries the GSE rejoins gradually the interior circulation of the North Atlantic Ocean, accompanied by the formation of large-amplitude meanders (see section 5.5). In this region both observations and model response (averaged fields in Fig. 5.8 and Fig. 5.9) display such a large-amplitude meandering.

While the model response yields a zonally oriented mean-path along 35 °- 36 °N, the observations display a mean-path along 38 °- 40 °N. Nevertheless, the location of the 0-cm contour line, as obtained by the model, coincides fairly well with the observed 135 cm contour line.

5.5 Low-frequency changes in the Gulf Stream system

To explore the low-frequency changes in the GS System we start with Fig. 5.11 showing the model response to the wind forcing in terms of kinetic energy $E_K(t)$ integrated within sector $S1$, $S2$, *and* $S3$ (see figure 5.10). Sector $S1$ includes only partially the jet variability and displays low energy values; by contrast, sector $S2$ represents most of the variability of

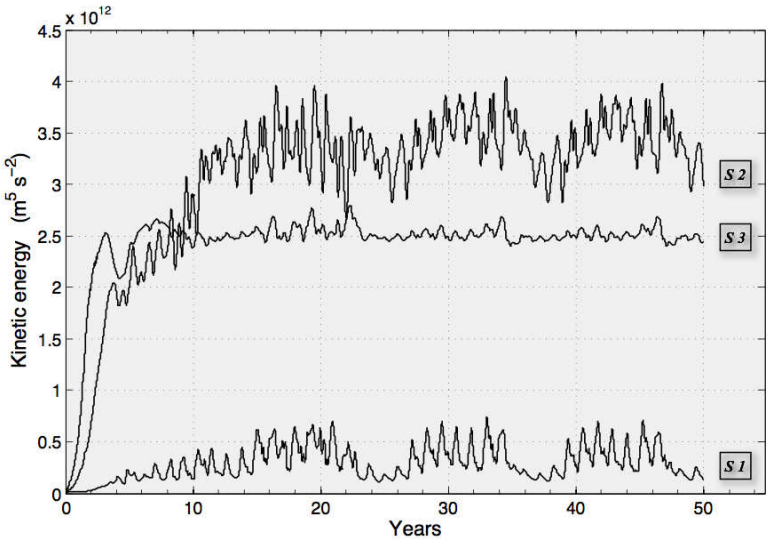

Figure 5.11: Time series of the kinetic energy integrated over the sectors $S1$, $S2$ and $S3$ (see Fig. 5.7)

the jet and includes several periodicities and high amplitude oscillations; finally, since sector $S3$ is far from the jet, it displays lower amplitude oscillations.

All the signals display chaotic oscillations due to the intrinsic non-linear dynamics, and the spectrum of the $E_K(t)$, within the region $S1 \cup S2 \cup S3$, yields peaks at 1.0; 3.9; 6.6 and 13.0 yr (Fig. 5.12).

In order to study the low-frequency variability of the jet, the last 26 years of integration are sampled yearly (taken the first day of each year). In Fig. 5.13, each line represents a snapshot of the $0 - cm$ SSH contour location of the simulated GS and GS Extension.

Some contours have been identified by green and blue solid lines, some others are dotted lines. When the Florida Current leaves its almost meridional orientation at around 31 °N, the figure shows the main changes of the seaward deflection off South Carolina. The green contours display a small northward shifting, when compared to the blue contours, and the dotted lines are found in between these two main locations.

Flowing northward the stream rejoins the coast, off North Carolina, and it yields a stable separation location at 35 °N and 75.5 °W, in very good agreement with observations. After separation from the American

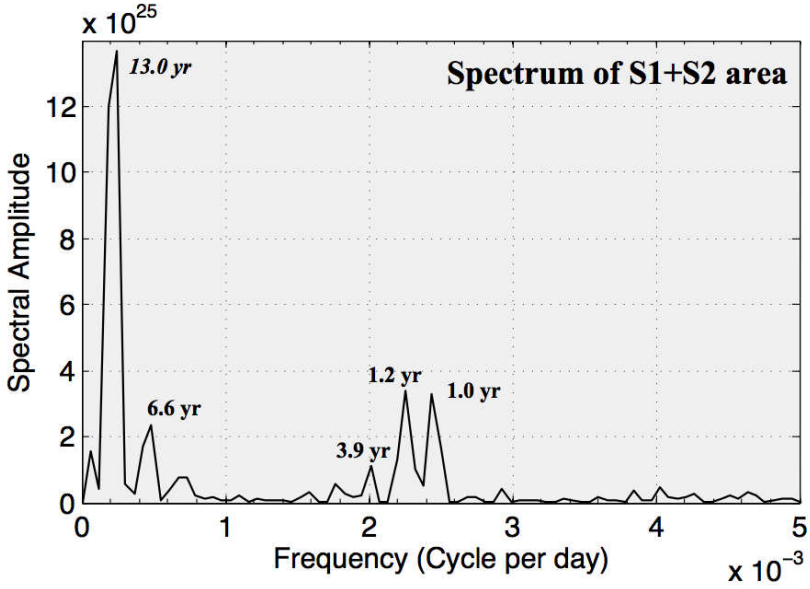

Figure 5.12: Spectral amplitudes corresponding to time series $S1 \cup S2$ in Fig. (5.11)

coast the GSE diverts into the open sea. In this region (between 75 °W and 70 °W) green and blue contours display two main meridional locations and dotted contours are found in between. The mean position of the green paths is found at 35 °N and it gradually shifts northward close to 36 °N.

The combined behavior of the green and blue states off South Carolina (in the GS deflection) and off Cape Hatteras (in the GSE) can be summarized as follows: in the green (blue) state, when the contour is located more northward (southward) in the GS deflection, the GSE is located more southward (northward).

Fig. 5.14 provides a different way to display the latitudinal shifting of the GSE jet. It shows a $t - \phi$ diagram in which the zonal geostrophic velocity at 75 °W is plotted over the 26-years interval of our analysis. In this time series the strong core of the stream is on average located at 35 °N, however transitions between the high and low latitudinal positions are showed. The stream may be stable within a period of 3-6 years and its transitions occur over shorter periods, generally 1-2 years.

Between the longitudes of 70 °W and 65 °W, very far from the coastal constraint, the GSE jet displays high amplitude meandering. All the

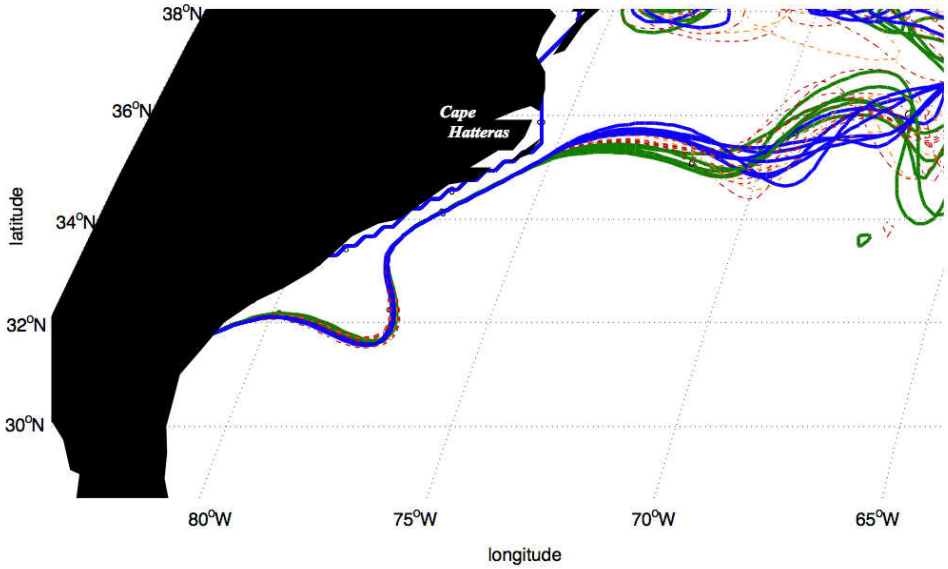

Figure 5.13: Paths of the GS and GS Extension defined by the 0-cm SSH contours (including 26 lines representing the last 26 years of the integration). (green contours): *Stretched state*, (blue contours): *Squeezed state*, (dotted lines): intermediate states. (see text for further explanation)

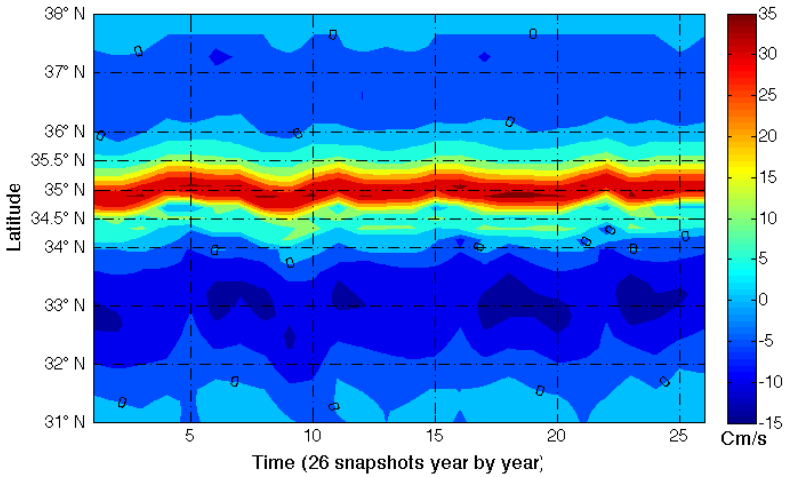

Figure 5.14: Contour plot of the simulated zonal geostrophic velocity at 75 °W as a function of latitude and for 26 samples of the integration time of the model ($m \cdot s^{-1}$).

contours are involved in a wide latitudinal shifting of about 2-3 °towards the northern and southern directions. Nevertheless, blue contours seem to follow a more straight mean path, with relatively small amplitude meandering when compared with the green contours. The flow associated with the blue contours may, hence, easily penetrate further east into the open sea.

Two main states of the GSE jet can, thus, be identified in this model simulation; a stretched state (blue contours) in which the jet has a higher latitudinal position and penetrates into the open sea, and a squeezed state (green contours), in which the jet has a lower latitudinal position and is accompanied by a strong amplitude meandering offshore.

Similar features may also be recognized in SSH observations. Fig. 5.15 shows annually averages of satellite derived Absolute Dynamic Topography (ADT) fields in 1995, 2005, 1996 and 2006 (from top to bottom). In these panel stretched and squeezed states of the GSE jet can be identified by means of two empirical indicators: the maximum meridional gradient of the SSH field $\partial h/\partial y$ along the jet and the meanders development downstream of the GSE jet.

In 1995 and 2005 the GSE jet displays a stretched state; indeed, at 72 °W, $\partial h/\partial y$ is located at about 38 °N and the jet flows eastward without any discontinuity, up to 55 °W (1995) and 62 °W (2005). By contrast, in 1996 and 2006 the $\partial h/\partial y$ maxima is located very close to 36 °N and a first meander is found at 64 °W (1998) and 69 °W (2006). Thus, the GSE jet displays a weak eastward penetration and its state may be referred to as squeezed state. Fig. 5.16 shows four SSH snapshots obtained from the model response (SSH 26, 5, 8 and 9) that have been chosen to be directly comparable with observations in Fig. 5.15. SSH 26 and SSH 5 are referred to a stretched state of the GSE jet (directly comparable with 1995, 2005) and, SSH 8 and SSH 9 are referred to a squeezed state (directly comparable with 1996, 2006).

5.6 Preliminary analysis in terms of nonlinear dynamical systems theory

The low-frequency variability of the GSE jet as simulated by the present model implementation may be also analyzed in the framework

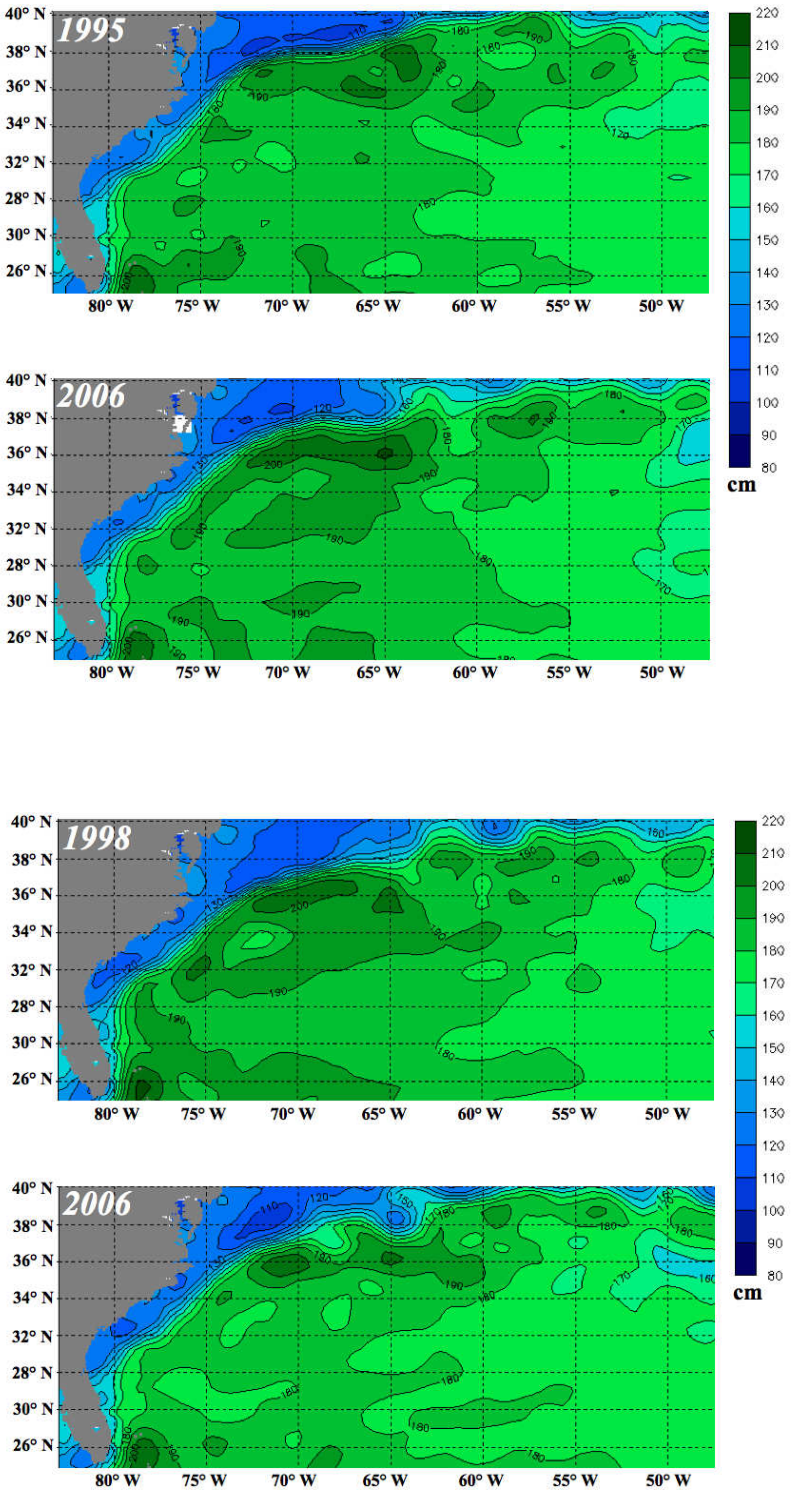

Figure 5.15: Annual mean of the absolute dynamic topography (distributed by Aviso/Cnes) in, from the top, 1995, 2005, 1998 and 2006 (cm)

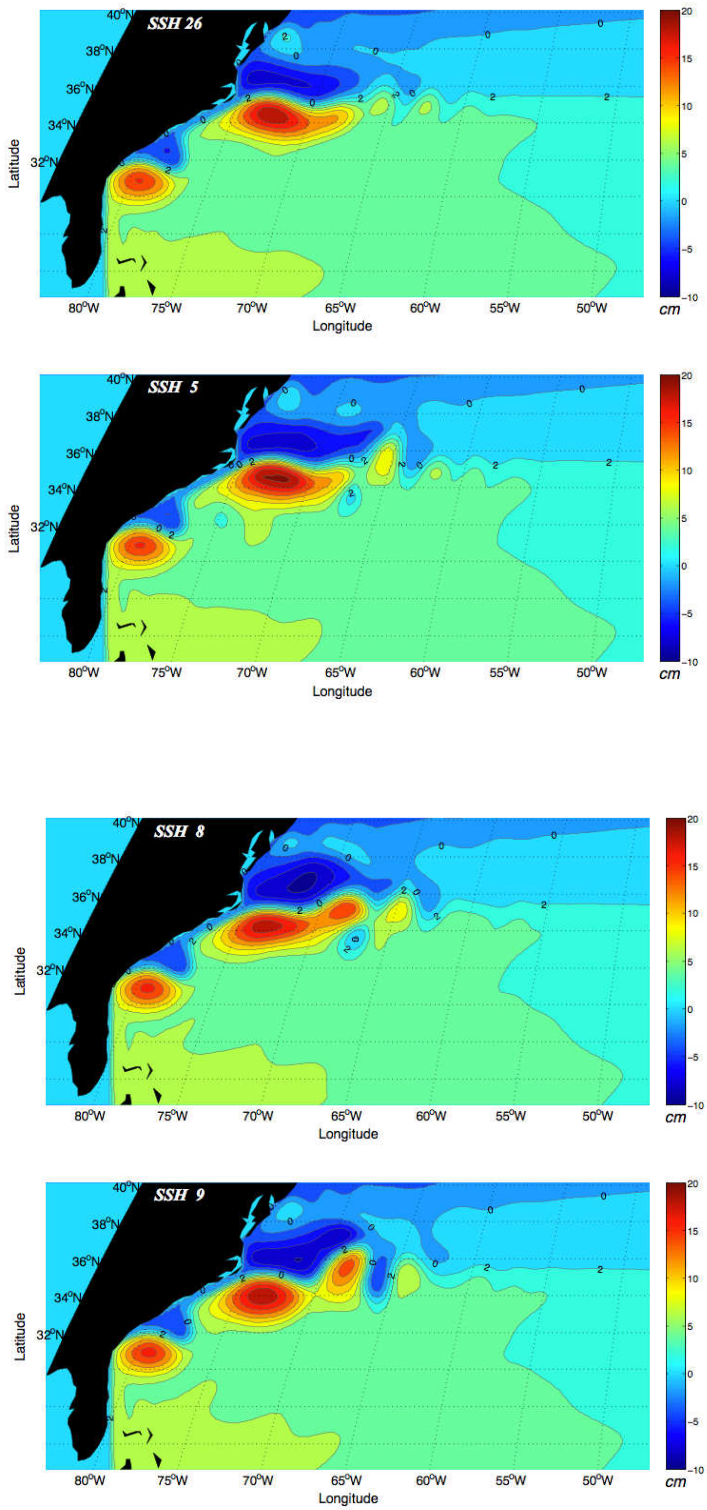

Figure 5.16: Model response for different temporal snapshots. From the top, SSH 26, SSH 5, SSH 8 and SSH 9 (amplitude: cm)

of nonlinear dynamical systems theory (see Appendix C). The aim of

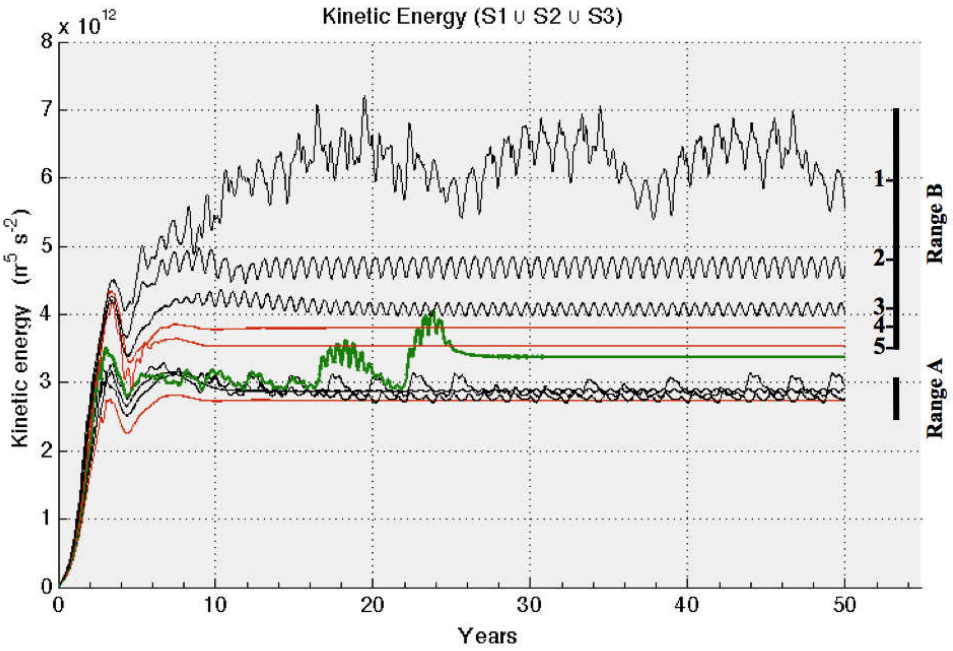

Figure 5.17: Time series of the kinetic energy integrated in sector $S1 \cup S2 \cup S3$ for different values of K_H; see text for further explanations

this approach is to provide a deeper insight into the GSE system and to understand the role played by the parameter range explored in the simulations in shaping the variability.

Fig. 5.17 shows the time series of the kinetic energy E_k of the GSE (integrated in sector $S1 \cup S2 \cup S3$). They are obtained by varying the lateral eddy viscosity coefficient K_H, used here as the control parameter. The time series with highest energy (1) represents the reference solution of the model simulations, thoroughly analyzed in the previous section. The eddy viscosity coefficient adopted for that experiment is the first value in Table 5.2. The following values listed in the table, from the top to the bottom, correspond to lower energy states of the system, displayed in Fig. 5.17. Fig. 5.18 can be read accordingly; it shows orbits projected onto the E_k (Sector 1) - E_K (Sector 2 ∪ Sector 3) plane, respectively, for different values of K_H.

Within the range $K_H = 100 - 300\, m^2\, s^{-1}$, several of low-frequency

Table 5.2: Control parameter values

Lateral eddy viscosity $m^2 \cdot s^{-1}$
$K_H = 100$
$K_H = 120$
$K_H = 140$
$K_H = 160$
$K_H = 180$
$K_H = 200$
$K_H = 220$
$K_H = 240$
$K_H = 260$
$K_H = 300$

variability scenarios can be detected: a stationary state that changes into small amplitude oscillations, higher energy periodic oscillations and a large amplitude chaotic oscillation. The red lines identify the stationary states of the system while periodic and aperiodic oscillations are represented with black lines.

From the lowest to the highest energy state of the system one can identifies a first Hopf bifurcation, that leads the stable state of the system to periodic oscillations (*Range A*). The green line shows a transition between two main regimes of variability, the second one found within the *Range B*. Here the transitions involve higher energy stable states and periodic oscillations that, with a subsequent global bifurcation, lead to a large amplitude chaotic oscillation.

In more detail, for high values of the eddy viscosity coefficient (e.g. $K_H = 300$), the internal variability disappears (see the fixed point in Fig. 5.18 corresponding to this value); below this value small oscillations, associated with the classical route to chaos quale?, are found. For $K_H = 200$ (green line) the system suddenly shifts from larger amplitude oscillations to a stable state. However, a new attractor appears when $K_H = 180$, and then a new transition to chaos begins for further decrease of K_H. For $K_H = 140$ and $K_H = 120$ two periodic oscillations are found, corresponding to limit cycles in figure 5.18; the amplitude of the oscillation approximately doubles for $K_H = 120$. Finally, for smaller values of K_H, ($K_H = 100$, for the reference experiment and $K_H = 90$, not shown) the variability degenerates into very large amplitude, highly

chaotic oscillations ($K_H = 100$), as also shown in phase space (Fig. 5.18).

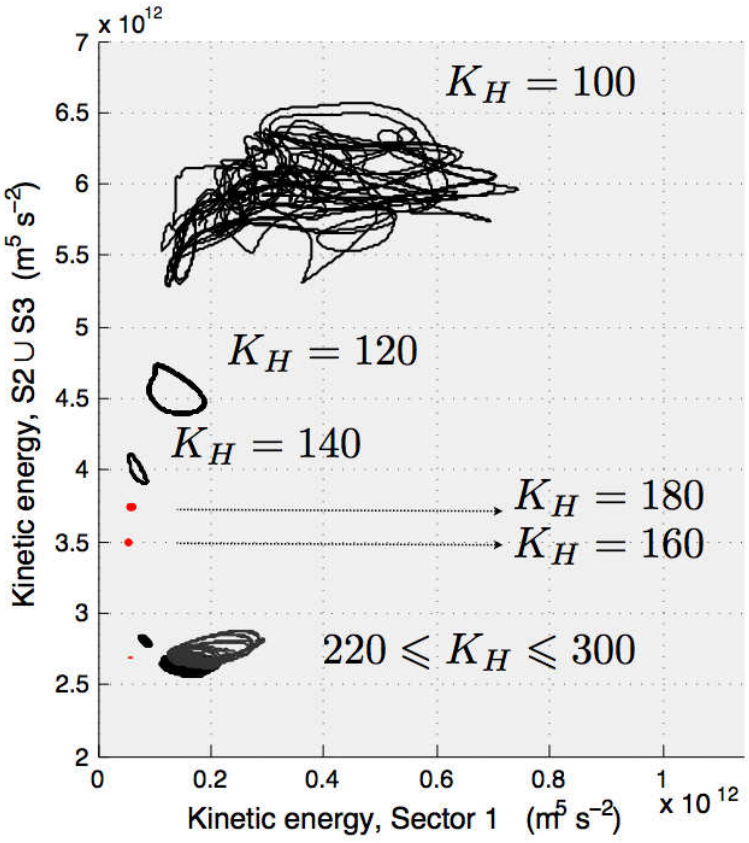

Figure 5.18: Orbits projected onto the E_k (Sector 1) - E_K (Sector 2 $\cup$ Sector 3) plane for different values of K_H

5.7 Summary and Conclusions

The results presented in this chapter show that a reduced-gravity nonlinear primitive equation ocean model with schematic (but relatively realistic) coastlines is able to simulate a number of observed features of the GS system low-frequency variability. Since those changes are obtained by forcing the model with a steady climatological wind field (derived from ECMWF data) we can be sure that such variability is generated by nonlinear mechanisms internal to the ocean system in the absence of topographic effects and baroclinic instability.

This analysis belongs to the class of process-oriented studies of the large-scale wind-driven circulation aimed at analyzing the intrinsically generated low-frequency variability (e.g., Dijkstra 2005), and shares the relatively realistic approach followed by Pierini (2006) in his study of the KE decadal variability, that has led to the simulation of the typical KE relaxation oscillation in substantial agreement with observations (as discussed in detail by Pierini and Dijkstra 2009; Pierini et al. 2009). As a consequence, this kind of model approach has once more turned out be a valuable tool to investigate the role played by intrinsic oceanic mechanism in shaping the variability. Of course, important differences distinguish the GSE from the KE, as discussed, for instance, by Kelly et al. (2010) and as shown in Fig. 5.3 and Fig. 5.4.

In section 5.3, the simulated GS mean jet was compared with observations, and substantial similarities are found in the Florida Current region and in the GS separation region off Cape Hatteras. Although, after the separation, the upstream GSE mean jet yields a meridional location in disagreement with observations, a recirculation cell and a weak meandering downstream are found in the simulations as similarly found in the observations. Moreover, in the oceanic interior the model yields a consistent description of the ocean dynamic, showing the prominent effect of the Ekman pumping in driving the oceanic response far from the western boundaries.

An analysis of the simulated low-frequency changes of the GS System (section 5.4) shows satisfactory agreement with recent satellite observations and the analysis carried out by Auer (1987). Similar is the bimodal character of the jet variability in the area just after the separation, where a meridional shifting of about 0.5 °occurs. As already mentioned above, this behavior may be explained, in the context of the present model, only in terms of an intrinsically generated variability of the inertial jet, that, in turn, allows for a further eastern penetration or early meandering (i.e. not further eastern penetration). Finally, a very preliminary analysis in the language of nonlinear dynamical systems theory (section 5.5) has allowed us to achieve a deeper understanding of the simulated GSE low-frequency variability. The results show that chaotic oscillations emerge from a global bifurcation.

Future perspectives include the use of a more realistic model that includes two-active layers, so that both the external mode, topographic effects, baroclinic instability and the interaction of the GSE with a deep western boundary current at the cross-over point can be considered (this

study is already under way). The presence of the external mode implies much more computer expensive runs, and this is a drawback when many long simulations are required to carry out an analysis in terms of dynamical system theory following the empirical continuation method. However, the use of the parallelized version of the code developed for the study of the KE (Pierini et al., 2009) will drastically reduce the computer time and make such study feasible.

Outlook

In this thesis model studies of the large-scale oceanic variability are presented. By means of a nonlinear shallow water reduced-gravity model, that includes realistic wind stress and schematic coastlines, several aspects of the observed oceanic variability are simulated. This approach provides an ideal framework in which the ocean dynamics can be investigated. Indeed, the model setup can be easily varied in order to assess the role played by the large-scale coastline orientation and the wind stress anomalies in shaping the oceanic variability.

The analysis of the wind-driven seasonal variability in the tropical Atlantic is presented in Chapter 4. Several aspects of the variability are identified and interpreted theoretically. The basin-scale dynamics, first observed from satellite altimeter derived fields, was, then, compared with the model response; annual baroclinic Rossby waves are found to radiate from the eastern boundary of the Atlantic Ocean, and the model correctly reproduces their eastern confinement North of 12°N, due to the beta-refraction effect. The local (Ekman pumping) and remote (teleconnection mechanism) contribution to the generation of such waves is also evaluated through sensitive experiments. The remote generation is foundto be an essential forcing for these mid-latitude westward propagating Rossby waves. In the same chapter, seasonal upwellings (downwellings) at the eastern boundary of the Atlantic Ocean were also analyzed by the model results. Seasonal changes of the SSH are found to be strongly affected by the teleconnection mechanism.

A qualitative agreement between the simulated sea surface height and the satellite-derived sea surface temperature is also found (not shown); thus, computing the cross-correlation between those two fields can provide evidence that coastal Kelvin wave propagation and coastal upwelling (associated with lower sea surface temperature) and downwelling (associated with higher sea surface temperature) are in phase. Within the future perspective of this research, this analysis will contribute to clarify the pre-

dominant role of remotely forced coastal Kelvin waves in controlling sea surface height changes when compared with the local atmospheric forcing in the Gulf of Guinea. Naturally, other dynamical aspects require a more realistic model approach to be fully understood. For instance, the use of a multi-layer model will allow us to simulate the complex equatorial current system together with the barotropic component.

In Chapter 5 an analysis of the low-frequency variability in the Gulf Stream region is proposed. By means of the previously adopted process-oriented model study, but with a different setup and with a time- independent forcing, a complex low-frequency variability is found originating from intrinsic oceanic mechanisms. A number of features of the observed Gulf Stream and Gulf Stream Extension (in terms of mean-path and low-frequaency variability) are identified and analyzed (in the reference experiment *Exp. A*).

In an ongoing extension of this research that makes use of a model that includes two-active layers, effects such as bottom topography, baroclinic instability and the interaction of the GSE with a deep western boundary current will be taken into account. A very preliminary analysis of the results on the intrinsically generated GSE low-frequency variability in terms of nonlinear dynamical systems theory is presented. However, more exhaustive analyses (also in progress) will require a large number of numerical simulations by varying control parameters such as the lateral eddy viscosity coefficient and the wind stress amplitude. This, in turn, will allow one to obtain a bifurcation diagram (e.g., see Pierini et al. 2009) that will shed light on the transitions between the different regimes of variability already identified in this thesis.

One last comment concerns the numerical models used in the simulations. A shallow water reduced-gravity model has been used in this thesis and a multi-layer model is going to be used, as already pointed out. A further investigation carried out with a 3D numerical ocean model (such as the Princeton Ocean Model) would provide a hierarchy of models of increasing complexity by which the observed phenomena can be analyzed, and the limits of each model approach can be evaluated.

Appendix

Appendix A

Kelvin and Rossby waves

The aim of this appendix is to derive properties of Kelvin and Rossby waves. For a more complete and comprehensive discussion on Kelvin waves and on Rossby waves the reader may refer to Pedlosky (2003) and Vallis (2006).

A.1 Kelvin waves

For the sake of simplicity one can imagine a fluid element flowing along a vertical boundary. The Earth's rotation piles up the fluid against the lateral boundary through Ekman transport, producing an offshore pressure gradient associated with the sea surface elevation. The pressure gradient force must be balance by the Coriolis force associated with the longshore flow and the geostrophic balance is reached in one direction. Due to the geostrophic balance, the longshore velocity and sea surface height decay exponentially from the boundary. The Kelvin wave amplitude is significant within an e-folding distance from the boundary of the order of the Rossby radius of deformation (defined by the ratio $\sqrt{gH}/f$ of the gravity wave speed over the absolute value of the Coriolis parameter). Such a dynamics is possible only for waves traveling with the lateral boundary to the right (left) in the Northern Hemisphere (Southern Hemisphere).

The mechanism and properties of the Kelvin waves can be illustrated by considering an idealized model with one layer of rotating fluid, the linearized shallow water model. The fluid has homogeneous density and

a free surface

$$\begin{cases} \frac{\partial u}{\partial t} - fv = -g\frac{\partial \eta}{\partial x} \\ \frac{\partial v}{\partial t} + fu = -g\frac{\partial \eta}{\partial y} \\ \frac{\partial \eta}{\partial t} + H\left(\frac{\partial u}{\partial x} + \frac{\partial v}{\partial y}\right) = 0 \end{cases} \tag{A.1}$$

The fact that $v = 0$ at $y = 0$ suggests that we look for a solution with $v = 0$ everywhere, whence these equations become

$$\begin{cases} \frac{\partial u}{\partial t} = -g\frac{\partial \eta}{\partial x} \\ fu = -g\frac{\partial \eta}{\partial y} \\ \frac{\partial \eta}{\partial t} + H\frac{\partial u}{\partial x} = 0 \end{cases} \tag{A.2}$$

The second equation of the system (A.2) shows that η and u vary along the y direction and it also shows that the direction of propagation depends on the Coriolis parameter. The first and the third equations in (A.2) lead to the standard wave equation

$$\frac{\partial^2 u}{\partial t^2} = c^2\frac{\partial^2 u}{\partial x^2} \tag{A.3}$$

where $c = \sqrt{gH}$, is the wave speed of shallow water waves.

The general solution of the (A.3) is

$$u = F_1(x + ct, y) + F_2(x - ct, y) \tag{A.4}$$

with corresponding surface displacement

$$\eta = \sqrt{H/g}[-F_1(x + ct, y) + F_2(x - ct, y)] \tag{A.5}$$

The solution represents the superposition of two waves, one (F_1) travelling in the negative x-direction, and the other in the positive x-direction. To obtain the y dependence of these functions we use the second equation of the system (A.2) which gives

$$\frac{\partial F_1}{\partial y} = \frac{f}{\sqrt{gH}}F_1, \quad \frac{\partial F_2}{\partial y} = \frac{f}{\sqrt{gH}}F_2 \tag{A.6}$$

with solutions

$$F_1 = F(x + ct)e^{\frac{y}{R}}, \quad F_2 = G(x + ct)e^{\frac{-y}{R}} \tag{A.7}$$

where $R = \sqrt{gH}/f$ is the radius of deformation. Since the solution F_1 grows exponentially away from the wall. It must be eliminated and the solution

$$u = G(x - ct)e^{\frac{-y}{R}}, \quad \eta = \sqrt{H/g}G(x - ct)e^{\frac{-y}{R}}, \quad v = 0 \tag{A.8}$$

should be adopted. Thus, Kelvin waves decay exponentially away from the boundary. If f is positive, as in the Northern Hemisphere, the boundary is to the right of an observer moving with the wave. Given a constant Coriolis parameter, we could equally have obtained a solution on a meridional wall, in which case we would find that the wave again moves such that the wall is to the right of the wave direction. Thus, in the Northern Hemisphere the wave moves anticlockwise round a basin, and conversely in the Southern Hemisphere, and in both hemispheres the direction is cyclonic.

These results can be generalized to a multilayer model (the model of the stratified ocean). Indeed, the propagating internal, or baroclinic, Kelvin wave behaves in the same manner as the surface wave, except that the motion varies with depth, and it occurs at a stable interface separating two relatively homogeneous layers. For internal Kelvin waves, the pressure gradient force normal to the lateral boundary arises from the tilt of the interface and it is balanced by the Coriolis force associated with the vertical differential flow parallel to the boundary. The internal Kelvin wave speed depends on the density difference across the interface and is given by $c = \sqrt{g'H}$, usually much smaller than that of surface Kelvin waves. A typical speed for internal Kelvin waves is of the order of O(1 $m \cdot s^{-1}$) with the "internal" radius of deformation of the order of 10 Km at mid-latitudes.

A.2 Rossby waves

While section 2.3 elucidates the mechanism of formation and propagation of the Rossby waves, this section illustrates several properties of the Rossby waves through a more rigorous mathematical approach. The motions associated with Rossby waves feels the effect of the Earth's sphericity. For large scales motions, a Cartesian coordinate system can be used to obtain a qualitatively correct view of the Rossby wave dynamics (Pedlosky, 2003). Such a frame of reference, which captures the most important effects of sphericity and which simplifies the mathematical approach, is called $\beta - plane$.

The $\beta-plane$ approximation

Since the large scale motions in the ocean are nearly horizontal, the vertical component of the Coriolis parameter is the only component of the Coriolis acceleration which is dynamically significant.

$$f = 2\Omega \sin\varphi \tag{A.9}$$

Since the large-scale motions involve wide changes in latitude, the Coriolis parameter cannot be a good approximation for the earth rotation in so a large region. If the coordinate y is direct northward and is measured from a reference latitude φ_0, then the generic latitudinal position of the motion is $\varphi = \varphi_0 + y/a$, where a is the earth's radius. Since y/a represents a small variation in latitude from the equilibrium position, the Coriolis parameter can be expanded in a Taylor series:

$$f = 2\Omega \sin\varphi_0 + 2\Omega \frac{y}{a} \cos\varphi_0 + ... \tag{A.10}$$

retaining only the first two terms,

$$f = f_0 + \beta_0 y \tag{A.11}$$

where $f_0 = 2\Omega \sin\varphi_0$ is the reference Coriolis parameter and $\beta_0 = 2(\Omega/a)$ $\cos\varphi_0$ is the β *parameter*. The beta-plane approximation is validated at mid- latitudes only if the $\beta_0 y$ term is small compared with the leading f_0 term.

Rossby waves in a single homogeneous layer

The general problem of the Rossby waves is here addressed. Important approximations will help the discussion of the issue, preserving the main theoretical aspects of the Rossby waves.

Consider a flow of a single homogeneous layer on a flat bottom ocean in the β-plane. The unforced, inviscid, linear, shallow water quasi -geostrophic equation of motion is:

$$\frac{D}{Dt}(\zeta + f - \frac{\psi}{R_e^2}) = 0 \tag{A.12}$$

where $\zeta = \nabla^2\psi$ is the vorticity and $\psi = (g/f)\eta$ is the streamfunction, that for a two dimensional flow, in a Cartesian coordinate system state $u = -\psi_y$ and $v = \psi_x$. $f = f_0 + \beta y$ and R_e is the external Rossby radius of deformation. In the case of infinite deformation radius, if the scale

of motion is much less than the deformation scale then the equation of motion is governed by

$$\frac{D}{Dt}(\zeta + \beta y) = 0 \tag{A.13}$$

Expanding the material derivative gives

$$\frac{\partial \zeta}{\partial t} + \mathbf{J}(\psi, \zeta) + \beta \frac{\partial \psi}{\partial x} = 0 \tag{A.14}$$

We now linearize such equation; that is, we suppose that the flow consists of a time-independent (mean) component plus a small perturbation Ψ. Such a mean flow must satisfy the time-independent equation of motion, and purely zonal flow will do this. If one choose a flow with no meridional dependence and let

$$\psi = \Psi + \psi'(x, y, t) \tag{A.15}$$

where $\Psi = -Uy$ and $|\psi| \ll |\Psi|$, with U the zonal component of the mean flow. Substitute (A.15) into (A.14) and neglect the nonlinear terms involving products of ψ' to give

$$\frac{\partial \zeta'}{\partial t} + \mathbf{J}(\Psi, \zeta') + \beta \frac{\partial \psi'}{\partial x} = 0 \tag{A.16}$$

Solutions to this equation may be found in the form of a plane wave

$$\psi' = Re\, \tilde{\psi} \quad e^{i(kx+ly-\omega t)} \tag{A.17}$$

where Re indicates the real part of the function.The amplitude of the oscillation is given by $\tilde{\psi}$ and the phase by $kx + ly - \omega t$, where k and l are the x- and y- wavenumbers and ω is the frequency. Solutions of the form (A.17) are valid in a domain with doubly-periodic boundary conditions; solutions in a channel can be obtained using a meridional variation of $\sin(ly)$, with no essential changes to the dynamics.

Substituting (A.17) into (A.16) yields

$$[(-\omega = +Uk)(K^2) + \beta k]\tilde{\psi} = 0 \tag{A.18}$$

where$K^2 = k^2 + l^2$. For non trivial solution this implies

$$\omega = Uk - \frac{\beta k}{K^2} \tag{A.19}$$

the disperion relation for Rossby waves. It provides the frequency ω as a function of the wavenumber.

For each positive k there is only one value of ω, and it is negative. So, the phase speed of Rossby waves c_p , in the x-direction is always towards negative x, i.e. westward

$$c_p^x = \frac{\omega}{k} = U - \frac{\beta}{K^2} \tag{A.20}$$

The group velocity c_g, in the x-direction is

$$c_g^x = \frac{\partial \omega}{\partial k} = U + \frac{\beta(k^2 - l^2)}{(K^2 + l^2)^2} \tag{A.21}$$

The group speed in the x-direction can have both signs, negative and positive. For *short waves* (i.e. for the wavelengths smaller than the deformation radius), the group speed component in the x-direction is positive, while for *long waves*, i.e. for the wavelengths larger than the deformation radius, the group speed is negative. Then, since the group speed represents the velocity at which the energy of a wave packet propagates, long waves have their energy propagating westward, and short waves have their energy propagating eastward.

For a finite deformation radius it is intuitive to derive the x components of phase speed and group velocity from the dispersion relation

$$\omega = Uk - k\frac{\beta + U/R_e^2}{K^2 + 1/R_e^2} \tag{A.22}$$

Equation (A.22) is valid for a baroclinic ocean as well, provided R is the *internal* Rossby deformation radius (R_i). Indeed, for very long waves, the deformation radius is much smaller then $1/K$ and the phase and the energy travel westward with speed

$$c_p^x \approx c_g^x \approx -\beta_0 R_i^2 \tag{A.23}$$

Moreover a maximum frequency of the Rossby wave exist, beyond which planetary waves cannot propagate given by

$$|\omega|_{max} = \frac{-\beta_0 R_i}{2} \tag{A.24}$$

Appendix B

Multivariate time series analysis

The aim of this appendix is to summarize the theoretical concepts used in this dissertation trough a mathematical approach. For a more complete and comprehensive discussion on the multivariate analysis the reader may refer to Emery and Thomson (1997).

A well known example of multivariate statistical analysis, very often used in oceanography and applied in this research, is given by the Empirical Orthogonal Functions (EOFs) analysis. The first reference to the application of EOFs analysis to geophysical fluid dynamics is a report by Lorenz in 1956 in which he developed a technique for statistical weather prediction (Emery and Thomson, 1997). The EOF procedure is one of a wider class of inverse techniques and it is equivalent to a data reduction method widely used in the social sciences known as factor analysis. The EOF analysis is aimed at identifying structures that explain the maximum amount of variance in a multivariate signal. Like Fourier transform, which uses universal global basis (i.e. trigonometric functions), for the decomposition, EOF method uses a set of specific basis functions that are determined from the specific analyzed signal. Such functions are a set of mutually orthogonal components, which are the constituents of the signal and are called *empirical* since they are derived, as stressed above, from the data set itself.

EOFs constitute the optimum means of decomposing a signal. The procedure, which depends on finding the eigenvectors and corresponding eigenfunctions of the covariance function of the variable, allows to obtain

an ordered set of orthogonal function (eigenvectors) in which the first one contains the largest variance, the second one the second-largest, and so on. The variance of the n^{th} orthogonal function is given by the n^{th} eigenvalue, therefore, the total variation exhibited by the data set is equal to the summation of all eigenvalues. By truncation at a particular level, it is possible to retain only the most essential components of the signal and to reconstitute it properly, retaining the necessary informations. Indeed, the EOFs form the empirical basis functions for a decomposition (reconstruction) of the original data set, which can be represented by the linear combination of such orthogonal functions and relative modal amplitudes. Finally, it is worth pointing out that since the EOF analysis deals with the variability, the data must have the mean removed and the filtering of any trend, if it is present, will highlight the modes of variability of the data.

B.1 EOF computation via singular values decomposition

The traditional method of computing EOF requires the use of the covariance matrix. The calculation of the covariance matrix and the solution of its eigenvalue problem could sometimes become computation impractical, especially if space dimension is large. According to Kelly (1988), the Singular Values Decomposition (SVD) permits a considerable saving in computations, providing a one-step method for computing the various components of the eigenvalue problem without the covariance matrix valuation. This is primarily true for those cases where the number of location in the spatial data matrix are far greater then number of temporal samples (Emery and Thomson, 1997). In practice, it is much simpler to derive EOF modes and respective amplitude by SVD of the original matrix of the data.

The SVD method computes three matrices: an $M \times N$ column orthogonal matrix, U, an $N \times N$ diagonal matrix, S, and the transpose V^T of an $N \times N$ orthogonal matrix V. The product of these matrices returns the MxN data matrix, D, whose number of the rows M must be greater than or equal to its number of columns N, in matrix notation:

if the data matrix is $D(M \times N) \quad with \quad M > N$, then

$$D = USV^T$$

where

$$S = diag(\sigma_1, \sigma_2, ..., \sigma_n) \quad with \quad \sigma_1 \geqslant \sigma_2 \geqslant ...\sigma_n \geqslant 0$$

U is the orthogonal matrix whose columns are the eigenvectors of the matrix DD^T and V is the orthogonal matrix whose columns are the eigenvectors of the matrix D^TD. The scalars σ_n appear in descending order of magnitude in the first N position of the diagonal matrix S. They are the singular values of the matrix D and, when they are normalized by the trace of S, denote the fractional variance in each mode of the variability. Every empirical basis function is obtained by the matrices S and V^T as

$$A = SV^T$$

With singular value decomposition we can represent the data matrix D as a linear combination of eigenvector contained in U and amplitudes, functions of the time only, contained in the matrix A. Indeed, the eigenvector are chosen to satisfy the orthogonal relationship $UU^T = I$, so that

$$D = UA$$

SVD applied to a scalar variable

Let us consider a scalar variable $f(x,t)$, defined at a discrete set of M points in physical space x and N points in time t. The function could, for example as in our case, be the temporal samples of the spatial distribution of the zonal wind stress over the tropical Atlantic Ocean and hence two dimensional in physical space

$$\tau(x_i, t_n) \quad with \quad i = 1, s; n = 1, c \tag{B.1}$$

Such a spatial distribution of temporal samples can also be written as

$$\begin{pmatrix} \tau(x_1,t_1) & \tau(x_1,t_2) & ..... & \tau(x_1,t_c) \\ \tau(x_2,t_1) & \tau(x_2,t_2) & ..... & \tau(x_2,t_c) \\ ..... & ..... & ..... & ..... \\ \tau(x_s,t_1) & \tau(x_s,t_2) & ..... & \tau(x_s,t_c) \end{pmatrix} \tag{B.2}$$

This matrix can be represented by a linear combination of the orthogonal functions: $u_k(x_i)$ as:

$$\widetilde{\tau}(x_i, t_n) = \sum_{k=1}^{s} a_k(t_n) u_k(x_i) \tag{B.3}$$

where

$$a_k(t_n) = \sum_{k=1}^{s} s(x_i, t_n) u_k(x_i) \tag{B.4}$$

are the amplitudes of the orthogonal functions. The eigenvectors $u_k(x_i)$ satisfy the orthogonality condition

$$\sum_{i=1}^{s} u_k(x_i) u_l(x_i) = \delta_{kl} \sum_{i=1}^{s} u_k^2(x_i) \tag{B.5}$$

where

$$\delta_{kl} = \begin{cases} 1, & \text{if } k = l \\ 0, & \text{if } k \neq l \end{cases} \tag{B.6}$$

and they define an orthogonal space along two directions where we can find the spatial (temporal) variance of the data set. Moreover, the fraction of the variance explained by each eigenvector is given by

$$VAR_k = \frac{\sigma_i^2}{k} \tag{B.7}$$

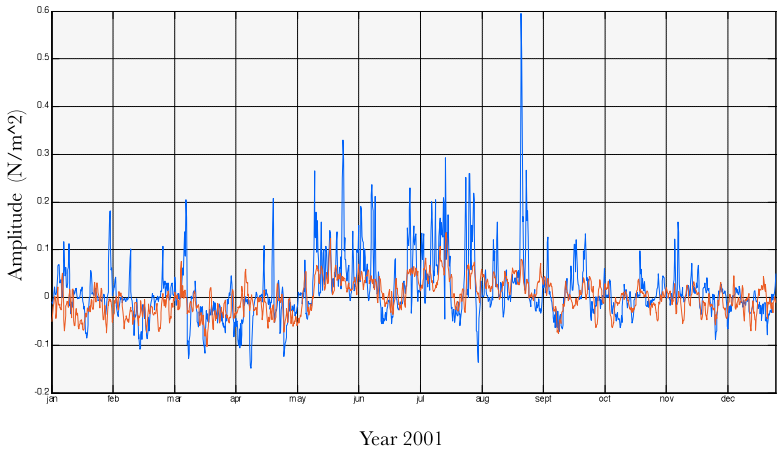

Figure B.1: The red line is an example of wind stress reconstruction, using a limited number of variability modes (20); the blue line represents the original temporal series.

By using a limited number of variability modes, those which retain most of the variance of the data, it is possible to reconstruct the original signal with a small mean square error (equation B.8) and cut off many scales of high variability (e.g. Fig. B.1). Indeed, this is the most efficient way to characterize the data using a smaller number of parameters than that in the original data set (Emery and Thomson, 1997).

$$rms = \sum_{k=1}^{s} \overline{[\tau_k(x_i, t_n) - \widetilde{\tau}_k(x_i, t_n)]^2} \tag{B.8}$$

Appendix C

Nonlinear dynamical system analysis

The aim of this appendix is to briefly summarize the theoretical concepts and techniques used in this dissertation. For a more complete and comprehensive discussion on dynamical systems theory the reader may refer to Nicolis (1999),Dijkstra (2005) and Nayfeh and Balachandran (2004).

A linear world is exactly what simple laws of proportionality can describe very easily. The experiences show that not all phenomena follow this proportionality but deviates from it. One of the most important difference between linear and nonlinear is the property of superposition (Nicolis, 1999). In a linear system the effect due to combined forces is the superposition of the effects of each one individually. On the contrary, when different forces are combined, effects may be dramatic in nonlinear systems. Nonlinear behaviors can arise in most of the natural phenomena and they can often be recognized also using simple laboratory experiments. For instance, the laboratory experiment on thermal convection proposed by Benard (1900) yielded many important features of nonlinear phenomena (e.g. Nicolis 1999).

C.1 Dynamical Systems

A mathematical model that describes the evolution in time of physical phenomena is a dynamical system Γ. It is characterized by a dimension N and it consists of an evolution law ϕ_t. An instantaneous state of such

system is defined by a value $P_t \in \Gamma$. In classical mechanics, the evolution laws, given by a set of differential equations of first order in time, allow to know the state of the model in the future and in the past.

A more generic form of evolution law, with a finite small number of variables is given by equation (C.1)

$$\frac{d\mathbf{x}}{dt} = \mathbf{f}(\mathbf{x}, \lambda, t) \tag{C.1}$$

Such equation is defined in a finite $n - dimensional$ space, $\mathbf{f}$ represent the evolution law which depends, as in the real phenomena, on the time t and on a number of parameters λ, hereafter referred as *control parameters*, which reflect the internal structure of the system (e.g. viscosity in a fluid or magnitude of the wind stress). It is possible to characterize two different kinds of dynamical systems, assuming that the evolution law does depend (*non-autonomous*) or does not depend (*autonomous*) explicitly on time. This appendix will refer to the properties of *autonomous* systems only.

Every instantaneous state ($\mathbf{P_t}$) of the system is given by a set of values $(x_1, ..., x_n)$. The evolution of the system can be described by an abstract n-dimensional space, where every dimension spans the full set of values of each variable, the *phace space* (Fig.C.1). In the course of the time t, a succession of points $(P_{t_0}, ...P_{t_n})$ in phase space will be determined and the curve $\mathbf{C}$ that joins all the points is called *phase space trajectory.*
The analysis of dynamical systems consist in the analysis of the phase space trajectory, which will be useful in determine *qualitative behaviors* of the system. In fact, not even the methods of modern science allow one to derive explicit solutions of (C.1) when n is greater than two.

Phase space: definitions and properties

Definitions:

- The evolution of the system is embedded into the n-dimensional space of the variables $(x_1, ...x_n)$ called *phace space* ($\mathbf{\Gamma}$).
- Every set of values $(x_1, ...x_n)$ bring together an instantaneous state ($\mathbf{P}$) of the system in phase space.
- For a succession of states, in the course of time t, corresponds a succession of points $(P_{t_0}, ...P_{t_n})$, in phase space, joined by a curve called *trajectory.*

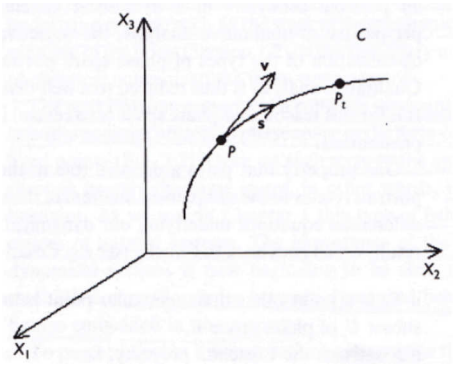

Figure C.1: Phase space trajectory of a dynamical system

- For every set of initial conditions, corresponds a *family of phase space trajectories.*

- The tangent to the phase space trajectory at given point is the *phase space velocity* $\mathbf{v} = (v_1, ...v_n)$.

- The tangents are defined everywhere in (Γ), except on points $\mathbf{x_s}$ called *singular points.* In an autonomous system, the singular points are fixed in phase space for all times, so that the terminology of *fixed point* is also used to characterize them.

Properties:

- The intersection of two trajectories, or the self-intersection of a given trajectory, is ruled out at any point other than a singular point (Nicolis, 1999). This rule is relates to the uniqueness theorem of the solutions of ordinary differential equations due to Cauchy.

> *Given* $\mathbf{X_0}$*, point and singular point in the phase space, if* $\mathbf{F}$ *satisfes the Lipschitz property*
>
> $$|\mathbf{F}(\mathbf{Y}) - \mathbf{F}(\mathbf{X})| \leq K|\mathbf{Y} - \mathbf{X}|$$
>
> *for some* $K < \infty$ *and the Euclidean norm* $|\cdot|$*, then there is an interval* $t_0 < t < t_0 + T$ *such that exists a unique solution* $\mathbf{X}(t, X_0, t_0)$ *satisfying the equation C.1, with initial condition* $\mathbf{X}(t_0) = \mathbf{X_0}$

C.1.1 Conservative and dissipative systems

Dynamical Systems are *deterministic systems*, that is, it is possible to completely identify its state $\mathbf{x} = (x_1, ..., x_n)$ at any time of the evolution. Of course, the processes of measurement are limited by a finite precision. So that, experimentally the phase space representation of a state is not a point but rather a volume $\Delta\Gamma_0$ surrounding such a point. Each point represent an initial condition, from which a phase space trajectory emanates. During the temporal evolution of the system such a volume can changes its shape and conserve the volume (*conservative system*) or it can change its shape and its volume (*dissipative system*). The uniqueness theorem ensures that *the number of phase space trajectories leaving a volume is conserved.* Gibbs in 1992 introduced the concept of *statistical ensemble*, constituted by a large number of identical systems subject to the same evolution laws and boundary condition, but differing in their initial condition. According to Gibbs, the relevant quantity to investigate in a dynamical system is not the state itself but the probability $P_{\Delta\Gamma}(t)$ of finding such a state in a phase space cell ($\Delta\Gamma$) at time t. Taking the limit of $\Delta\Gamma$ it will be investigated the *probability density* ρ

$$\rho = \frac{1}{N_{tot}} \lim_{\Delta\Gamma \to 0} \frac{\Delta N}{\Delta\Gamma} \tag{C.2}$$

where ΔN is the number of states in $\Delta\Gamma$ and N_{tot} is the total number of phase space states available. Since the number of phase space trajectories leaving a volume is conserved, two classes of dynamical system can be defined

- *Conservative systems*

  which have the property

  $$div\mathbf{f} = 0$$

  i.e. during the evolution, the phase space volume is conserved

- *Dissipative Systems*

  have the property

  $$div\mathbf{f} \neq 0$$

implying more restrictive condition

$$\overline{(div\mathbf{f})_t} < 0, \qquad t \geq t_0$$

i.e. during the evolution of a dissipative system, a contraction of phase space volume is implied .

When $t \to \infty$ the trajectories of a dissipative system, initially emanating from a certain phase space $\Delta\Gamma_0$, will tend to a subset of phase space of zero volume. This subset has a dimension strictly less then the phase space dimension and is referred to as an *attractor* of the dynamical system.The attractors are invariant manifolds, so that one can apply to them the definitions of section C.1.2.

C.1.2 Invariant manifolds

Invariant manifold are very important "objects" that could exist along a trajectory (or flow) in the phase space. They are bounded and are mapped into themselves during the evolution of the dynamical system (C.1). By this definition the trivial invariant manifold is the phase space itself.

Invariant manifolds for different phase space dimensionality

$n = 1$

The phase space is one-dimensional and the dimensionality of the invariant manifold should be strictly less then the phase space dimension. In this case, only the zero-dimensional manifold may exists. It is the *fixed point*, which has dimensionality $d = 0$. Since by virtue of (C.1) $dx_i/dt = f_i = 0$ on these points, one can concludes that, in the phase space, fixed points describe the *stationary state of the system*. The evolution of the system is limited at the point itself.

$n = 2$

In a two-dimensional phase space $n = 2$ two different manifolds can exist, whose dimension is $d = 0$ (fixed point) or $d = 1$ (invariant curve) respectively. This new manifold exhibits periodic behavior which means that a typical state of the system recurs periodically. Both manifolds can coexist showing more

complex trajectory. Some example are the *Heteroclinic trajectories*, which are curves joining fixed points and *Homoclinic trajectories*, which are curves leaving fixed point and subsequently returning to it.

$n = 3$

This case includes manifolds whose dimensionality is $d = 0, d = 1$ and $d = 3$. The latter case is described in the phase space by tori which yield a quasi-periodic behavior.

Besides this list, *fractal manifolds* do also exist. They hold chaotic behaviors and are abundant in large classes of natural systems. When the phase space has sufficiently large dimensionality ($n \geqslant 3$) such fractal manifolds, called *strange attractors*, may arise from chaotic trajectories. Since the structure of a fractal manifold is invariant with respect to different scales, its dimension is said to be a *fractal dimension.*

C.2 Stability Analysis

Stability analysis is the analysis of the *orbit structure* of a dynamical system to perturbations. Where *orbit structure* means the different orbits of the considered system and their number and stability for a give set of parameter values (Nayfeh and Balachandran, 2004). Stability analysis allows to define properties of singularity of the system which are very useful for the understanding of the future states of the system. In this context is located the concept of stability and for a finite-dimensional, and continuous on time system, the following definitions can be adopted:

- A solution $\mathbf{x}(t)$ of either an autonomous system of differential equations is stable in the sense of Lyapunov (*Lyapunov stable*) if, given a small number $\epsilon > 0$, there exists a number $\delta = \delta(\epsilon) > 0$ such that for any other solution $\mathbf{y}(t)$ with $\|\mathbf{x}-\mathbf{y}\| < \delta$ at time $t = t_0$ satisfies $\|\mathbf{x} - \mathbf{y}\| < \epsilon$ for all $t > t_0$.

that is, if $\mathbf{x}(t)$ is Lyapunov stable, then any other solution that is "close" to the initial remains so.

- $\mathbf{x}(t)$ is unstable if the Lyapunov conditions are not verified.

- A solution $\mathbf{x}(t)$ of an autonomous system of differential equations is said *asymptotically stable* if it is Lyapunov stable and, in addition $\|\mathbf{x} - \mathbf{y}\| \to 0$ as $t \to \infty$.

C.2.1 Analysis of Fixed Points

Let us consider a system of ordinary differential equations

$$\frac{d\mathbf{x}}{dt} = \mathbf{f}(\mathbf{x}, \lambda, t) \tag{C.3}$$

where $\mathbf{x}$ is the state vector in the real n-dimensional state space, $\mathbf{f}$ is a smooth vector field, λ is a control parameter and t denotes the time evolution of the system. Such equations define an autonomous dynamical system, since $\mathbf{f}$ does not depend explicitly on time. Given a parameter value $\overline{\lambda}$, the system has a solution $\overline{\mathbf{x}}$ when

$$\mathbf{f}(\overline{\mathbf{x}}, \overline{\lambda}) = 0 \tag{C.4}$$

and the solution is a fixed point or steady-state solution. That is, any trajectory with initial conditions at the fixed point will remain there forever. In the "real world", systems never stay in a single state as time vary. Most of the systems intrinsically generate their own variability and exchanges of energy with the environment should be take into account. As a result, the instantaneous state $\mathbf{x}(t)$ of the system will be always deviate from $\mathbf{x}_s$ (reference state) by an amount $\widehat{x}(t)$, referred to as the *perturbation*

$$\mathbf{x}(t) = \mathbf{x}_s + \widehat{x}(t) \tag{C.5}$$

The system can leave the reference state $\mathbf{x}_s$ or it can oscillates close to him for each time. The perturbation of the system is the starting point for the *analysis of the linear stability of fixed points*. Given x_s, the reference state and particular solution of the system (C.3), ones can substitute the solution C.5 into the system (C.3). Assuming that $\mathbf{f}(\mathbf{x}, \lambda, t)$ could be Taylor expanded in formal power series of $\mathbf{x}$ around $\mathbf{x}_s$ The linearization of the perturbed equation gives

$$\frac{d\mathbf{x}}{dt} = \mathbf{J}(\overline{\mathbf{x}}, \overline{\lambda}) \cdot \mathbf{x} \tag{C.6}$$

where $\mathbf{J}$ is the Jacobian matrix of $\mathbf{f}(\mathbf{x}, \lambda, t)$ evaluated at reference state. The original non linear problem is now replaced by an "auxiliary" linearized problem (Nicolis, 1999). In the analysis of fixed points as solutions of autonomous systems, the Jacobian operator is time-independent. It follows that equation (C.6) admits solutions that depend on time exponentially which, when substituted, lead to the eigenvalue problem

$$\mathbf{J}(\overline{\mathbf{x}}, \overline{\lambda})\widehat{\mathbf{y}} = \sigma\widehat{\mathbf{y}} \tag{C.7}$$

where $\widehat{\mathbf{y}}$ and σ are respectively, eigenvectors and eigenvalues of the Jacobian matrix. When all the eigenvalues have nonzero real parts, the corresponding fixed point is called *hyperbolic fixed point*, otherwise, it is called *nonhyperbolic fixed point*. There are three types of hyperbolic fixed point: sinks, sources and saddle points.

- *Sink*: When all the eigenvalues have negative real part. In this case, the solution decrease as $t \to \infty$, hence such a fixed point is asymptotically stable (see section C.2).

  If the Jacobian has complex eigenvalues, the sink is known as *stable focus*. If all the eigenvalues are real, the sink is also called *stable node*. All the sinks can be stable and unstable depending on the direction of time integration.

- *Sources*: When all the eigenvalues have positive real parts the fixed point is called *source*. In this contest, the perturbation grow exponentially as t increase, and the fixed point is said to be unstable.

  If the Jacobian has complex eigenvalues the source is called *unstable focus*.

- *Saddle points*: When some of the eigenvalues have positive real parts and the rest of the eigenvalues have negative real parts, the fixed point is called *Saddle points*. It is unstable in both forward and reverse times.

A nonhyperbolic fixed point is unstable if one or more of the eigenvalues have positive real parts. It is called *center*, if all the

eigenvalues are purely imaginary and non zero. When some of the eigenvalue have negative parts while the rest of the eigenvalues have zero real parts, the fixed point is said to be *neutrally stable.*

When, in the "neighborhood" of nonhyperbolic fixed points or periodic solution, qualitative changes occur, such as change in type or number of solution, the dynamical system is said to have undergone a *local bifurcation.* In bifurcation problems, the *state-control space* is very useful to describe the state of the system. It is formed by using the state variables and the control parameter. In such a space, locations at which bifurcation occur are called *bifurcation points.* Diagrams in which the variation of solutions and their stability are displayed in the state-control space are called *bifurcation diagrams.* A bifurcation called *codimension-m* requires at least m independent control parameter to occur.

Besides, *nonlocal bifurcations* (global bifurcation), associated with global changes in the state space, does exist. At a global bifurcation point, there is either a homoclinic or a heteroclinic orbit, which respectively lead to homoclinic and heteroclinic bifurcations. A well known dynamical system in which homoclinic orbits occur is the Lorenz model. Global bifurcations are of interest because they can result in the creation of chaotic orbits (Dijkstra, 2005).

Bifurcation Analysis

When a single parameter is involved in the evolution of an continuous-time and autonomous system, local bifurcations are of codimension-1 bifurcation. If one starts with a control parameter corresponding to a stable fixed point, and then slowly varies the control parameter, this fixed point can lose stability through one of the following bifurcations (Nayfeh and Balachandran, 2004): saddle-node bifurcation, pitchfork bifurcation, transcritical bifurcation and Hopf bifurcation. Several more complicated bifurcations may arise when more than one parameter in the system is changed (Dijkstra, 2005).

An example of a codimension-one bifurcation occurs in the one-dimensional autonomous dynamical system (eq. C.8).

$$\frac{dx}{dt} = f(x, \mu) = \mu x - x^3 \tag{C.8}$$

where μ is the control parameter and x the state variable. For $\mu < 0$, there is only one stable fixed point. For $\mu > 0$ there are three fixed points: $x = 0$ and $x = \pm\sqrt{\mu}$ and hence the number of fixed points changes as μ crosses zero. The bifurcation di-

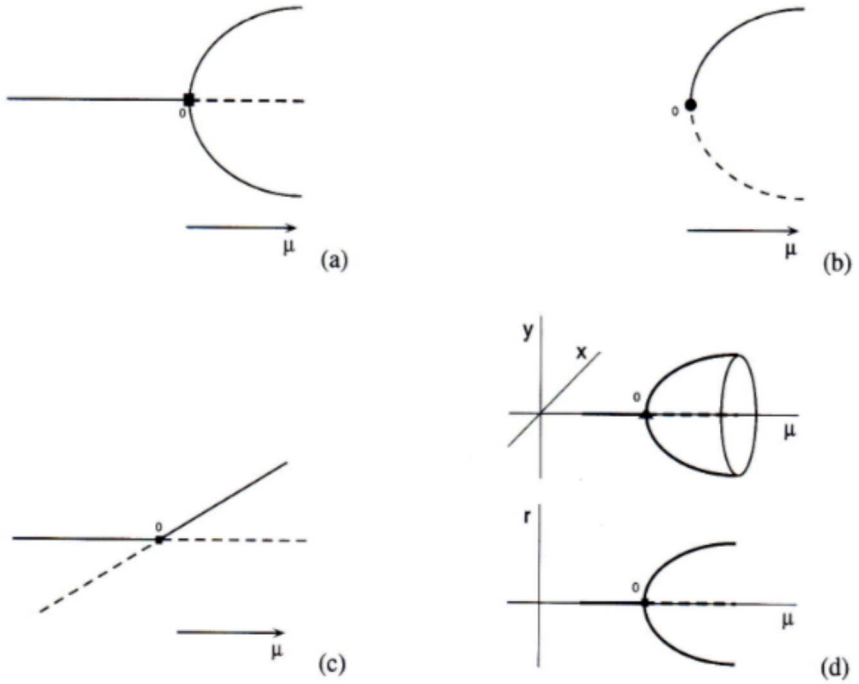

Figure C.2: Overview of codimension-one bifurcations

agram of the system (C.8) is shown in figure (C.2a) as a graph of x against μ where stable fixed fixed points are drawn and unstable states are dashed. At $\mu = 0$ the number of fixed points changes and the diagram shows the pitchfork bifurcation. Two other bifurcation diagrams are shown in figure C.2: figureC.2b represents the saddle-node bifurcation for the one-dimensional system $dx/dt = \mu - x^2$, figure C.2c represents the transcritical bifurcation for the one-dimensional system $dx/dt = \mu x - x^2$ and figureC.2d represent the saddle-node bifurcation for the two-dimensional system

$dx/dt = \mu x - \omega y - x(x^2 + y^2); dy/dt = \mu y - \omega x - y(x^2 + y^2)$(Dijkstra and Molemaker, 1999); i.e. the Hopf bifurcation, where a stable state migrates, through an unstable state, toward a stable periodic solution.

C.2.2 Analysis of Periodic Solutions

Unlike the stationary states of a system, periodic solutions are characterized by time-varying states with basic frequencies. The spectrum of a periodic signal consists of a spike at zero frequency and spikes at integer multiples of the basic frequency.

A solution of a general dynamical system C.3 is a periodic solution, of period T, if it satisfies $\mathbf{x}(t + T) = \mathbf{x}(t)$ and $\mathbf{x}(t + \tau) \neq \mathbf{x}(t)$ for $0 < \tau < T$. To determine the stability of a periodic solution Floquet theory provides a set of "multiplers" (values), which measure the degree of divergence or convergence of the orbit. Indeed, if a trajectory starts at the periodic orbit it will stay on the orbit, while if a trajectory starts near the orbit it may diverge or converge from the orbit and this defines its stability.

Bifurcation Analysis
When one control parameter is varied, the state-control space portrait may show qualitative differences and the accompanying qualitative change in the periodic solutions of a dynamical system is known as "bifurcation" (codimension-one bifurcation). If one starts with a control parameter corresponding to a stable periodic solution, and then slowly varies the control parameter, the periodic solution loses stability through a rich set of bifurcations (Nayfeh and Balachandran, 2004). Period doubling bifurcation is one of such bifurcations. This bifurcation, introduces a new frequency, which has twice the period of the original orbit, into the behavior of the dynamical system (Dijkstra, 2005).

C.3 Chaos

Since chaotic solutions cannot be represented through a standard mathematical function, several definitions are universally excepted

for them. Such definitions depend on special identifiable characteristics of the solution itself. A broad definition could state that, in a deterministic system, a chaotic solution is an aperiodic solution which exhibits sensitive dependence on initial conditions. Lorenz, nicely introduced the *butterfly effect* to highlight the sensitivity of some system to initial condition; that is, tiny differences in the input can be quickly amplified and create huge differences in the output.

In the state phase, the attractor associated with a chaotic motion is not a manifold, so that, it is not a point or a closed curve but it is a complicated geometrical object that possesses fractal dimension. A spectrum of a chaotic signal has a continuous broadband character with a number of superimposed spikes that indicate the predominant frequencies. As Nayfeh and Balachandran (2004) argue, a chaotic system may dwell for a brief time on a motion that is very nearly periodic and than may change to another periodic motion. The latter usually has a period that is k times that of the preceding motion, producing a long-time impression of randomness with glimpses of order.

Routes to Chaos

In a nonlinear dynamical system, transitions to chaotic solutions may appear when a control parameter is varied. Several routes bring the system to chaos and *Period-Doubling mechanism* and *Intermittency mechanism* will be shortly described in this section.

In the period-doubling scenario, a solution turn from its periodic behavior to a chaotic behavior via a sequence of period-doubling local bifurcations. The period increases until the control parameter reaches a critical value beyond which the chaotic behavior appears (Feigenbaum, 1978). The intermittency is the second listed route to chaos which is observed frequently in physical experiments. In this case, if one varies the control parameter value, a regular almost stable oscillation may be intermittently interrupted by chaotic outbreaks at irregular intervals. In the intermittency mechanism, the old periodic attractors can disappear and they can be replaced by larger chaotic attractors.

References

Adamec, D. and J. O'Brian, 1978: The seasonal upwelling in the Gulf of Guinea due to remote forcing. *J. Phys. Oceanogr.*, **8**, 1050–1060.

Adcroft, A. and D. Marshall, 1998: How slippery are piecewise-constant coastlines in numerical ocean models? *Tellus*, **50A**, 95–108.

Arnault, S., A. Morliere, and J. Merle, 1992: Low-frequency variability of the tropical Atlantic surface topography: Altimetry and model comparison. *J. Phys. Oceanogr.*, **97 (C9)**, 14,259–14,288.

Auer, S. J., 1987: Five-year climatological survey of the Gulf Stream system and its associated rings. *J. Geophys. Res.*, **92 (C11)**, 11,709–11,726.

Bane, J. M. and W. K. Dewar, 1988: Gulf Stream bimodality and variability downstream of the Charleston Bump. *J. Geophys. Res.*, **93**, 6695–6710.

Batchelor, G. K., 1967: *An introduction to fluid dynamics*. Cambridge mathematical library, Cambridge University Press, 541 pp.

Busalacchi, A. J. and J. Picaut, 1983: Seasonal variability from a model of the tropical Atlantic Ocean. *J. Phys. Oceanogr.*, **13**, 1564–1587.

Chassignet, E. and D. Marshall, 2008: Gulf Stream separation in numerical ocean models. *In Eddy-Resolving Ocean Modeling*, **M. Hecht and H. Hasumi, Eds. (AGU Monograph Series)**, 39–62.

Chassignet, E. P. and Z. D. Garaffo, 2001: Viscosity parameterization and the Gulf Stream separation. *In "From Stirring to Mixing in a Stratified Ocean". Proceedings of the 12th 'Aha Huliko'a Hawaiian Winter Workshop. U. of Hawaii.*, **P. Muller and D. Henderson, Eds.**, 37–41.

Chelton, D. B. and M. G. Schlax, 1996: Global observation of oceanic R ossby waves. *Science*, **272**, 234–238.

Colling, A. and O. CourseTeam, 2002: *Ocean Circulation*. BH and The Open University, 286 pp.

Dengg, J., A. Beckmann, and R. Gerdes, 1996: The Gulf Stream separation problem. *In the warmwatersphere of the North Atlantic Ocean, Krauss, W. A., editor. Borntraeger*, 253–290.

Dijkstra, H. and M. Ghill, 2005: Low-frequency variability of the large-scale ocean circulation: A dinamical system approach. *Rev. Geophys.*, **43**, 1–38.

Dijkstra, H. and C. Katsman, 1997: Temporal variability of the quasi-geostrophic wind-driven ocean circulation, Geophysical and Astrophysical Fluid Dynamics. *Geophysical and Astrophysical Fluid Dynamics*, **85**, 195–232.

Dijkstra, H. A., 2005: *Nonlinear Physical Oceanography*. Springer, 532 pp.

Dijkstra, H. A. and M. J. Molemaker, 1999: Imperfections of the North-Atlantic wind-driven ocean circulation: continental geometry and wind stress shape. *J. Mar. Res.*, **57**, 1–28.

Emery, W. J. and R. E. Thomson, 1997: *Data Analysis Methods in Physical Oceanography*. Pergamon, 634 pp.

Feigenbaum, M. J., 1978: Quantitative universality for a class of nonlinear trasformations. *Journal of Statistic Physic*, **19**, 25–52.

Flierl, G. R., 1978: Models of vertical structure and the calibration of two-layer models. *Dyn. Atmos. Oceans*, **2**, 341–381.

Fu, L. L. and R. A. Chelton, 2001: *Large-scale ocean circulation. Satellite altimetry and Earth Sciences. L.L. Fu and A. Cazenave*. Academic Press, 133-169 pp.

Gill, A. E., 1982: *Atmosphere-Ocean Dynamics*. Academic Press, 662 pp.

Han, W., P. J. Webster, J.-L. Lin, W. Liu, R. Fu, D. Yuan, and A. Hu, 2008: Dynamics of intraseasonal sea level and thermocline variability in the equatorial Atlantic during 2002-03. *J. Phys. Oceanogr.*, **38**, 945–967.

Hermann, P. and W. Krauss, 1989: Generation and propagation of annual Rossby waves in the North Atlantic. *J. Phys. Oceanogr.*, **19**, 727–744.

Hogg, A. M., P. D. Killworth, and J. R. Blundell, 2005: Mechanisms of decadal variability of the wind-driven ocean circulation. *J. Phys. Oceanogr.*, **35**, 512–531.

Houghton, R. W., 1976: Circulations and hydrographic structure of the Ghana continental shelf during the 1974 upwelling. *J. Phys. Oceanogr.*, **6**, 909–924.

Johns, W. E., T. J. Shay, J. M. Bane, and D. Watts, 1995: Gulf Stream structure, transport and recirculation near 68 °w. *J. Geophys. Res.*, **100**, 817–838.

Josey, S. A., E. C. Kent, and P. K. Taylor, 2002: Wind stress forcing of the ocean in the SOC climatology: Comparison with the NCEP-NCAR, ECMWF, UWM/COADS, Hellerman and Rosenstain dataset. *J. Phys. Oceanogr.*, **32**, 1993–2018.

Kantha, L. H. and C. A. Clayson, 2000: *Numerical Models of Oceans and Oceanic Processes*. Academic Press, 943 pp.

Katz, E. J. and collaborators, 1977: Zonal pressure gradient along the equatorial Atlantic. *J. Mar. Res.*, **35**, 293–307.

Kelly, K. A., 1988: Comment on "empirical orthogonal function analysis of advanced very high resolutin radiometer surface temperature patterns in Santa Barbara Channel" by G.S.E. Largerloef and r. l. berstein. *J. Geophys. Res.*, **93**, 15,753–15,754.

Kelly, K. A., R. J. Small, R. Samelson, B. Qiu, and T.M.Joyce, 2010: Western Boundary Currents and Frontal Air-Sea Interac-

tion: Gulf Stream and Kuroshio Extension. *Revised for J. Climate January.*

Kowalik, Z. and T. S. Murty, 1993: *Numerical Modeling of Ocean Dynamics.* World Scientific, 481 pp.

Lee, T. and P. Cornillon, 1995: Temporal variation of meandering intensity and domain-wide lateral oscillations of the Gulf Stream. *J. Geophys. Res.*, **100 (C7)**, 13,603–13,613.

Matsuno, T., 1966: Quasi-geostrophic motion in the equatorial area. *Journal of the Metorological Society of Japan*, **44**, 25–42.

McCalpin, J. D. and D. Haidvogel, 1996: Phenomenology of the low-frequency variability in a reduced-gravity, quasigeostropic double-gyre model. *J. Phys. Oceanogr.*, **26**, 739–752.

McCreary, J., 1976: Eastern Tropical Ocean Response to Changing Wind Systems: with Application to El Niño. *J. Phys. Oceanogr.*, **6**, 632–645.

Moore, D. W., P. Hisard, J. P. McCreary, J. Merle, J. J. O'Brien, J. Picaut, J. Verstraete, and C. Wunsch, 1978: Equatorial adjustment in the eastern Atlantic. *Geophys. Res. Lett.*, **5**, 637–640.

Moore, D. W. and S. G. Philander, 1977: Modeling of the tropical ocean circulation. *The Sea, E. Goldberg et al.*, Wiley, 319–361.

Mueller, T., Y. Ikeda, N. Zangenberg, and L. V. Nonato, 2000: Direct measurement of Western Boundary Currents off Brazil between 20s and 28s. *J. Geophys. Res.*, **28**, 28, 509–28, 526.

Munk, W., 1950: On the wind-driven ocean circulation. *j. Meteorology*, **7**, 79–93.

Nayfeh, A. H. and B. Balachandran, 2004: *Applied Nonlinear Dynamics: analytical, computational, and Experimental Methods.* Wiley-VCH, 685 pp.

Nicolis, G., 1999: *Introduction to Nonlinear Science.* Cmbridge University Press, 254 pp.

Pedlosky, J., 1987: *Geophysical Fluid Dynamics.* Springer-Verlag, 688 pp.

Pedlosky, J., 2003: *Waves in the Ocean and Atmosphere*. Springer, 260 pp.

Philander, S. and R. C. Pacanowsky, 1986: A model of the seasonal cycle in the tropical Atlantic Ocean. *J. Geophys. Res.*, **91 (C12)**, 14,192–14,206.

Philander, S. G., 1990: *El Niño, La Niña, and the Southern Oscillation*. Academic Press, 289 pp.

Pierini, S., 1996: Topographic Rossby modes in the Strait of Sicily. *J. Geophys. Res.*, **101**, 6429–644.

Pierini, S., 2002: Sea modeling by microwave altimetry. *In: "Remote Sensing of Atmosphere and Ocean from Space: Models, Instruments and Techniques", Advances in Global Change Research, F. Marzano and G. Visconti (Editors). Kluwer Academic Publishers*, **(ISBN: 1-4020-0943-7)**, 165–182.

Pierini, S., 2003: A model of the wind-driven seasonal variability in the tropical North Pacific, with validation through altimeter data. *J. Phys. Oceanogr.*, **35**, 218–231.

Pierini, S., 2005: A model study of the spectral structure of boundary-driven Rossby waves, and related altimetric implications. *J. Phys. Oceanogr.*, **35**, 218–231.

Pierini, S., 2006: A Kuroshio Extension system model study: decadal chaotic self-sustained oscillations. *J. Phys. Oceanogr.*, **36**, 1605–1625.

Pierini, S., 2008: On the crucial role of basin geometry in double-gyre models of the Kuroshio Extension. *J. Phys. Oceanogr.*, **38**, 1327–1333.

Pierini, S. and H. A. Dijkstra, 2009: Low-frequency variability of the Kuroshio Extension. *Nonlinear Process. in Geoph.*, **16**, 665–675.

Pierini, S., H. A. Dijkstra, and A. Riccio, 2009: A nonlinear theory of the Kuroshio Extension bimodality. *J. Phys. Oceanogr.*, **39**, 2212–2229.

Pierini, S., P. Falco, G. Zambardino, T. A. McClimans, and I. Ellingsen, 2010: A laboratory study of nonlinear Western Boundary Currents, with application to the Gulf Stream separation due to inertial overshooting. *Submitted.*

Polito, P. S. and O. T. Sato, 2007: Global interannual trends and amplitude modulations of the sea surface height anomaly from the TOPEX/Jason-1 Altimeters. *J. Climate*, **21**, 2824–2834.

Polo, I., A. Lazar, B. R. Rodriguez-Fonseca, and S. Arnault, 2008: Oceanic Kelvin waves and tropical Atlantic interseasonal variability: 1. Kelvin wave characterization. *J. Geophys. Res.*, **113**, 1–18.

Pond, S. and G. L. Pickard, 1991: *Introductory Dynamical Oceanography.* Pergamon Press, 329 pp.

Qiu, B., 2002: The Kuroshio Extension system: Its large-scale variability and role in the midlatitude ocean-atmosphere interaction. *J. Oceanogr*, **58**, 57–75.

Qiu, B. and S. Chen, 2005: Variability of the Kuroshio Extension Jet, recirculation gyre, and mesoscale eddies on decadal time scales. *J. Phys. Oceanogr.*, **35**, 2090–2103.

Quattrocchi, G. and S. Pierini, ...: Locally and remotely forced upwelling events along the western coasts of africa at low latitudes. *In preparation.*

Quattrocchi, G., S. Pierini, and H. A. Dijkstra, ...: On the intrinsic low-frequency variability of the gulf stream extension. *In preparation.*

Risien, C. M. and D. B. Chelton, 2008: A global climatology of surface wind and wind stress fields from quikSCAT scatterometer data. *J. Phys. Oceanogr.*, **38**, 2379–2413.

Robinson, I. S., 1994: *Satellite Oceanography.* Wiley, 455 pp.

Roisin, B. C. and J.-M. Beckers, 2010: *Introduction to Geophysical Fluid Dynamics.* Academic Press, 762 pp.

Schmeits, M. J. and H. A. Dijkstra, 2001: Bimodal behavior of the Kuroshio and the Gulf Stream. *J. Phys. Oceanogr.*, **31**, 3435–3456.

Simonnet, E., 2003: Low-frequency variability in shallow-water models of the wind-driven ocean circulation. part ii: Time-dependent solution. *J. Phys. Oceanogr.*, **33**, 729–752.

Simonnet, E., M. Ghil, K. Ide, R. Temam, and S. Wang, 2003: Low-frequency variability in shallow-water models of the wind-driven ocean low-frequency variability in shallow-water models of the wind-driven ocean circulation. part i: Steady-state solution. *J. Phys. Oceanogr.*, **33**, 712–728.

S.Jiang, F. Jin, and M. Ghil, 1995: Multiple equilibria, and aperiodic solutions in a wind-driven, double-gyre, shallow-water model. *J. Phys. Oceanogr.*, **25**, 764–786.

Smith, S. D., 1980: Wind stress and heat flux over the oceanin gale force winds. *J. Phys. Oceanogr.*, **10**, 709–726.

Spall, M. A., 1996a: Dynamics of the Gulf Stream/Deep Western Boundary Current Crossover. Part ii: Low-frequency internal oscillation. *J. Phys. Oceanogr.*, **26**, 2169–2182.

Spall, M. A., 1996b: Dynamics of the Gulf Stream/Deep Western Boundary Current Crssover. Part i: Entrainment and recirculation crossover. *J. Phys. Oceanogr.*, **26**, 2152–2168.

Stommel, H., 1948: The westward intensification of wind-driven ocean currents. *Trans. Amer. Geophysical Union*, **29**, 202–206.

Stramma, L., Y. Ikeda, and R. G. Peterson, 1990: Geostrophic transport in the Brazil Current region north of 20 ° s. *Deep-Sea Res.*, **37**, 1875–1886.

Sverdrup, H. U., 1947: Wind-driven currents in a baroclinic ocean with application to the equatorial current in the eastern Pacific. *Proc. Natl. Acad. Sci. Wash*, **33**, 318–326.

Tomczak, M. and J. S. Godfrey, 2001: *Rgional Oceanography: an introduction*. Pergamon (web pdf version 1.0), 391 pp.

Townsend, T., H. Hurlburt, and P. J. Hogan, 2000: Modeled Sverdrup flow in the North Atlantic from 11 different wind stress climatologies. *Dyn. Atmos. Oceans*, **32**, 373–417.

Vallis, G. K., 2006: *Atmospheric and Oceanic Fluid Dynamics*. Cambridge, 745 pp.

White, W. B., 1977: Annual forcing of baroclinic long waves in the tropical North Pacific Ocean. *J. Phys. Oceanogr.*, **7**, 50–61.

Wilson, W. and W. Johns, 1997: Velocity structure and transport in the windward islands passages. *Deep-Sea Res.*, **44**, 487–520.

WOCE, 2001: Ocean circulation and climate: Observing and modeling the global ocean. *[Siedler, G. and Church, J and Gould, J. (Eds)]. Academic Press, San DIego, USA*.

Wyrtki, K., L. Magaard, and J. Hagar, 1976: Eddy energy in the oceans. *J. Geophys. Res.*, **81**, 2641–2646.

Xie, S. P., W. T. Liu, Q. Liu, and M. Nonaka, 2001: Far-reaching effect of the Hawaiian Islands on the Pacific Ocean atmosphere. *Science*, **292**, 2057–2060.